© 2014

Hua Wang

ALL RIGHTS RESERVED

EFFECTS OF MICROBIAL ATTACHMENT AND BIOFILM FORMATION ON MICROBIOLOGICALLY INFLUENCED CORROSION

A Dissertation

Presented to

The Graduate Faculty of The University of Akron

In Partial Fulfillment

of the Requirements for the Degree

Doctor of Philosophy

Hua Wang

May, 2014

EFFECTS OF MICROBIAL ATTACHMENT AND BIOFILM FORMATION ON MICROBIOLOGICALLY INFLUENCED CORROSION

Hua Wang

Dissertation

Approved:	Accepted:
Advisor Dr. Bi-min Zhang Newby	Department Chair Dr. H. Michael Cheung
Committee Member Dr. Lu-Kwang Ju	Dean of the college Dr. George K. Haritos
Committee Member Dr. Gang Cheng	Dean of the Graduate School Dr. George R. Newkome
Committee Member Dr. Jiang Zhe	Date
Committee Member Dr. Amy Milsted	

ABSTRACT

This dissertation describes the effects of microbial attachment and biofilm formation on microbiologically influenced corrosion (MIC). The participation of microbes in the corrosion process includes initial attachment, biofilm formation, localized environment changing, and eventually, corrosion.

Initial microbial attachment is considered as the first step of MIC. In the first part of this study, the initial attachment of three bacteria, *Pseudomonas aeruginosa*, *Escherichia coli,* and *Pseudomonas putida*, on two substrates, glass and octadecyltrichlorosilane (OTS) modified glass, was examined in flow chambers. The attachment trend on glass could be explained by the secondary minima and energy barriers as predicted by the extended Derjaguin-Landau-Verwey-Overbeek (XDLVO) theory. This part of study generated some insights into the effects of cell and substrate surface properties on initial bacterial attachment.

In addition to the surface and medium properties, other factors such as the shear associated flow conditions could be one of the most important factors affecting initial bacterial attachment as well. In the second part of this study, four bacteria, *Staphylococcus epidermidis*, *P. aeruginosa*, *P. putida*, and *E. coli*, were examined for their attachment to glass and OTS modified glass under different shears. The results from this part of the study suggested that, without complications from surface

features/extracellular polymeric substances (EPS), the analysis based on the XDLVO theory could provide a basis for understanding shear effect on initial bacterial attachment. The critical shear stress, a measure of bacterial attachment strength, was found to be correlated with the maximum attractive force towards the secondary energy minimum.

As microbes attach and develop into biofilm on metal surfaces, the localized environment of metal surfaces could be changed by the influence of microbial metabolism. The third part of this study is intended to evaluate how early stage of biofilm formation affects carbon steel and aluminum alloy corrosion. In this part, aluminum alloy (Al 3003 H14) coupons and carbon steel (CS C1010) coupons were used, along with two common bacterial strains, *P. aeruginosa* and *E. coli*. Results showed that bacterial attachment strength and subsequent biofilm development could strongly influence metal corrosion behaviors.

In the fourth part of this study, corrosion behaviors of carbon steel (CS C1010) and stainless steel (SS 304) in the presence of iron-oxidizing bacteria: *Acidithiobacillus ferrooxidans* was examined. Results showed that, due to the extremely high oxidizing rate of Fe(II) to Fe(III), *A. ferrooxidans* cells can accelerate CS corrosion, while SS 304 showed a good resistance to corrosion. The accelerated CS corrosion was likely related to the metabolism of *A. ferroxidans*, but not to the attachment strength and biofilm development of *A. ferroxidans*.

In the last part, corrosion behaviors of aluminum alloy (Al 2024) in the presence of *Trichoderma reesei* and *Aspergillus niger* were evaluated. Results showed that *T. reesei* or *A. niger* could not firmly attach to Al coupon surfaces in an aqueous environment, and they could not corrode Al 2024 under our experimental conditions.

ACKNOWLEDGMENTS

The writing and completion of this Dissertation would not been possible without the guidance, support and assistance of many people.

First, I would like to thank my advisor, Dr. Bi-min Zhang Newby whom motivated, inspired, and guided me during my PhD study. She certainly made this work possible.

I would also like to thank all of my committee members: Dr. Lu-Kwang Ju, Dr. Gang Cheng, Dr. Jiang Zhe, and Dr. Amy Milsted, for their support and invaluable input throughout this study.

Many thanks to Dr. John M. Senko, Dr. Homero Castaneda-Lopez, Dr. Carla Giai, and Dr. Lingyan Li for their valuable suggestions and assistance.

Special thanks to my colleagues: Dr. Yangjun Cai, Akhila Raya, Hokyung Song, Suchata Kirdponpattara, Dipika Parajuli, Siriporn Taokaew, Nicholas Callow, Dr. Maysam Sodagari, Yajie Chen, Dr. Srujana Koganti, Xin He and Dr. Zhongye Lin for their constant assistance.

Finally, I would like to express my greatest gratitude to my parents and my wife for their endless love and unconditional support during these years.

TABLE OF CONTENTS

Page

LIST OF TABLES xi

LIST OF FIGURES xiii

CHAPTER

INTRODUCTION 1

1.1 Importance of microbiologically influenced corrosion study 1

1.2 Objectives of research 3

1.3 Overview of the dissertation 4

BACKGROUND 6

2.1 Microbiologically influenced corrosion 6

2.2 The DLVO and XDLVO theories 8

2.3 Current studies of shear effect on bacterial attachment 11

2.4 Microbial species 13

2.4.1 *Pseudomonas aeruginosa* PAO1 13

2.4.2 *Escherichia coli* 13

2.4.3 *Pseudomonas putida* 14

2.4.4 *Staphylcoccus epidermidis* 15

2.4.5 *Acidithiobacillus ferrooxidans* 15

2.4.6 *Trichoderma reesei* 16

2.4.7 *Aspergillus niger* 16

2.5 Flow chamber system 17

2.6 Background on Characterization Techniques 19

2.6.1 Laser scanning confocal microscopy 19

2.6.2 InfiniteFocus microscopy 22

2.6.3 Atomic force microscopy 22

2.6.4 Standard test method for corrosivity of water in the absence of heat transfer 25

EXPERIMENTAL APPROACH 26

3.1 Materials and Equipment 26

3.2 Effects of cells and substrate surface properties on initial bacterial attachment in slow flowing systems 28

3.2.1 Chamber surface preparation and characterization 28

3.2.2 Bacterial suspension preparation 29

3.2.3 Bacterial hydrophobicity evaluation 30

3.2.4 Cell surface zeta potential measurement 31

3.2.5 Bacterial attachment study using the flow chamber system 32

3.3 Effects of shear on initial bacterial attachment in slow flowing systems 33

3.3.1 Chamber preparation 33

3.3.2 Bacterial and particle suspensions preparation 33

3.3.3 Surface properties evaluation 34

3.3.4 Bacterial cell and particle attachment 34

3.4 Corrosion of carbon steel and aluminum alloy in the presence of *Pseudomonas aeruginosa* and *Escherichia coli* biofilm 35

3.4.1 Preparation of coupons 35

3.4.2 Design of flow chambers 36

3.4.3 Preparation of bacterial suspension 36

3.4.4 Monitoring bacterial attachment and biofilm formation and subsequent MIC behaviors 37

3.4.5 Post-run treatments and imaging 39

3.4.6 Corrosion rate determination 39

3.5 Corrosion behaviors of carbon steel C1010 and stainless steel 304 in the presence of iron oxidizing bacteria *Acidithiobacillus ferrooxidans* 40

3.5.1 Preparation of coupons 40

3.5.2 Preparation of bacterial suspension 41

3.5.3 Bacterial attachment study using the flow chamber system 41

3.5.4 Corrosion test and monitoring biofilm formation 42

3.5.5 Post-run treatments and imaging 42

3.5.6 Corrosion rate determination 43

3.6 Corrosion evaluations of aluminum alloy (Al 2024) in the presence of *Trichoderma reesei* and *Aspergillus niger* 43

3.6.1 Preparation of coupons 43

3.6.2 Preparation of fungal suspension 44

3.6.3 Fungal attachment study using static vessel system 44

3.6.4 Corrosion rate determination 46

RESULTS AND DISCUSSION 47

4.1 Effects of cell and substrate surface properties on initial bacterial attachment in slow flowing systems 48

4.1.1 Introduction 48

4.1.2 Initial attachment on glass chambers 51

4.1.3 Initial attachment on OTS modified glass chambers 52

4.1.4 Hydrophobic partitioning of bacterial cells to hexadecane 54

4.1.5 Surface properties evaluations 56

4.1.6 Interpretation of the attachment data by the extended DLVO theory 58

4.1.7 Summary 65

4.2 Effects of shear on initial bacterial attachment in slow flowing systems 67

4.2.1 Introduction 67

4.2.2 Initial attachments 68

4.2.3 Shear effects on initial attachment 71

4.2.4 Gravitational settlement on initial attachment 75

4.2.5 Convective diffusion on initial attachment 77

4.2.6 Shear force and adhesion force 81

4.2.7 Interaction energy and attractive force based on the XDLVO theory 83

4.2.8 Summary 93

4.3 Corrosion of carbon steel and aluminum alloy in the presence of *Pseudomonas aeruginosa* and *Escherichia coli* biofilm 95

4.3.1 Introduction 95

4.3.2 Bacterial Attachments and Biofilm Formation 96

4.3.3 Corrosion Behaviors 100

4.3.4 Corrosion Rate 104

4.3.5 Summary 107

4.4 Corrosion behaviors of carbon steel C1010 and stainless steel 304 in the presence of iron oxidizing bacteria *Acidithiobacillus ferrooxidans* 108

4.4.1 Introduction 108

4.4.2 Initial attachments in flow chamber system 109

4.4.3 Bacterial attachment and biofilm formation 111

4.4.4 Corrosion evaluation 113

4.4.5 Potential mechanism 117

4.4.6 CS coupon corrosion characterization 123

4.4.7 Summary 125

4.5 Corrosion evaluations of aluminum alloy (Al 2024) in the presence of *Trichoderma reesei* and *Aspergillus niger* 127

4.5.1 Fungal attachment 127

4.5.2 Corrosion evaluation 129

4.5.3 Summary 130

CONCLUDING REMARKS 131

REFERENCES 135

APPENDIX 144

LIST OF TABLES

Table Page

4.1 The contact angles of water, methylene iodine, and ethylene glycol on the three bacterial lawns, zeta potential of PAO1, *P. putida* and *E. coli* in the medium suspension used for attachment study, and the equivalent bacterial size estimated from the AFM topographic scans are presented. Also presented are the surface energy and its components (LW and AB) of each surface of interests. 56

4.2 The values of and estimated using equations (2) and (3), respectively, are reported. 60

4.3 The secondary minima of interaction energies and the energy barriers between the secondary and primary minima of the three bacterial strains interacting with the two types of surfaces are summarized. For the three bacteria-glass combinations, primary minima were not found within the separation distance range ($d > d_0$). 60

4.4 The cells/particles gravitational settlement numbers N, ratios of cells/particles attachment to settlement (Ra) on both types of surface, the secondary energy minima (ΔG_{sm}^{XDLVO}) and the maximum attractive forces (F_{MAX}^{XDLVO}) estimated using the XDLVO theory, and critical shear stresses (σc)/forces ($F_{c-shear}$) determined experimentally are summarized. 76

4.5 Critical shear stress/force by deposition efficiency and experimental results. 80

4.6 The surface energies and their components of bacterial/particle lawns, the zeta potentials (ζ) and equivalent radius (*R*) of the bacteria/particles used in this study are summarized. Surface energy (γ) and its components (γ^{LW}, γ^{AB}, γ^{+}, and γ^{-}) are calculated based on contact angles of water, methylene iodide, and ethylene glycol formed on the lawns. 84

4.7 The table summarizes the average roughness (Ra) of Al and CS coupons prior to the runs, and of the coupons submerged 14 days in control flow chambers and in flow chambers with PAO1, and with *E. coli*. 102

4.8 The corrosion rate of CS coupons in control, with PAO1, and with *E. coli* after submerged in the flow chambers for 7 d and 14 d are presented. 106

4.9 Surface roughness of CS and SS in control, cell medium, and with cells systems prior to run, after 7 d, 14 d, 21 d, and 28 d's exposure, respectively. 116

A.1 The contact angles of the three probe liquids on the six surfaces along with surface energy and its components as well as zeta potential of BSA and the six substrate surfaces are summarized. 153

LIST OF FIGURES

Figure Page

2.1 pH growth profile of *T. reesei* RUT-C30 NRRL 11460 and *A. niger* NRRL 13201.. 18

2.2 Schematic of flow chamber system 18

2.3 Schematic of laser scanning confocal microscopy principle 21

2.4 Schematic of atomic force microscopy principle..... 24

3.1 (a). The picture of flow chamber is shown, together with Al thin film, Al coupon, and CS coupon, from left to right, inside. (b). The schematic of flow chamber system is shown. The dash line connection is for initial bacterial attachment. After 3 h, this connection is removed, and the chambers are connected to the flow through system (solid lines) for bacterial biofilm formation and metal corrosion study. 38

3.2 The schematic of static vessel system is shown..... 45

4.1 The initial attachments of three bacterial strains: PAO1, *P. putida* and *E. coli*, on the bottom surface of the glass chamber are shown. The error bars shown for each is the standard deviation value obtained for at least eight data points. 51

4.2 (a). The initial attachment of three bacterial strains: PAO1, *P. putida* and *E. coli*, on the bottom surface of the OTS modified glass chamber are shown. (b). To provide a better comparison of the hydrophobic effects of chamber wall, relative attachments of the initial attachment of PAO1, *P. putida* and *E. coli*, on the bottom surface of the OTS modified chambers to those on the un-modified glass surfaces are shown. The error bars shown for each is the standard deviation value obtained for at least eight data points. 53

4.3 (a). The attachment of the three bacterial strains on the OTS surface is shown to have a positive linear relationship with the hydrophobic partitioning of cells to the water-hexadecane interface. (b). The attachment of the three bacterial strains on the glass surface decreases with the increase of the hydrophobic partitioning of cells to the water-hexadecane interface. The error bars shown for each is the standard deviation value obtained for at least eight data points. 55

4.4 Atomic force microscopic (AFM) topography scans of the three bacterial strains. The length (L), width (W) and height (H) from the scans were utilized to estimate the equivalent radius, *R*, (by assuming the cell is spherical in shape) of the bacterial cell. The scan size for *E. coli* and *P. putida* is 3 x 3 mm2, and it is for 6 x 6 mm^2 PAO1 so the length of the flagella can be shown. The standard deviation value for each data point reported in the table is the results of at least ten cross-sectional measurements. 57

4.5 The total interaction energies, estimated by the XDLVO theory, vs. separation distance are shown for the PAO1-OTS combination (solid line), the *P. putida*-OTS combination (dotted line), the *E. coli*-OTS combination (dashed line) and the *E. coli*-glass combination (dashed-dotted line). While for the case of the OTS surface, the energy barriers for all three bacterial strains are resulted. The primary minima for the PAO1-OTS, *P. putida*-OTS, and *E. coli*-OTS combinations are not shown in the profiles, their values are -5116, -2774, and -8704 kT, respectively. For the case of the glass surface, only the secondary minima, at a distance of $d \geq d_0$, exist based on the calculation. The primary minima for all three bacteria-glass combinations would occur at $d < 0.015$ nm, which is outside the separation range ($d > d_0 = 0.158$ nm) we plotted. 61

4.6 The attachment number is plotted against the secondary energy minima of the three bacterial strains on the two types of surfaces. The error bars for each attachment number are the standard deviation value obtained for at least eight data points. 63

4.7 (a). The attachments of positively charged amidine latex (AL) PS particles on the surfaces of glass and OTS modified glass at the shear stress of 15 mN/m^2 are shown. (b). The attachments at the end of the 1^{st} hour (we defined this as the initial attachments) of four bacterial strains: PAO1, *P. putida*, *E. coli*, and *S. epidermidis*, on the surfaces of glass and OTS at a shear stress of 15 mN/m^2 are shown. The errors shown for each data point is the standard deviation obtained from at least four sets of measurements. 70

4.8 The initial attachments of particles on glass and the OTS surface under different shear stresses (0.1, 1, 2.5, 5, 15, 50, 150, 175, and 200 mN/m^2) for both positively charged and negatively charged (carboxylate modified latex, CML) PS particles are summarized. The errors shown for each data point is the standard deviation obtained from at least four sets of measurements. The arrows pointed out the maximum attachments occurred at the critical shear stresses. 73

4.9 (a). The initial attachments of four bacterial strains: PAO1, *P. putida*, *E. coli*, and *S. epidermidis*, on glass under different shear stresses (1, 2.5, 5, 15, 25, and 50 mN/m^2) are shown. (b). The initial attachments of PAO1, *P. putida*, *E. coli*, and *S. epidermidis* on the OTS surfaces under different shear stresses (1, 2.5, 5, 15, 25, 50 mN/m^2) are summarized. The errors shown for each data point is the standard deviation obtained from at least four sets of measurements. The arrows pointed out the maximum attachments occurred at the critical shear stresses. 74

4.10 The PS-AL deposition efficiency, on both glass and OTS surfaces, as a function of shear stress. The trendlines are added based on the deposition efficiency approach.80

4.11 Particle/cell adhesion process onto a substrate. 82

4.12 Schematic of forces applied on a particle/cell during attachment. 82

4.13 Atomic force microscopic (AFM) topography scans of the four bacterial strains: (a). PAO1, (b). *P. putida* (the inset is a more magnified AFM topographic scan showing EPS surrounding a cell when the cells are not washed prior to scanning), (c). *E. coli*, and (d). *S. epidermidis* are presented. The arrow in (a) pointed to a flagella that fell off the cell. Each of the scan is 3×3 mm^2, and the z-scale is 1000 nm. (e). The phase image (10×10 mm^2) of PAO1 and their flagella are presented. The harder deposits observed in the phase image could be salt aggregates formed as the medium dried up. 85

4.14 The XDLVO interaction energy curves of *S. epidermidis*, *P. putida*, and PS particles on (a). glass and (b). OTS surfaces are presented. 87

4.15 A series of representing images show the growth of attached PAO1 cells on Al thin film surfaces as the enriched medium flowed through the samples. Scale bars represent 50 μm. 98

4.16 (a). The surface coverage of PAO1 and *E. coli* vs. time is summarized. (b). PAO1 and *E. coli* biofilm thickness vs. time on CS coupon surface is presented. 99

4.17 The respective digital and optical microscope images of CS coupons in (a) & (e). control, (b) & (f). with PAO1, and (c) & (g). with *E. coli* after 14 days inside the flow chamber are presented. (d) is the optical microscope image of CS coupon prior to the run. Scale bars represent 5 mm in (a) – (c) and 50 μm in (d) – (g). 102

4.18 The 3-D laser scanning confocal microscopy images of PAO1 and *E. coli* biofilm stained with Live/Dead fluorescent stain solutions are presented. The green dots are live bacterial cells. 103

4.19 The dissolved oxygen (DO) level in the control system and underneath the PAO1 and *E. coli* biofilm are shown. 106

4.20 The initial attachments of *A. ferrooxidans* on the surfaces of CS, glass and OTS modified glass are shown. The errors shown for each data point is the standard deviation obtained from at least four sets of measurements. 110

4.21 (a)-(c). The fluorescent confocal images of attached *A. ferrooxidans* cells on CS coupon surfaces after 1 d, 7 d, and after rinsed with diluted basal salts solution, respectively. Scale bars represent 20 μm. (d)-(f). The fluorescent confocal images of attached *A. ferrooxidans* cells on SS coupon surfaces after 1 d, 7 d, and after rinsed with diluted basal salts solution, respectively. Scale bars represent 20 μm. (g). The

bacterial cell concentrations in bulk medium of with CS and SS coupon systems vs. time are presented. The errors shown for each data point is the standard deviation obtained from at least six sets of measurements. 112

4.22 (a). The weight loss of CS C1010 coupons exposed in control (pH ~ 2 DI water), cell medium (pH ~ 2), and in cell medium with cells (pH ~ 2) for 1, 3, 7, 14, 21, and 28 days are shown. The errors shown for each data point is the standard deviation obtained from at least eight sets of measurements. (b). The corrosion rate of CS C1010 coupons exposed in control, cell medium, and with cells, all started with a pH of ~ 2, for 1, 3, 7, 14, 21, and 28 days are shown. The errors shown for each data point is the standard deviation obtained from at least eight sets of measurements. 114

4.23 (a). The pH changes of acid/water, cell medium, and cell medium + cell culture with CS C1010 coupon in control, cell medium, and with cells systems, respectively, vs. time are shown. The errors shown for each data point is the standard deviation obtained from at least eight sets of measurements. (b). The pH changes of acid/water, cell medium, and cell medium + cell culture with SS 304 coupon in control, cell medium, and with cells systems, respectively, vs. time are shown. The errors shown for each data point is the standard deviation obtained from at least eight sets of measurements. 119

4.24 (a). The weight loss of CS C1010 coupons exposed in control and pH adjusted systems for 24 h are shown. The errors shown for each data point is the standard deviation obtained from at least eight sets of measurements. The insert is the corrosion rate of CS C1010 coupons exposed in control and pH adjusted systems for 24 h. The errors shown for each data point is the standard deviation obtained from at least eight sets of measurements. (b). The pH change of control and pH adjusted systems for 24 h are shown. 120

4.25 Schematic of the iron (Fe) reaction pathways of *A. ferrooxidans* with (a) Carbon steel C1010 and (b) Stainless steel 304. 121

4.26 (a). The digital images of CS coupons (from left) prior to run, in control, in cell medium, and with cells after 7 days, respectively, are shown. Scale bar represents 5 mm. (b). An optical microscope image of typical pitting corrosion of CS coupon in with cells system after 7 d is presented. Scale bar represents 100 μm. The inserts are the cross sections of the two main pits on the coupon surface. (c). The color converted 3-D image of (b) is shown. 124

4.27 (a) The fluorescent confocal image of Al 2024 surface in with *T. reesei* system after 7 days, after rinsed with DI water. Scale bars represent 100 μm. (b). The fluorescent confocal image of Al 2024 surface in with *A. niger* system after 7 days, after rinsed with DI water. Scale bars represent 100 μm. 128

A.1 Fluorescent microscope images of FITC-BSA adsorbed on (a). glass, (b). OTS, (c). PEG, (d). PS, and (e). PMMA surfaces are shown. (f) is the fluorescent image for

glass prior to adsorption. The pictures were taken under exactly same conditions (e.g. light intensity and exposure time). Scale bars represent 50 μm. 152

A.2 The normalized relative mean gray values of FITC-BSA on the six surfaces are shown. 153

A.3 The estimated DLVO and XDLVO interaction energy profiles between FITC-BSA and (a) glass and (b) PEG are presented. 155

A.4 The estimated DLVO and XDLVO interaction energy profiles between FITC-BSA and (a) OTS and (b) PMMA are presented. 156

CHAPTER I

INTRODUCTION

1.1 Importance of microbiologically influenced corrosion study

Corrosion is a natural but costly process, which is defined as the deterioration of a metal or its properties because of the reaction with its environment; it is estimated to cost 3.5 – 4.5 % of Gross Domestic Product (GDP) annually for the United States [1]. Microbiologically influenced corrosion (MIC) is one of the worst forms of corrosion. It could occur in environments where no corrosion is predicted, and the corrosion rates resulting from MIC can be extremely fast [2]. Flemming [3] suggested that about 20% of all corrosion on metallic material surfaces is related to MIC, and Booth [4] believed that 50% of corrosion failures in pipelines involved microbiology. The mechanisms involved in MIC are very complicated, since the procedure is affected by many elements, including formed biofilm structures, production of corrosive agents such as organic/inorganic acids and metal-binding effect of extracellular polymeric substances by microbial metabolism [5].

Generally speaking, the participation of microorganisms in the corrosion process includes initial attachment, biofilm formation, localized environment changing, and eventually, corrosion [6]. Initial microbial attachment is considered as the first step of MIC. The process of initial microbial attachment is complicated; it can be affected by

various physicochemical properties of both the microbial cells and the substrate surfaces [7]. During the past decades, the surface hydrophobicity/hydrophilicity, charge, and polarity of cells and the substrate surfaces have been considered as the primary factors of microbial attachment. Theories based on the adhesion/deposition of colloidal particles, especially the classical Derjaguin–Landau–Verwey–Overbeek (DLVO) [8, 9] and extended DLVO (XDLVO) models [10, 11], have been utilized to interpret initial microbial attachment.

In addition to the surface and medium properties, other factors such as the shear associated with flow conditions could also be one of the most important factors affecting initial microbial attachment [12]. Reports on the effects of shear on bacterial attachment have been contradictory [12-18]. Some reported that shear enhanced bacterial attachment [15-18], while others showed the opposite was true [12-14]. These studies also indicated that critical shear stresses were species and surface dependent. Most studies that investigated the shear dependency used relatively high shear stresses, and the critical shear was found to be in tens to thousands of mN/m^2. Others believed that the attachment behavior was dominated by the van der Waals, electrostatic and acid-base interactions considered in the DLVO and/or XDLVO theories [8-11, 19]. In general, such interactions are relatively weak; thus, the critical shear to overcome such interactions should be small.

As microbes attached and formed a biofilm on a metal surface, the localized environment of the metal surface is changed by the influence of microbial metabolism. A mature biofilm could prevent diffusion of oxygen or some other aggressive ions to the metal surface [6], or neutralize the corrosive elements present in the environment [20] to

inhibit metal corrosion. In this case, biofilm present on the metal surface plays a protective role and inhibits metal surface corrosion.

More aggressive metal corrosion microbes, such as iron-oxidizing bacteria (FeOB), acid-producing bacteria (APB)/fungi, and sulfate-reducing bacteria (SRB) could utilize metal as an energy source to survive and lead to corrosion. Iron-oxidizing bacteria (FeOB) induced aerobic corrosion has been suggested as a significant portion of MIC [21], and the presence of FeOB has been identified from different environments including water tanks [22] and pipelines [23]. One FeOB species, *Acidithiobacillus ferrooxidans* [24], is found to play an important role in metal oxidative activities [25]. However, there are still many unknowns on the exact role of FeOB in carbon steel corrosion [26]. Some attributed the corrosion to the crevice corrosion mechanism, which is related to the formed $Fe(OH)_3$ precipitation layer by FeOB cells and the environment aerobic condition [27, 28].

In addition to bacteria, fungi have also been found in corrosion sites. Acid-producing fungi are considered a main cause of microbial corrosion of aluminum alloy. A large number of fungi, such as *Aspergillus niger*, were isolated and identified from those corrosion products. However, the real role of acid-producing fungi played in MIC is a topic that is still under debate [29, 30].

1.2 Objectives of research

The main objectives of this study include:

- To evaluate the effects of microbial attachment and biofilm formation on MIC.

- To evaluate the effect of cells and substrate surface properties on initial bacterial attachment.
- To verify whether or not the XDLVO theory is applicable in predicting the shear dependent behaviors of initial bacterial attachment.
- To examine the corrosion behaviors of carbon steel and aluminum alloy in the presence of two common bacterial strains, *Pseudomonas aeruginosa* PAO1 and *Escherichia coli*.
- To study the role of iron-oxidizing bacteria (*A. ferrooxidans*) in carbon steel and stainless steel corrosion behaviors and to elucidate a potential mechanism of iron corrosion associated with *A. ferrooxidans*.
- To investigate the effects of *Trichoderma reesei* and *Aspergillus niger* on aluminum alloy corrosion.

1.3 Overview of the dissertation

The outline of this dissertation is as follows: In this chapter, the importance of the MIC study and the main objectives of this work are presented. Chapter II will present the background information on microbiologically influenced corrosion, the DLVO and XDLVO theories, shear effect on bacterial attachment, seven species of microbes used in this study (*Pseudomonas aeruginosa* PAO1, *Escherichia coli*, *Pseudomonas putida, Staphylcoccus epidermidis, A. ferrooxidans, Trichoderma reesei*, and *Aspergillus niger*), and characterization techniques utilized in the experimental section. Chapter III will provide the details on the materials, equipment, and procedures utilized in this work. Chapter IV will describe the results and discussion of effects of cells and substrate

surface properties and shear stress on initial bacterial attachment, corrosion behaviors of carbon steel, aluminum alloy, and stainless steel in the presence of *P. aeruginosa* PAO1, *E. coli*, *A. ferrooxidans, T. reesei* and *A. niger*. Chapter V will conclude this study along with suggestions for future work.

CHAPTER II

BACKGROUND

In this chapter, background information on microbiologically influenced corrosion will be provided in Section 2.1; the DLVO and XDLVO theories will be explained in Section 2.2; current studies of shear effect on bacterial attachment will be addressed in Section 2.3; basic information of seven species of microbes: *Pseudomonas aeruginosa* PAO1, *Escherichia coli*, *Pseudomonas putida, Staphylcoccus epidermidis, Acidithiobacillus ferrooxidans, Trichoderma reesei*, and *Aspergillus niger* will be described in Section 2.4; the information of flow chamber system will be provided in Section 2.5; and the background about main characterization techniques is reviewed in Section 2.6.

2.1 Microbiologically influenced corrosion

Corrosion, which is defined as the deterioration of a substance (usually a metal) or its properties because of a reaction with its environment, is a natural and costly process of destruction [31]. According to the estimation by Koch et al. [1], the direct cost of metallic corrosion is $276 billion, in 1998, on an annual basis for the United States, which represents 3.5 – 4.5 % of Gross Domestic Product (GDP). Corrosion causes costly, untimely, and dangerous failures of facilities, equipment and devices becomes a safety

hazard, and ultimately it could have devastating impacts on economy and resources. While most materials, including ceramics, polymers, semiconductors, are all susceptible to corrosion, corrosion for metals and metal alloys has been the primary concern.

Microbiologically influenced corrosion (MIC), which is the corrosion resulting from the presence and activities of microorganisms [32], is considered as one of the worst forms of corrosion for metals. Researchers attributed that about 20% of the all corrosion of metallic material surfaces to MIC [4], and suggested that about 50% of corrosion failures in pipelines involved microbiology [3]. MIC has been documented for metals exposed to seawater, freshwater, distilled and demineralized water, process chemicals, foodstuffs, soil, oil, gasoline and aircraft fuels, human plasma, and sewage [2]. According to the surveys, the industries most affected by MIC are power generation; oil production, transportation, and storage; and water distribution. Recently, MIC is recognized as a potential problem in long-term nuclear waste storage. MIC occurs in environments where corrosion will not be predicted and normally the rates can be extraordinarily high. MIC can produce many types of corrosion on the metal-biofilm interface by the reaction driven by biofilm. Mostly, MIC can cause localized corrosion and can take the form of pitting, crevice corrosion, under-deposit corrosion, and de-alloying, in addition to enhance galvanic and erosion corrosion [2, 33]. The initial stages of microbe attachment and interaction with metal surfaces serve as a precursor to MIC. Some researches have investigated the initial attachment of algae, invertebrate shells and some non-MIC-relevant bacteria to various ceramic and polymer surfaces. Meanwhile, some researches have proposed mechanisms that how MIC-relevant bacteria accelerate/inhibit metal corrosion. However, few studies have been completed related to the initial MIC

hazardous bacterial attachment on metal surfaces in natural environment or industrial processes where MIC is a serious issue. Some of the MIC corrosion reactions are still under debate, and the relationship between biofilm structures and corrosion behaviors have not been extensively studied [34-37].

2.2 The DLVO and XDLVO theories

The classical Derjaguin–Landau–Verwey–Overbeek (DLVO) theory was originally developed to describe the forces between two charged surfaces in a liquid medium [8, 9]. In theory, two main interactions, the attractive Lifshitz van der Waals (LW) (ΔG^{LW}) and the repulsive electrostatic double layer (EL) (ΔG^{EL}) interactions are included in the theory as a function of separation distance to quantitatively calculate the actual adhesion energy variations involved in colloidal adhesion and aggregation. It is expressed as:

$$\Delta G^{Tot}(d) = \Delta G^{LW}(d) + \Delta G^{EL}(d) \quad (1)$$

where ΔG^{Tot} is the total free energy of interaction, ΔG^{LW} is the attractive van der Waals free energy of interaction (negative), and ΔG^{EL} is the repulsive electrostatic free energy of interaction (positive).

To account for the potential hydrogen bonds, which are common when a bacterial cell interacts with an oxidized or hydrophilic surface, van Oss et al. [10, 11] added the short-range Lewis acid-base (AB) interactions in the XDLVO theory. The LW and AB interactions between a layer of bacteria cells (1) and a flat substrate surface (2) in a medium (3) with a minimum equilibrium distance d_0 (~ 0.158 nm, the critical distance

below which the outer electron shells of adjoining non-covalently interacting molecules would overlap [38, 39]) can be expressed as [7, 40]:

$$\Delta G_{d_0}^{LW} = -2\left(\sqrt{\gamma_3^{LW}} - \sqrt{\gamma_2^{LW}}\right)\left(\sqrt{\gamma_3^{LW}} - \sqrt{\gamma_1^{LW}}\right) \tag{2}$$

$$\Delta G_{d_0}^{AB} = 2\left(\sqrt{\gamma_1^+\gamma_3^-} + \sqrt{\gamma_2^+\gamma_3^-} + \sqrt{\gamma_1^-\gamma_3^+} + \sqrt{\gamma_2^-\gamma_3^+} - \sqrt{\gamma_1^+\gamma_2^-} - \sqrt{\gamma_1^-\gamma_2^+} - 2\sqrt{\gamma_3^+\gamma_3^-}\right) \tag{3}$$

where γ_i^{LW}, γ_i^+ and γ_i^- denote the Lifshitz-van der Waals component, electron-acceptor (acid) and electron-donor (base) of the Lewis acid-base component of the surface energy (i.e. $\gamma_i = \gamma_i^{LW} + \gamma_i^{AB}$, and $\gamma_i^{AB} = 2(\gamma_i^+ \gamma_i^-)^{1/2}$).

When a single bacterial cell, assuming it is rigid and perfectly spherical, is involved, the LW, AB and EL interaction energy in a medium can be modified to [7, 41]:

$$\Delta G_{bms(d)}^{LW} = -\frac{AR}{6d} \tag{4}$$

$$\Delta G_{bms(d)}^{AB} = 2\pi R \lambda \Delta G_{d_0}^{AB} \exp\left(\frac{d_0 - d}{\lambda}\right) \tag{5}$$

$$\Delta G_{bms(d)}^{EL} = \pi R \varepsilon \varepsilon_o \left(2\psi_{01}\psi_{02} \ln\left(\frac{1+e^{-\kappa d}}{1-e^{-\kappa d}}\right) + \left(\psi_{01}^2 + \psi_{02}^2\right)\ln\left(1-e^{-2\kappa d}\right)\right) \tag{6}$$

A is the un-retarded sphere-substrate Hamaker constant in water. R is the bacterial mean radius. d is the separation distance between the bacterial cell and the flat substrate. λ is the characteristic decay-length of AB interaction in water (~ 0.6 nm [42]). ε and ε_o are the relative dielectric permittivity of medium and the permittivity in a vacuum, respectively. $1/\kappa$ is the Debye-Huckel length (or the electric double layer thickness); κ (m^{-1}) is related to the ionic strength, I (M), of the medium by $\kappa = 3.28 \times 10^9 I^{1/2}$. ψ_{01} and ψ_{02} are the surface potentials of bacterial cell and the chamber wall, respectively, which

are correlated to their zeta potentials (ζ_1 and ζ_2). For cells, $\psi_{01} = \zeta_1\left(1+\frac{z}{R}\right)\exp(\kappa z)$, where z is the slipping distance having a value of ~0.3 nm [43]. For the chamber wall, $\psi_{02} \approx \zeta_2$. The subscript b, m and s represent a single bacterial cell, the medium, and the flat substrate, respectively.

Then the extended DLVO theory can be expressed as:

$$\Delta G^{Tot}(d) = \Delta G^{LW}(d) + \Delta G^{AB}(d) + \Delta G^{EL}(d) \quad (7)$$

The DLVO theory and, especially, the XDLVO theory were found to adequately interpret the initial microbial adhesion in many studies [7, 44-46], on substrates of different hydrophobicity and in both static and flow systems. There were also studies where the experimental results could not be directly explained by the XDLVO theory [47, 48]. For these studies, some specific events or properties, such as the formation of polymeric bridges, significant deviation of the bacterial cells from a round shape to an elongated shape, or cell surface heterogeneity, were believed to be the causes. When such causes were properly accounted for, e.g., by adjusting the cell radius for a non-spherical cell, and/or alternating the overall cell surface properties from the contribution of the cell surface structures/exopolymers, the XDLVO theory was generally valid for interpreting bacterial attachment.

In addition to bacterial cell properties, as shown in equations (2) to (6), the medium conditions also affect the overall interaction energy and its components. The surface energy and its components, as well as the zeta potential of the medium are all varying with the individual nutrient concentrations, pH and ionic strength of the medium. These medium conditions also affect the properties of cells. Substances in the medium,

especially the dissolved organic matter, could adsorb to the cell and/or substrate surfaces, thus affecting the initial attachment behaviors [45, 47, 49].

2.3 Current studies of shear effect on bacterial attachment

Reports on the effects of shear on bacterial attachment have been contradictory [12-18]. Some reported that shear enhanced bacterial attachment [15-18], while others showed the opposite was true [12-14]. Thomas et al. [15, 50] studied the attachment of *Escherichia coli* expressing adhesin FimH in flow chambers and reported that increased shear could enhance the binding of FimH to cell surface receptors by a catch-bond mechanism, thus increasing number of *E. coli* attaching to cell surfaces. On the other hand, several studies [12-14] on shear effects on the attachment of various bacteria found that as shear stress increased, the bacterial attachment decreased. Roosjen et al. [14] hypothesized that the attractive force of microorganisms, even for those already attached at low shear, was too weak to resist the increasing shear. Nejadnik et al. [13] and Park et al. [12] also proposed that the decrease of bacterial attachment was caused by the shear stress exceeding the critical value needed to detach attached cells. These studies also indicated that critical shear stresses were species and surface dependent. For example, the critical shear stress for *Staphylococcus aureus*, *Pseudomonas aeruginosa*, and *Staphylococcus epidermidis* were found to be 1000, 1100, and 2700 mN/m^2, respectively on pristine silicone rubber surface [13], but in another study, the critical shear stress for *P. aeruginosa* was found to be only 17 mN/m^2 on glass [12]. Also the critical shear stress was noticed to depend on the suspending medium [51]. In a phosphate-buffered saline

(PBS) with pH 7.4, the critical shear stress for attachment of *S. epidermidis* cells on glass was only about half of the critical value in the PBS with pH 6.8 [14, 52].

Most studies that investigated the shear dependency used relatively high shear stresses, and the critical shear was found to be in tens to thousands of mN/m^2. Busscher and van der Mei [53] demonstrated that the critical shear stress was related to the attractive forces (10^{-13} to 10^{-15} N) between the bacterial cells and the substrate, and the critical shear stress was relatively low (less than 10 mN/m^2). In our recent study [54] on the effects of rhamnolipids and shear on the initial attachment of *P. aeruginosa* PAO1 on glass under slow flows, it was observed that a shear stress as low as ~ 5 mN/m^2 could prevent cells from attachment. Recently, Boks et al. [55] pointed out that there were two critical shear stresses involved in bacterial attachment. One was for preventing attachment and the other was for detaching already attached cells, and the critical shear stress for detachment could be two to three orders of magnitude higher than that for preventing attachment. This could be the reason why very different critical shear stress values have been reported by different researchers.

While bacterial cells might attach onto a surface by forming specific bonds [56], such as receptor-ligand bonds, and result in firm attachment; most attachment behaviors could likely be initiated by the attractive interactions resulted from van der Waals, electrostatic and acid-base interactions considered in the DLVO and XDLVO theories [8-11, 19]. In general, such interactions are relatively weak; thus, the critical shear to overcome such interactions, i.e. to prevent attachment, could be small.

2.4 Microbial species

In this section, background information of seven species of microbes utilized in this study: *Pseudomonas aeruginosa* PAO1, *Escherichia coli*, *Pseudomonas putida, Staphylcoccus epidermidis, Acidithiobacillus ferrooxidans, Trichoderma reesei*, and *Aspergillus niger* are provided.

2.4.1 *Pseudomonas aeruginosa* PAO1

Pseudomonas aeruginosa is a unipolar in motility, Gram-negative, aerobic, rod shaped (0.5 to 0.8 μm in diameter and 1.5 to 3.0 μm in length) bacterium that grow in soil, marine environments, and on plant and animal tissues. *P. aeruginosa* is opportunistic pathogen of plants as well as human beings [57]. *P. aeruginosa* exists in nature in two forms, planktonic form and biofilm form. In the planktonic form, because of the polar flagella, bacterial cells are in highly mobile. Formation of the biofilm is attributed to the interaction of flagella with the substrate surfaces, which cause the bacterial cells to attach and develop into a biofilm [58]. *P. aeruginosa* has a very simple nutritional requirements. In the laboratory, *P. aeruginosa* can be grown in medium that contains acetate and ammonium sulfate. The *P. aeruginosa* strain PAO1 is able to degrade aromatic hydrocarbons, and produce rhamnolipids [59].

2.4.2 *Escherichia coli*

Escherichia coli is a Gram-negative, rod shaped (0.5 μm in diameter and 2 μm in length) bacterium, which is commonly found in the intestine of endotherms. Most *E. coli* strains are nonpathogenic, which are part of the normal flora of the gut, can produce

vitamin K_2 for their hosts [60]. *E. coli* is versatile and well-adapted to its characteristic habitats. It can grow in aerobic and can survive in anaerobic conditions, can produce "mixed acids and gas" as end products by the process of fermentation under anaerobic conditions. Also they can respond to the changes in the environment such as pH, temperature, osmolarity, *etc*., in some remarkable ways. *E. coli* strains that possess peritrichous flagella can swim by rotating long thin helical filaments and are motile [61]. The filaments can form bundles that drive the cells forward. Some *E. coli* strains have been noticed to glide over surfaces by extending and retracting pili, which are thin filament like structures that can stick to the substrate surface [62].

2.4.3 *Pseudomonas putida*

Pseudomonas putida is a Gram-negative, aerobic, rod-shaped (0.5 to 0.8 μm in diameter and 2 to 3.0 μm in length), saprotrophic soil bacterium, which is capable of the typical *Pseudomonas* bacterial cells' motility with the function of one or more polar flagella [63]. *P. putida* is capable of growing on aromatic hydrocarbons such as benzene, toluene, ethylbenzene, n-propylbenzene, n-butylbenzene and cumene by taking those organic solvents as the sole carbon and energy sources. By this ability, *P. putida* can clean the organic pollutants in the soil. In this case, *P. putida* become an inexpensive choice to purify fuel in the petroleum industry [64]. Also, *P. putida* strains are safe strains of bacteria, which were believed to be nonpathogenic as it lacks the genes and enzymes to digest the membrane of cells [63].

2.4.4 *Staphylcoccus epidermidis*

Staphylcoccus epidermidis is a Gram-positive, cocci (1-2 μm in diameter), hardy, non-motile, facultative anaerobic bacterium that can survive by aerobic respiration or by fermentation. It is a common inhabitant of the skin and mucosa and the most frequent cause of hospital-acquired infections. *S. epidermidis* causes infection only in immunocompromised individuals or after damage to the epithelium [65]. *S. epidermidis* is able to reduce nitrate and produce phosphatase, and produce acid aerobically from glucose, fructose, maltose, sucrose, and glycerol [66]. In the application of biotechnology part, recombinant lipases from *S. epidermidis* is utilized as a catalyst to synthesize different flavor esters in aqueous environment without organic solvent, which can avoid the problem of toxicity and flammability of organic solvent, simplify the product purification conditions, and lower the cost [67].

2.4.5 *Acidithiobacillus ferrooxidans*

Acidithiobacillus ferrooxidans is a Gram-negative, aerobic, rod shaped (0.6 to 1.0 μm in diameter and 1.0 to 1.6 μm in length), chemoautotrophic, and acidophilic iron oxidizing bacterium [68]. *Acidithiobacillus ferrooxidans*[24] plays an important role in metal oxidative activities [25]. The species utilizes ferrous (Fe(II)) as the sole energy source for CO_2 fixation at an acidic condition with a pH range from 2.0 to 4.5 [68].

The basic reactions couple the oxidation of Fe(0) to the reduction of oxygen at the surface of the iron [69] as:

$$2Fe + O_2 + 2H_2O \longrightarrow 2Fe^{2+} + 4OH^- \quad (8)$$

$$4Fe^{2+} + O_2 + 2H_2O \longrightarrow 4Fe^{3+} + 4OH^- \quad (9)$$

After Fe(II) oxidized to ferric (Fe(III)), amorphous $Fe(OH)_3$ precipitates formed at a pH ~2 condition as shown below:

$$Fe^{3+} + 3H_2O \longrightarrow Fe(OH)_3 \downarrow + 3H^+ \quad (10)$$

The reaction coupled with the metabolism of *A. ferrooxidans* metabolism to achieve:

$$24Fe^{2+} + 6CO_2 + 24H^+ \longrightarrow 24Fe^{3+} + C_6H_{12}O_6 + 6H_2O \quad (11)$$

Reaction (9) is the rate-limiting step, occurs very slow especially under a low pH condition [70]. But in the presence of *A. ferrooxidans*, the oxidation rate of Fe(II) to Fe(III) could increase by 500,000 times at a pH ~2 condition [71].

2.4.6 *Trichoderma reesei*

Trichoderma reesei is a mesophilic, filamentous, soft-rot ascomycete (~ 8 μm in diameter and 10 mm in length for hyphae size) fungus. In industry, *T. reesei* is widely used as a source of cellulases and hemicellulases for the hydrolysis of cellulose, a major component of plant biomass, into glucose. Meanwhile, *T. reesei* is capable of hydrolyzing biomass polysaccharides for producing bioethanol and a range of organic acids [72]. With sufficient cellulose provided, *T. reesei* can decrease and maintain the pH to around 3 (Figure 2.1) by producing of acetic acid in the medium [73].

2.4.7 *Aspergillus niger*

Aspergillus niger is a haploid filamentous (range from 900-1600 μm in length and 40-60 μm in diameter for conidiophores) fungus. In the field of biotechnology, *A. niger* is

widely used for the production of food ingredients, pharmaceuticals, industrial enzymes, and especially, organic acids, such as citric acid and gluconic acid. *A. niger* shows a extraordinary versatile metabolism, allowing to grow on various substrates under different environmental conditions [74]. Under laboratory condition, *A. niger* is able to produce citric acid and lower the medium pH to around 2.5 (Figure 2.1). Reports shown that *A. niger* involved in the corrosion activity on aluminum and its alloys, and accelerated corrosion behavior by its metabolism, while the actual mechanism was still unclear [29, 30]. However, contradictory results also shown that *A. niger* acted as corrosion inhibitor on aluminum [75, 76].

2.5 Flow chamber system

The flow chamber allows studying microbial adhesion in which initial bacterial attachment and biofilm formation can be monitored *in situ* [77]. Also, the flow rate of the bacterial suspension, one of the most important parameters in the initial attachment of bacteria to surfaces [78], can be easily adjusted via the flow systems. The flow rate can be estimated to be similar to those of the slow flowing streams or waves brushing against stationary structures. Furthermore, a flow chamber system allows more consistent and reproducible bacterial attachment results to be obtained [54].

In this study, the flow chamber system consists of a reservoir flask with bacterial suspension, a reservoir flask with 0.5% fresh saline solution, a constant pump, a rectangular glass chamber and some pieces of silicone tubing (Figure 2.2). Silicone tubing is utilized to connect the whole system. During the experiment, the bacterial suspension will be continuously circulated between the reservoir flask and the glass

chamber, where cells attachment will be observed. The saline solution will be used to rinse off loosely attached cells inside the glass chamber.

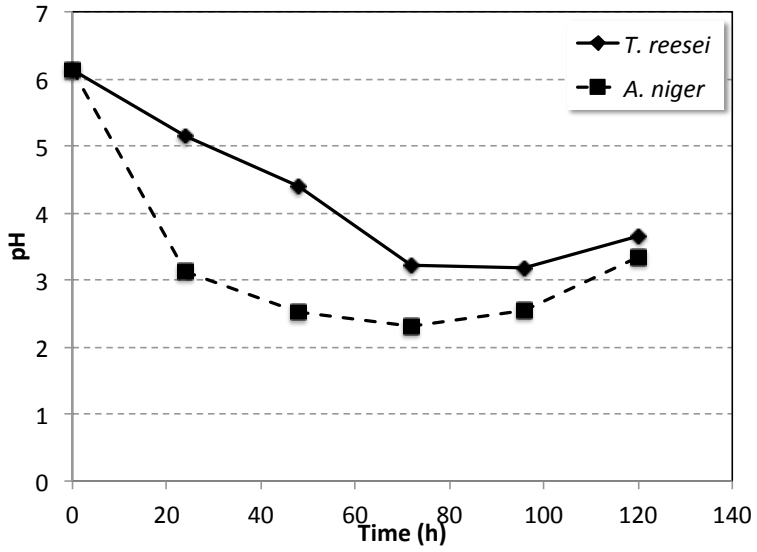

Figure 2.1 pH growth profile of *T. reesei* RUT-C30 NRRL 11460 and *A. niger* NRRL 13201.

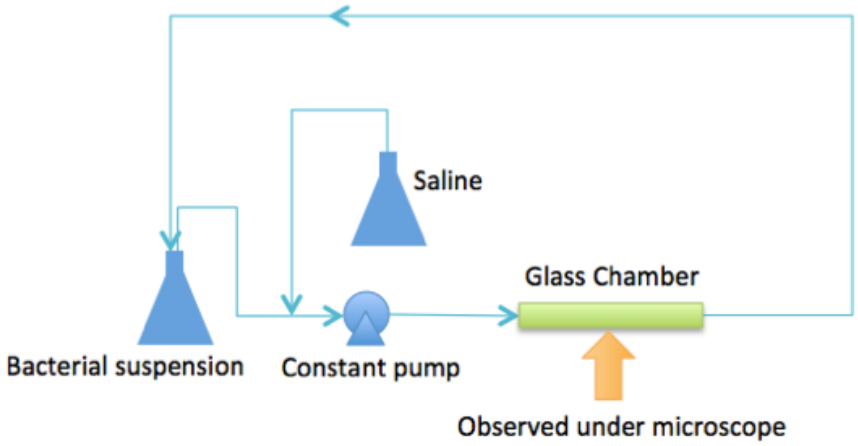

Figure 2.2 Schematic of flow chamber system

2.6 Background on Characterization Techniques

In this work, four main characterization techniques are used, including laser scanning confocal microscopy (LSCM, confocal), InfiniteFocus microscopy (IFM), atomic force microscopy (AFM), and standard test method for corrosivity of water in the absence of heat transfer (weight loss method ASTM D2688). The basic mechanisms and calculations are described in detail in sub-sections.

2.6.1 Laser scanning confocal microscopy

Laser scanning confocal microscopy (LSCM or CLSM) is a technique for obtaining high-resolution optical images with depth selectivity [79]. The basic key to the confocal approach is its ability to acquire in-focus images from selected depths, a process known as optical sectioning. Images are acquired point-by-point and reconstructed with a computer, allowing three-dimensional reconstructions of topologically complex objects.

There has been a tremendous explosion in the popularity of confocal microscopy in recent years, due in part to the relative ease with which extremely high-quality images can be obtained from specimens prepared for conventional fluorescence microscopy, and the growing number of applications in cell biology that rely on imaging both fixed and living cells and tissues. In fact, confocal technology is proving to be one of the most important advances ever achieved in optical microscopy [80].

The confocal principle in epi-fluorescence laser scanning microscopy is diagrammatically presented in Figure 2.3. Coherent light emitted by the laser system passes through a pinhole aperture that is situated in a conjugate plane (confocal) with a scanning point on the specimen and a second pinhole aperture positioned in front of the

detector (a photomultiplier tube). As the laser is reflected by a dichromatic mirror and scanned across the specimen in a defined focal plane, secondary fluorescence emitted from points on the specimen (in the same focal plane) pass back through the dichromatic mirror and are focused as a confocal point at the detector pinhole aperture. The significant amount of fluorescence emission that occurs at points above and below the objective focal plane is not confocal with the pinhole and forms extended Airy disks in the aperture plane. Because only a small fraction of the out-of-focus fluorescence emission is delivered through the pinhole aperture, most of this extraneous light is not detected by the photomultiplier and does not contribute to the resulting image. The dichromatic mirror, barrier filter, and excitation filter perform similar functions to identical components in a wide-field epi-fluorescence microscope. Refocusing the objective in a confocal microscope shifts the excitation and emission points on a specimen to a new plane that becomes confocal with the pinhole apertures of the light source and detector [80].

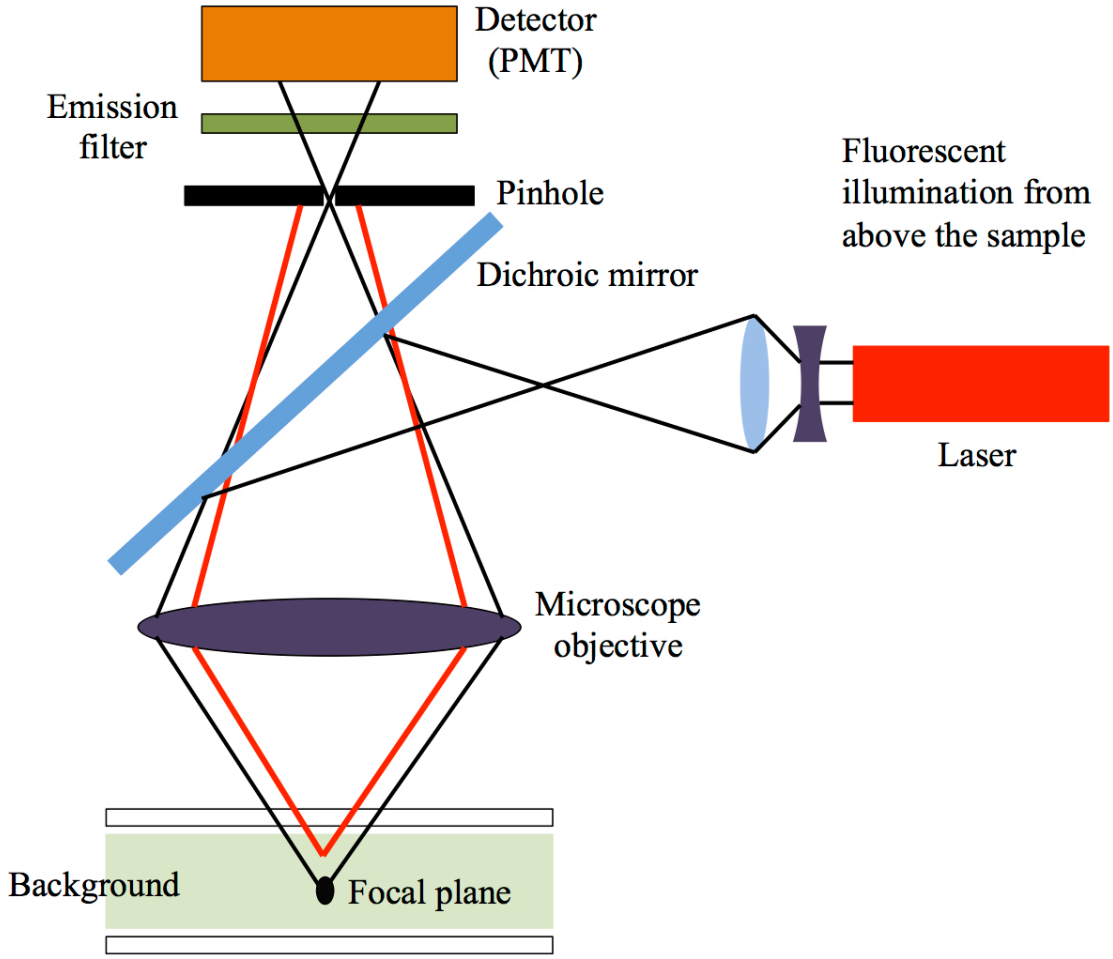

Figure 2.3 Schematic of laser scanning confocal microscopy principle

2.6.2 InfiniteFocus microscopy

The InfiniteFoucus microscopy (IFM) is an optical device for 3D surface measurement. The system provides the functionalities of an optical profiler and a micro coordinate measurement device in one system. This allows the measurement of form and roughness plus a full range of surface characterization in a single measurement. A vertical resolution of up to 20 nm is achieved even on large vertical and lateral scanning areas. Complex forms of solid and compound material with varying reflection properties are measured in the same high vertical resolution. With InfiniteFocus, small ultra precision tools are as easily measured as micro and nano structures on large components. The measurement of micro components is performed in the same high resolution as form and roughness of a gear wheel in the meter-range. Requirements regarding meaningful investigations of tribological and corrosive mechanics are easily achieved as well. Additionally, wear analysis and the measurement of form deviations to reference geometry or a CAD data set are other typical measures in industrial quality assurance that are provided by the system. InfiniteFocus is based on of Focus-Variation. Its operating principle combines the small depth of focus of an optical system with vertical scanning to provide topographical and color information from the variation of focus [81].

2.6.3 Atomic force microscopy

Atomic force microscopy (AFM) is one kind of scanning probe microscopy (SPM). SPM is a general term referring to surface characterization techniques that utilize probes in close proximity to the sample surface. They are designed to measure local properties with a probe, such as height, magnetism, and friction. Topography

characterization is perhaps the most common use of SPM techniques. The AFM is an invaluable tool not only to obtain high-resolution topographical images, but also to determine certain physical properties of specimens, such as their mechanical properties and composition. In addition to the wide range of applications, from materials science to biology, this technique can be operated in a number of environments as long as the specimen is attached to a surface, including ambient air, ultra high vacuum, and most importantly for biology, in liquids [82].

Like all other SPM, the AFM utilizes a sharp probe moving over the surface of a sample in a raster scan. In the case of the AFM, the probe is a tip on the end of a cantilever which bends in response to the force between the tip and the sample. Figure 2.4 demonstrates the basic principle of AFM operation. As the cantilever flexes, the light from the laser is reflected onto the split photo-diode. By measuring the difference signal, changes in the bending of the cantilever can be measured. Since the cantilever obeys Hooke's Law for small displacements, the interaction force between the tip and the sample can be detected. The movement of the tip or sample is performed by an extremely precise positioning device made from piezoelectric ceramics, most often in the form of a tube scanner. The scanner is capable of sub-angstrom resolution in x-, y- and z-directions. The z-axis is conventionally perpendicular to the sample. A feedback loop is used to maintain either a constant deflection (contact mode) or oscillatory amplitude (tapping mode) of the cantilever. The mirror is used to increase the path length between the cantilever and the detector in order to amplify deflections of the laser beam [83, 84].

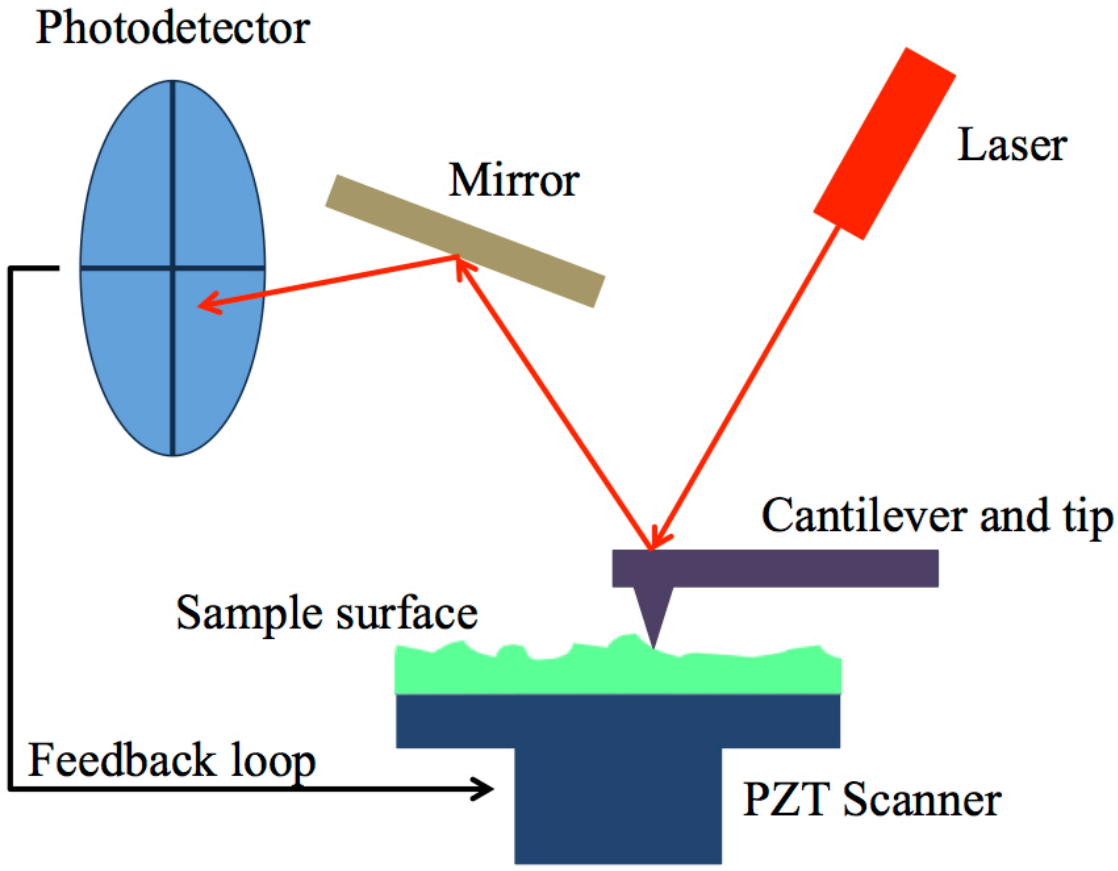

Figure 2.4 Schematic of atomic force microscopy principle

2.6.4 Standard test method for corrosivity of water in the absence of heat transfer [85]

Standard test method for corrosivity of water in the absence of heat transfer (weight loss method ASTM D2688) is a test method covers the determination of the corrosivity of water by evaluating pitting and by measuring the weight loss of metal specimens. Pitting is a form of localized corrosion; weight loss is a measure of the average corrosion rate. The rate of corrosion of a metal immersed in water is a function of the tendency for the metal to corrode and is also a function of the tendency for water and the materials it contains to promote (or inhibit) corrosion. This method employs flat, rectangular-shaped metal coupons which are mounted on pipe plugs and exposed to the water flowing in metal piping in municipal, building, and industrial water systems using a side stream corrosion specimen rack.

Since the two tendencies are inseparable for a metal to corrode and for water and the materials it contains to promote or inhibit corrosion, the corrosiveness of a material or the corrosivity of water must be determined in relative, rather than absolute, terms. The tendency for a material to corrode is normally determined by measuring its rate of corrosion and comparing it with the corrosion rates of other materials in the same water environment. Conversely, the relative corrosivity of water may be determined by comparing the corrosion rate of the same material in other waters. Such tests are useful, for example, for evaluating the effects of corrosion inhibitors on the corrosivity of water. Although this test method is intended to determine the corrosivity of water, it is equally useful for determining corrosiveness and corrosion rate of materials. Examples of systems in which this method may be used include but are not limited to open recirculating cooling water and closed chilled and hydronic heating systems.

CHAPTER III

EXPERIMENTAL APPROACH

In this chapter, the essential details about the materials and equipment used, methods adopted while preparing and inoculating the bacterial cell culture for flow chamber systems and corrosion evaluation, and procedures for substrate surface sample preparation, processing, and characterization are provided.

3.1 Materials and Equipment

Sulfuric acid (98% H_2SO_4), H_2O_2 (30% technical grade), agar, Polystyrene (PS), hexane (HPLC grade), $(NH_4)_2SO_4$, KCl, K_2HPO_4, $Ca(NO_3)_2$, $FeSO_4 \cdot 7H_2O$, ethanol, and 20 mL Disposable Scintillation Vials were all purchased from Fisher Scientific; *n*-Octadecyltrichlorosilane ($CH_3(CH_2)_{17}SiCl_3$, OTS), 2-[methoxy-poly(ethyleneoxy)propyl]trimethoxysilane ($CH_3O(CH_2CH_2O)_{6\text{-}9}\text{-}(CH_2)_3Si(OCH_3)_3$, PEG-silane, M_w = 460-590 g/mol) were purchased from Gelest; Poly(dimethylsiloxane) (PDMS) Sylgard® 184 was from DowCorning. Poly(methyl methacrylate) (PMMA) and aluminum (Alloy 2024) were from McMaster-Carr; Bovine serum albumin labeled with fluorescein isothiocyanate (FITC-BSA), methylene iodide (99%), ethylene glycol (99.8%), and hexadecane (99+%) were from Sigma-Aldrich; tryptic soy broth (TSB) medium was from MP Biomedicals, LLC; glycerol (99+%) was from Acros Organics;

Nylon filters (pore diameter, 0.22 mm; filter diameter, 47 mm) were purchased from GE Water & Process Technologies. Glass slides (25 mm × 75 mm × 1 mm) were purchased from VWR. Carbon steel (C1010) and aluminum (Alloy 3003 H14) were purchased from Q-Lab Corporation; FilmTracer Live/Dead biofilm viability kit fluorescent staining solutions and Polystyrene (PS) microspheres (0.51 μm in diameter) were from Invitrogen. MgSO4•7H_2O was from Sigma-Aldrich; Deionized (DI) water was purified in-house and had a conductivity of ~0.1 S or less.

The microorganisms used were *Pseudomonas aeruginosa* PAO1 (ATCC 15692), *Pseudomonas putida* (NRRL B-14938), *Escherichia coli* (ATCC 11303), *Staphylcoccus epidermidis*, *Acidithiobacillus ferrooxidans* (ATCC 23270), *Trichoderma reesei* RUT-C30 (NRRL 11460), and *Aspergillus niger* (NRRL 13201). The equipment used included a vacuum oven (Model No. 5831, National Appliance), magnetic stir plates (Corning), a hot/stir plate (VWR Scientific), a shaker incubator (Innova 4080, New Brunswick Scientific Co.), a standard analog shaker (Model 1000, VWR), an electric pressure steam sterilizer (Model 25X, All American), glass chambers (LRT-2-12-120 and BST-10-90, Friedrich & Dimmock, Inc.), a UV-vis spectrophotometer (Model 1601, Shimadzu), peristaltic pumps (Masterflex L/S, Cole Parmer Instrument Company), a Rame-Hart contact angle goniometer (Model 100-00), a Malvern Zetasizer (ZEN3600, Nano series), two centrifuges (Sorvall RC 5C plus, DuPont; and Model 5415D, Eppendorf), an atomic force microscope (AFM) (MultiMode SPM, Digital Instruments), an infinitefocus microscope (IFM, Alicona) and IF-MeasureSuite (Version 4.1, Alicona), a dissolved oxygen sensor (Fibox 3-trace v3, PreSens), a balance (E1RR80, Ohaus), a pH meter (Education, Fisher Scientific), 0.22 μm filters (Express Plus, Millipore), a laser scanning

confocal microscopy (FV1000, Olympus) with an optical microscope (BX61W1, Olympus), and an optical microscope (IX70, Olympus) with a CCD camera (XC-ST70, SONY), a digital camera (E-420), and One-Touch Video Capture (VC500, Diamond Multimedia Inc.) and ImageJ (Version 1.43, National Institutes of Health).

3.2 Effects of cells and substrate surface properties on initial bacterial attachment in slow flowing systems

In this part, effects of cells and substrate surface properties on initial bacterial attachment in slow flowing systems were studied. The detailed procedure, including flow chamber system preparation, substrates modification by OTS-silane, bacterial suspension preparation, bacterial/substrates surface properties characterization, and bacterial attachment study in flow chamber system are described.

3.2.1 Chamber surface preparation and characterization

Square glass chambers with the internal cross section of 10 mm × 10 mm and the wall thickness of 0.9 mm were cut into 100 mm long pieces. For cleaning the cut chambers were immersed in the piranha solution (70/30 v/v 98% H_2SO_4/30% H_2O_2) at 80°C for 1 h and then rinsed with a copious amount of deionized (DI) water. The chambers were then dried with a stream of compressed nitrogen (N_2).

For OTS modification, the cleaned chambers were soaked in a solution of 0.168 wt % of OTS in HPLC-grade hexane for 30 min at room temperature. Afterwards, the chambers were sonicated in hexane for 5 min to remove the non-grafted OTS molecules, rinsed thoroughly with ethanol, and then dried with a stream of N_2.

Contact angles of water, methylene iodide, and ethylene glycol on the glass and OTS-modified chamber surfaces were measured to determine the surface energy of the substrate. They were measured by the sessile drop technique using a Rame-Hart contact angle goniometer under ambient conditions (1 atm, 24 ± 2°C). Both advancing and receding angles were measured on two randomly chosen spots on each of the triplicate samples. One-Touch Video Capture was used to record the drop shapes, and ImageJ was used to measure the contact angles.

3.2.2 Bacterial suspension preparation

PAO1 and *P. putida* were maintained as frozen stocks in TSB medium containing 15% glycerol. *E. coli* cells were maintained on TSB agar plates (30 g/L TSB and 12 g/L agar) at 4°C. A frozen tube of PAO1 was thawed at 34°C in an incubator-shaker for 15 min. The culture was then prepared in a two-step procedure. In the first step, 0.5 mL of the thawed culture were added to 10 mL growth medium (composition described in [54]) and grown overnight in the shaker at 280 rpm. In the second step, 5 mL of the grown culture were transferred into 45 mL of the same medium and grown for 18 h under the same temperature and shaking. The culture was finally ready to be diluted to the right cell concentration and used in the flow chamber experiment, as described later. The same procedure was used for *P. putida* except that the thawing/culturing temperature was changed to 28°C and that the growth medium was supplemented with 2.5 g/L peptone and 2.5 g/L yeast extract. For *E. coli*, the same medium containing peptone and yeast extract was used but the procedure was further modified: (1) 2 loops of the plate culture were used as the seeds for the first growth stage, (2) the growth duration was only 4 h in

both growth stages, and (3) the growth temperature was 37°C. The two-step procedure was adopted to eliminate the effect of different viability of stock cultures. The culture durations were determined from previous experiments (data not shown) to ensure that the culture used for the flow chamber studies were reproducibly at their mid to late exponential growth phases.

All the media used in this study were adjusted to pH 7.1 ± 0.1 and autoclaved at 121°C for 15 min before use. To keep the cell concentrations consistent, at about 7×10^6 cells/mL, in all the flow chamber experiments, the optical densities (OD) of the culture harvested at the end of the second growth stage were measured at 600 nm using a UV-vis spectrophotometer and the inoculation sizes adjusted. The adjustment was made according to the calibration curves, between the cell number concentration and OD_{600}, established for the 3 bacteria in previous experiments (data not shown). (The cell number concentrations were measured by plating the serially diluted cultures on TSB-agar plates and counting the developed colonies after incubation.) The low cell number concentrations, about 7×10^6 cells/mL, were chosen for easier counting of the attached cells on chamber wall.

3.2.3 Bacterial hydrophobicity evaluation

The cell partitioning to hexadecane–water interface was evaluated as an indicator of the cell surface hydrophobicity. 5 mL of the bacterial culture were centrifuged at 7000 rpm for 10 min. The cells were washed once by a pH 7.0 phosphate buffer, and then suspended in the buffer to make the OD_{400} 0.40 ± 0.01. 6.0 mL of hexadecane were then added and vortexed for 2 min. Next, the mixed suspension was kept stationary for 30 min

to allow phase separation. The OD of the bottom aqueous phase was measured. The percent decrease in OD, caused by the removal of cells to the water-hexadecane interface, was calculated.

Cell surface properties were also characterized by contact angle measurement as described in the following: A bacterial layer was prepared by collecting the cells on a Nylon filter. The bacterial suspension to be filtered was first diluted with DI water to an OD_{600} about 1.70. 20 mL of the bacterial suspension were filtered under the vacuum drawn by an aspirator. 20 mL of DI water were then added to the filter holder and filtered through to wash the bacterial layer. The aspirator was left on for 5 more min to dry the bacterial layer by the air drawn through the filter cake. The air flow rate was controlled at 400 mL/min using a flowmeter.

Contact angles of DI water, methylene iodide and ethylene glycol on the bacterial layer were measured using the Rame-Hart Goniometer. Drops of each probe liquid were placed on randomly chosen spots of the bacterial layer. Drop shapes were recorded and contact angles measured as described earlier. Use of the reproducible drying procedure (5 min of filtered air flow) was found very important. If the bacterial layer was not dried enough, the residual water on the surface would affect the contact angles obtained. If dried too much, the cell layer would wrinkle and even crack.

3.2.4 Cell surface zeta potential measurement

Zeta potentials of cells were measured in the same medium used in the chamber study by Malvern Zetasizer at 24°C with a fixed attenuator of 10. To avoid interferences from the nutrients and metabolites present in the broths, the cells were centrifuged and

washed once with DI water before being re-suspended in the chamber study medium. The suspension was then used for the zeta potential measurement.

3.2.5 Bacterial attachment study using the flow chamber system

The medium used for the flow chamber experiment was 100 mL of the 10 times diluted growth medium without glucose, peptone or yeast extract. The same medium was used for all 3 bacteria. The bacterial suspension (approximately 7×10^6 cells/mL) was continuously circulated at 20 mL/min between a reservoir flask and the square glass (or OTS modified glass) chamber, where the initial cell attachment on chamber surface was observed [54]. The attached cell numbers were counted hourly for the first 3 h using an optical microscope video system. Four to six screens imaged from different locations near the center of the chamber were counted, and the average number of attached cells per mm^2 was reported. After 3 h, the chamber was rinsed for about 10 min with a fresh saline solution at the same flow rate to remove the loosely attached cells. In each batch of experiment, two chambers were used for each bacterial species and chamber surface combination (e.g., PAO1-on-glass, *E. coli*-on-OTS, *etc.*) under investigation to ensure data reproducibility. In addition, each combination was evaluated with at least three experimental batches performed on different days. If the results were inconsistent, additional batches were carried out. The averages and standard deviations of these results are reported in this work.

3.3 Effects of shear on initial bacterial attachment in slow flowing systems

In this part of study, effects of shear on initial bacterial attachment in slow flowing systems were studied. The detailed procedure, including chamber, bacterial and particle suspension preparation, surface properties evaluation, bacterial cell and particle attachment study in flow chamber system are described.

3.3.1 Chamber preparation

Glass chambers with the internal cross section of 2 × 12 mm were cut into 150 mm long pieces. For cleaning, the cut chambers were sonicated in hexane and ethanol for 5 minutes each, then rinsed with a copious amount of deionized (DI) water, followed with sonication in DI water for 5 minutes, and finally dried with a stream of compressed nitrogen (N_2). The OTS modified surface (would be referred to the OTS surface in this manuscript) was prepared according to the previous method [19]. Briefly, after the cut chambers were thoroughly cleaned using a freshly prepared piranha solution (70/30 v/v 98% H_2SO_4/30% H_2O_2), they were immersed in a solution of 3 mM OTS in HPLC-grade hexane for 30 min at room temperature. Afterward, the chambers were sonicated in hexane and then rinsed with ethanol and DI water, separately, to remove the non-grafted OTS molecules.

3.3.2 Bacterial and particle suspensions preparation

The bacterial suspension preparation has been detailed elsewhere [19]. The cultured cells were diluted to ~ 6×10^6 cells/mL, measured using optical density (OD) at 600 nm with a UV-vis spectrophotometer and confirmed by direct cell counting. The low

cell concentrations were chosen for easier counting of the attached cells on chamber wall. The particles were diluted in DI water, also to a concentration of ~ 6×10^6 particles/mL.

3.3.3 Surface properties evaluation

Cell surface properties were characterized by contact angle measurements on bacterial layers prepared by a process established in our former study [19]. Briefly, a bacterial lawn was collected on a 0.22 mm Nylon filter by filtering ~ 50 mL of the bacterial suspension with ~ 1.7×10^9 cells/mL using a vacuum pump (vacuum at ~ 40 Torr). DI water (20 mL) was then added to the filter holder and filtered through to wash the bacterial layer. After all the liquid was filtered through, the vacuum pump was left on for 10 additional minutes to pull air through the lawn for further drying. Then, the filtered lawn was removed and left under the ambient condition for 5 minutes prior to contact angle measurements. Contact angles of DI water, methylene iodide, and ethylene glycol were measured on the lawn using the Rame-Hart Contact Angle Goniometer.

3.3.4 Bacterial cell and particle attachment

As described in our earlier study [19], the bacterial/particle suspension was circulated between the glass chamber and a reservoir flask at flow rates that gave the following corresponding shear stress on bottom chamber surface: 1, 2.5, 5, 15, 25, and 50 mN/m^2. The numbers of cells/particles attached on the bottom surface of the chamber were counted hourly for the first 3 h using an optical microscope video system. Four to six screens imaged from different locations near the center section of the chamber were counted, and the average number of attached cells per mm^2 was reported. After 3 h, the

chamber was rinsed for about 10 min with a fresh saline solution at the same flow rate to remove the loosely attached cells/particles. In each batch of experiment, two chambers were used for each bacterial species or particle type at each shear to ensure data reproducibility. In addition, every system, corresponding to a particular combination of species/particle, surface (glass or OTS), and shear studied, was evaluated with at least three experimental batches performed on different days. If the results were inconsistent, additional batches were carried out.

3.4 Corrosion of carbon steel and aluminum alloy in the presence of *Pseudomonas aeruginosa* and *Escherichia coli* biofilm

In this part of study, corrosion of carbon steel and aluminum alloy in the presence of *Pseudomonas aeruginosa* and *Escherichia coli* biofilm were studied. The detailed procedure, including metal coupons and bacterial suspension preparation, flow chamber design, bacterial attachment and biofilm formation and subsequent MIC behaviors monitoring, metal coupons post-run treatments and imaging, and corrosion rate determination are described.

3.4.1 Preparation of coupons

Carbon steel (CS) and aluminum (Al) were cut into 25 × 10 mm^2 pieces, and sonicated with acetone, ethanol, and deionized (DI) water for 2 min each, and then dried with compressed nitrogen (N_2). Al thin film was prepared by using physical vapor deposition method to deposit an Al thin film on a well-cleaned glass microscope slide. Glass microscope slides were cut into 18 × 9 mm^2 pieces. To clean the surfaces, glass

slides were immersed in the piranha solution (70/30 v/v 98% H_2SO_4/30% H_2O_2) at 80°C for 1 h. After decanting the solution, the slides were rinsed with a copious amount of DI water. The slides were then dried with a stream of compressed N_2. To coat the Al thin film on the surfaces of slides, the physical vapor deposition method was utilized. An Al thin film with a thickness of ~50 - 100 nm was coated onto the well-cleaned microscope glass slides.

3.4.2 Design of flow chambers

Rectangular glass chambers with an internal cross section of 2 × 12 mm^2 and a wall thickness of 1.2 mm were cut into 150 mm long pieces, followed by the cleaning procedure of sonicating in acetone, ethanol, and DI water for 2 min each. After a glass slide with the Al thin film, a glass slide, an Al coupon, another glass slide, and a CS coupon were placed into the chamber in that order, the chambers were connected with a glass tubing (inside and outside diameters of ~ 6 mm and 8 mm, respectively) by melting/blowing and fusing the glass parts together as shown in Figure 3.1(a). After that, the chambers were immersed into 75% ethanol for about 18 h to make sure the inside surface and all the coupons and slides were sterilized. For each set of run, at least four chambers were used; two served as control chambers, where no cells were presented, and the other two were allowed to have a particular strain of bacteria to attach for three.

3.4.3 Preparation of bacterial suspension

The bacterial suspension preparation has been detailed elsewhere [19]. All the media used in this study were adjusted to pH 7.1 ± 0.1 and autoclaved at 121°C for 15

min before use. The cultured cells were diluted to ~7×10^6 cells/mL, measured using optical density (OD) at 600 nm with a UV-vis spectrophotometer and confirmed by direct cell counting. The low cell concentrations were chosen for easier counting of the attached cells on chamber wall. The particles were diluted in DI water, also to a concentration of ~7×10^6 particles/mL.

3.4.4 Monitoring bacterial attachment and biofilm formation and subsequent MIC behaviors

As shown in Figure 3.1(b), the medium used for the experiments was 100 mL of the 10 times diluted growth medium without glucose, peptone or yeast extract. The same medium was used for both bacteria. During the bacterial attachment study, the bacterial suspension was continuously circulated at 20 mL/min between a reservoir flask and the chamber, where the initial cell attachment on glass microscope slides and the Al-thin film deposited glass slides was observed for up to three hours. The attached cell numbers were counted hourly using an optical microscope video system. Four to six screens imaged from different locations near the center of the chamber were counted, and the average number of attached cells per mm^2 was reported.

After 3 h, the bacterial suspension was removed (dashed lined section of Figure 3.1(b)), and an enriched cell free medium was flowing over, one pass only, attached cells with flow rate at 0.4 mL/min. Normally, two chambers containing coupons with bacterial cells attached to, and two control chambers where only coupons presented without cells, were connected in parallel to the flowing medium. The coupons in the control chambers were used to assess the effects of the enriched medium on the corrosion behaviors of the

metal coupons. The medium provided the necessary nutrients for the attached cells to grow into a biofilm.

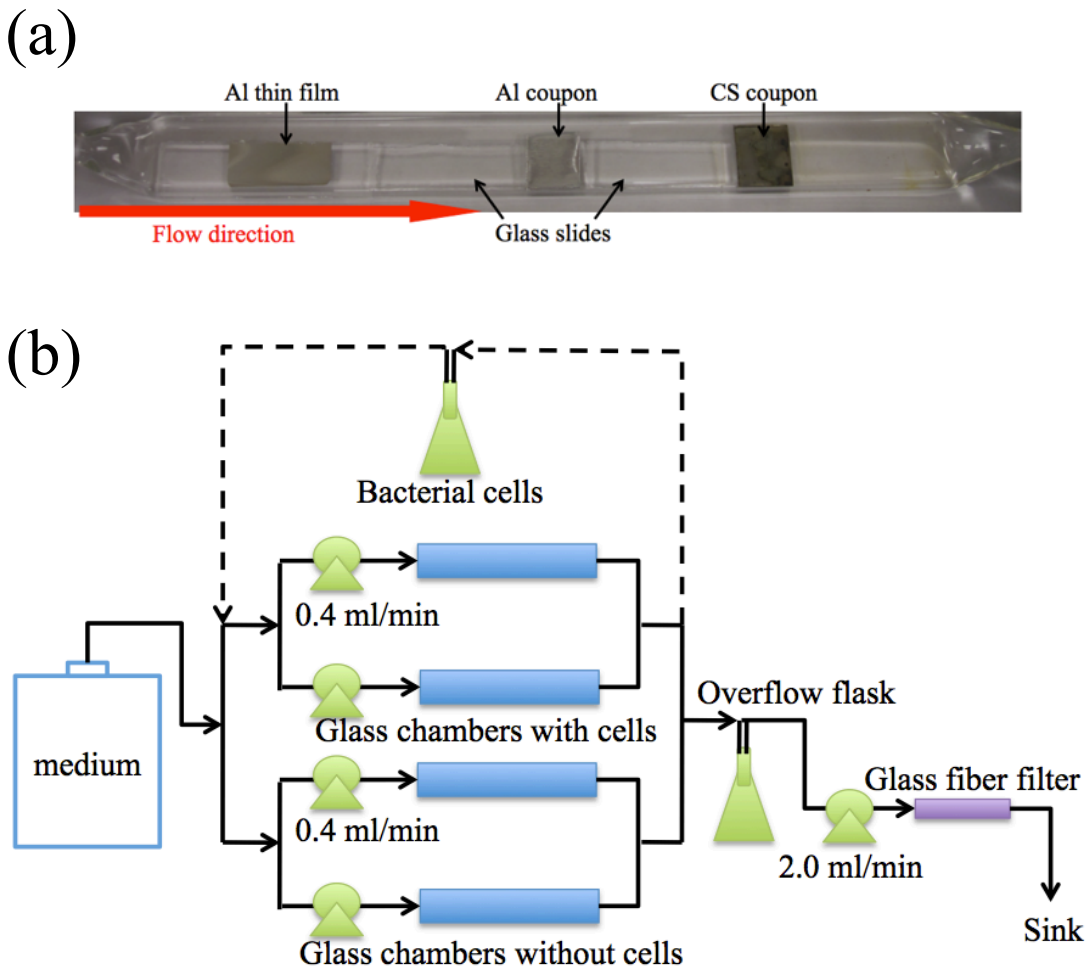

Figure 3.1 (a). The picture of flow chamber is shown, together with Al thin film, Al coupon, and CS coupon, from left to right, inside. (b). The schematic of flow chamber system is shown. The dash line connection is for initial bacterial attachment. After 3 h, this connection is removed, and the chambers are connected to the flow through system (solid lines) for bacterial biofilm formation and metal corrosion study.

As the biofilm was being formed, the thickness of biofilm on metal coupon was measured using the microscope every 24 h. To measure the biofilm thickness, the microscope was first focused on the bottom layer of the cells, and then focused on the top layer of the cells, and distance the objective travelled in between the two focuses was assumed to be the thickness of the biofilm.

3.4.5 Post-run treatments and imaging

The chambers, one control and one with cells, were taken off the system at day 7 and another set at day 14, to determine the corrosion rate and examine the corrosion features. Before the coupons were removed from the chamber, a fresh saline solution followed with DI water, was flowing through the chamber, at the flow rate of 0.4 mL/min, to wash away the loosely attached biofilm for 30 min each. After the coupons were removed from the chambers, biofilm morphology and structure was evaluated by confocal microscopy after stain the biofilm with Live/Dead fluorescent stains. Afterwards, the standard weight loss cleaning procedure (ASTM D2688-05) was followed. A soft-brush was used to brush the coupons surfaces to remove the firmly attached biofilm and corrosion products. Brushing was continued until the weight of the coupons is consistent, and then the coupons were dried with N_2. Finally, surface roughness of coupon was examined using IFM.

3.4.6 Corrosion rate determination

All the aluminum and CS coupons were weighted, using an analytical balance (accuracy of 0.1 mg), before the coupons were inserted into the chambers and after the

post cleaning procedure as described above. The size and thickness of the coupons were also measured using a caliper before and after. The corrosion rate was calculated based on the weight loss of the coupons, according to the ASTM standard D2688-05. The exact expression for the corrosion rate in the unit of mils per year is:

$$\text{Corrosion rate (mils per year, mpy)} = 22.3\ W / (d\ a\ t) \qquad (12)$$

where: W is weight loss in mg, d is density of the metal in g/cm^3, a is the exposed surface area of the coupon in in^2, and t is the time of the evaluation period in days.

3.5 Corrosion behaviors of carbon steel C1010 and stainless steel 304 in the presence of iron oxidizing bacteria *Acidithiobacillus ferrooxidans*

In this part of study, corrosion behaviors of carbon steel C1010 and stainless steel 304 in the presence of iron oxidizing bacteria *Acidithiobacillus ferrooxidans* were examined. The detailed procedure, including preparation of coupons and bacterial suspension, corrosion test and monitoring biofilm formation, post-run treatment and imaging, and corrosion rate determination are described.

3.5.1 Preparation of coupons

Carbon steel (CS) and Stainless steel (SS) were cut into 25 × 10 mm^2 pieces, and followed with cleaning procedure of sonication with acetone, ethanol, and deionized (DI) water for 2 min each, and then dried with compressed nitrogen (N_2).

3.5.2 Preparation of bacterial suspension

A. ferrooxidans was cultured in 9K medium [86]: $(NH_4)_2SO_4$ 3.0 g/L; KCl 0.10 g/L; K_2HPO_4 0.50 g/L; $MgSO_4 \cdot 7H_2O$ 0.50 g/L; $Ca(NO_3)_2$ 0.01 g/L; $FeSO_4 \cdot 7H_2O$ 14.74% (w/v); and 10 N H_2SO_4 1 mL/L. The pH of 9K medium was ~ 2, and sterilized by filtration through 0.22 μm filter system. Cell culture was maintained at 26 °C in the shaker at 150 rpm under aerobic condition and transferred every 7 d. The culture for experimental use was prepared freshly: 5 mL cell culture was added into 45 mL 9K medium, incubated at 26 °C in the shaker at 150 rpm for 24 h. To ensure the reproducibility of this study, cell concentration was determined by direct cell counting and controlled at the concentration of ~ 2×10^7 cells/mL.

3.5.3 Bacterial attachment study using the flow chamber system

The medium used for the flow chamber experiment was 100 mL of the 10 times diluted basal salts solution (9K medium without H_2SO_4 and $FeSO_4 \cdot 7H_2O$). The bacterial suspension (approximately 5×10^6 cells/mL) was continuously circulated at 0.4 mL/min between a reservoir flask and a rectangular glass chamber with a piece of CS coupon, glass slide, and OTS modified glass slide. The attached cell numbers were counted after 1 h and 3 h. Before counting the cells, the chamber was rinsed for about 10 min with a fresh saline solution at the same flow rate to remove the loosely attached cells. Afterwards, attached cells were stained with Live/Dead fluorescent stains, and counted by florescent optical microscope. In each batch of experiment, two chambers were used for each bacterial species and chamber surface combination under investigation to ensure data reproducibility. In addition, each combination was evaluated with at least three

experimental batches performed on different days. If the results were inconsistent, additional batches were carried out. The averages and standard deviations of these results are reported in this work.

3.5.4 Corrosion test and monitoring biofilm formation

For the corrosion test, metal coupon was placed into 20 mL vial, and 10 mL of pH ~2 H_2SO_4/water (as control system), cell medium (without cells, pH ~2), and bacterial suspension (pH ~2) were added into the vial, respectively. The vials were kept on a shaker with 150 rpm under room temperature (~ 20 °C). *A. ferrooxidans* cells can attach and propagate on the metal surface then develop into biofilm. Biofilm morphology and structure were evaluated by confocal microscopy after stain the biofilm with Live/Dead fluorescent stains after 1 d and 7 d. To study if the biofilm was attach onto metal coupon firmly, 10× diluted basal salts solution (9K medium without $FeSO_4 \cdot 7H_2O$) was utilized to gently rinse the metal coupon surface for ~ 30 s, and the attached cells were examined by confocal microscopy as well.

3.5.5 Post-run treatments and imaging

Corrosion behaviors were examined after 1 d, 3 d, 7 d, 14 d, 21 d, and 28 d, respectively. Each condition had at least 8 duplicates. After the coupons were removed from the vials, the standard weight loss cleaning procedure (ASTM D2688-05) was followed. A soft-brush was used to brush the coupons surfaces to remove biofilm and corrosion products. Brushing was continued until the weight of the coupons was

consistent, and then the coupons were dried with N_2. Finally, surface roughness of coupon was examined using IFM.

3.5.6 Corrosion rate determination

All the CS and SS coupons were weighted, using an analytical balance (accuracy of 0.1 mg), before experiment and after the post cleaning procedure as described above. The size and thickness of the coupons were also measured using a caliper before and after. The corrosion rate was calculated based on the weight loss of the coupons, according to the ASTM standard D2688-05.

3.6 Corrosion evaluations of aluminum alloy (Al 2024) in the presence of *Trichoderma reesei* and *Aspergillus niger*

In this part of study, corrosion evaluations of aluminum 2024 in the presence of *Trichoderma reesei* and *Aspergillus niger* were studied. The detailed procedure, including preparation of coupons and fungal suspension, fungal attachment study using static vessel system, and corrosion rate determination are described.

3.6.1 Preparation of coupons

Aluminum 2024 was cut into 50 × 10 mm^2 pieces, and followed with cleaning procedure of sonication with acetone, ethanol, and deionized (DI) water for 2 min each, and then dried with compressed nitrogen (N_2).

3.6.2 Preparation of fungal suspension

Both *T. reesei* and *A. niger* were maintained on potato dextrose agar plates. Before use, Both *T. reesei* and *A. niger* were transferred and cultured in 100 mL 24 g/L potato dextrose broth at room temperature (21 ± 2°C) in the shaker at 150 rpm for 72 h.

3.6.3 Fungal attachment study using static vessel system

To maintain the systems pH at a certain level, pH controllable static vessel system (Figure 3.2) was design and utilized. In the vessel, pH was monitored and controlled by a pH probe, which was connected to a digital pH adjustment box. The box was used to real time monitoring and adjusting the pH associated with two pumps linked to acid and base solution respectively.

The medium used in vessel system for fungal growth was as follows: $(NH_4)_2SO_4$ 1.4g/L, KH_2PO_4 2 g/L, $MgSO_4 \cdot 7H_2O$ 0.3 g/L, $CaCl_2 \cdot 2H_2O$ 0.4 g/L, $CO(NH_2)_2$ 0.3 g/L, proteose peptone 1 g/L, Tween-80 (1.08g/mL) 0.2 g/L, Trace elements 1 mL/L, and glucose 10 g/L. After fungal suspension transferred into the vessel, glucose concentration was monitored by dinitrosalicylic acid (DNS) assay. To ensure there were enough nutrients for cells to grow, glucose concentration was maintained at ~ 8 g/L.

The attached cells were evaluated after 7 and 14 days. Before counting the cells, the Al coupon was rinsed with DI water for 30 seconds to remove loosely attached fungal cells. Afterwards, attached cells were stained with Live/Dead fluorescent stains, and counted by florescent optical microscope. To ensure results reproducibility, four Al coupons were collected in each batch of experiment.

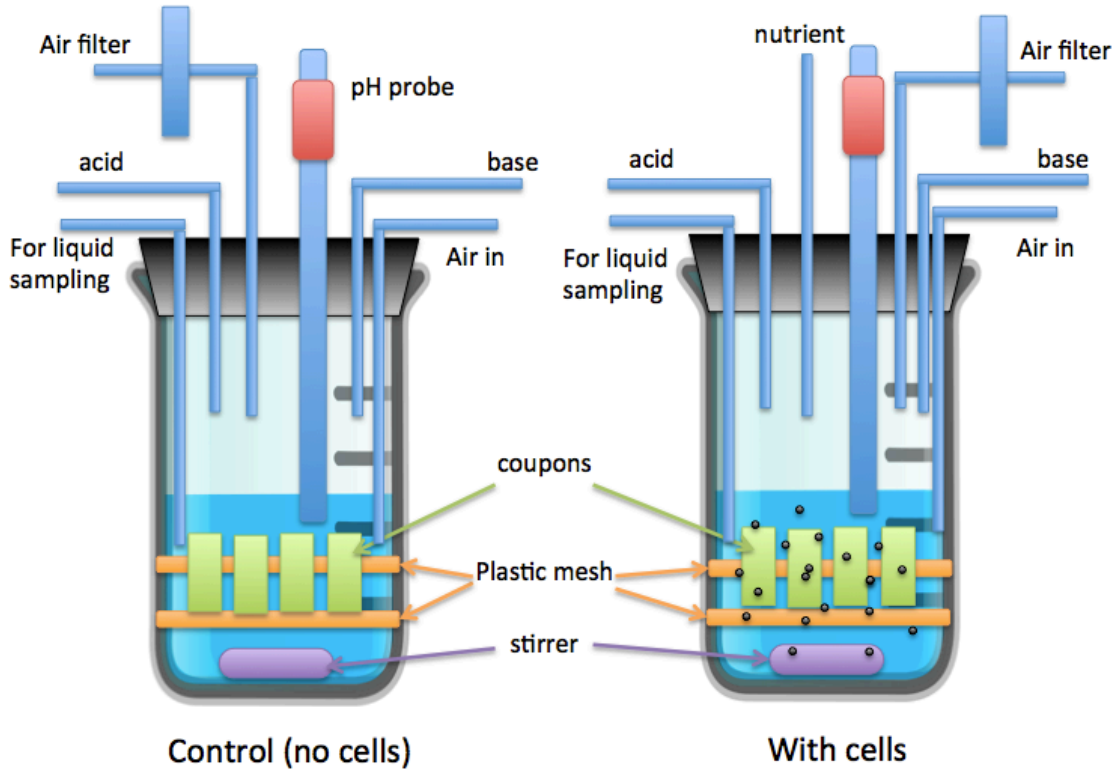

Figure 3.2 The schematic of static vessel system is shown.

3.6.4 Corrosion rate determination

All the Al coupons were weighted, using an analytical balance (accuracy of 0.1 mg), before experiment and after the post cleaning procedure as described above. The thicknesses of the coupons were measured using a caliper to determine the exposed area. The corrosion rate was calculated based on the weight loss of the coupons, according to the ASTM standard D2688-05.

CHAPTER IV

RESULTS AND DISCUSSION

This chapter summaries all the results and discussion of this work. Is consists of five main sections. Section 4.1 describes the effects of cell and substrate surface properties on initial bacterial attachment in slow flowing systems. Section 4.2 explains the effects of shear on initial bacterial attachment in slow flowing systems. Section 4.3 demonstrates corrosion of carbon steel and aluminum alloy in the presence of *Pseudomonas aeruginosa* and *Escherichia coli* biofilm. Section 4.4 discusses corrosion behaviors of carbon steel C1010 and stainless steel 304 in the presence of iron oxidizing bacteria *Acidithiobacillus ferrooxidans*. Section 4.5 details Corrosion evaluations of aluminum alloy Al 2024 in the presence of *Trichoderma reesei* and *Aspergillus niger*.

4.1 Effects of cell and substrate surface properties on initial bacterial attachment in slow flowing systems

This part demonstrates the results and discussion about effects of cell and substrate surface properties on initial bacterial attachment in slow flowing systems. The subsections include initial attachment on glass and OTS modified chamber, hydrophobic partitioning of bacterial cells to hexadecane, surface properties evaluations, interpretation of the attachment data by the extended DLVO theory, and summary.

4.1.1 Introduction

Biofilm, the highly structured microbial communities, has negative impacts on various biomedical, environmental and maritime systems and/or operations [7]. Biofilm forms sequentially, with the transport of microorganisms to surfaces and the initial microbial attachment being among the first steps. An effective way to manage biofilm formation is to inhibit/reduce the initial microbial or bacterial attachment [87, 88]. The process of initial bacterial attachment is complicated; it can be affected by various physicochemical properties of both bacterial cells and the substrate surfaces [7]. During the past decades, the surface hydrophobicity/hydrophilicity, charge, and polarity of cells and the substrate surfaces have been considered as the primary factors. Theories, based on the adhesion/deposition of colloidal particles, especially the classical Derjaguin-Landau-Verwey-Overbeek (DLVO) [8, 9] and extended DLVO (XDLVO) models [10, 11], have been utilized to interpret initial microbial attachment.

In the classical DLVO theory [43, 89], two main interactions, the attractive Lifshitz-van der Waals (LW) and the repulsive electrostatic double layer (EL)

interactions are included. To account for the potential hydrogen bonds, which are common when a bacterial cell interacts with an oxidized or hydrophilic surface, van Oss et al. [10, 11] added the short-range Lewis acid-base (AB) interactions in the XDLVO theory. The DLVO theory and, especially, the XDLVO theory have been found to adequately interpret the initial microbial adhesion in many studies [7, 44-46], on substrates of different hydrophobicity and in both static and flow systems. There have also been studies where the experimental results could not be directly explained by the XDLVO theory [47, 90-94]. For these studies, some specific events or properties, such as the formation of polymeric bridges, significant deviation of the bacterial cells from a round shape to an elongated shape, or cell surface heterogeneity, have been believed to be the causes. When such causes have been properly accounted for, e.g., by adjusting the cell radius for a non-spherical cell, and/or alternating the overall cell surface properties from the contribution of the cell surface structures/exopolymers, the XDLVO theory has been generally valid for interpreting bacterial attachment.

In addition to bacterial cell properties, the medium conditions also affect the overall interaction energy and its components. The surface energy and its components, as well as the zeta potential of the medium are all varying with the individual nutrient concentrations, pH and ionic strength of the medium. These medium conditions also affect the properties of cells. Substances in the medium, especially the dissolved organic matter, could adsorb to the cell and/or substrate surfaces, thus affecting the initial attachment behaviors [45, 47, 49].

In order to gain a better understanding on the initial bacterial attachment under the natural water environment, the conditions closely mimicking natural water should be

employed. In this part of study, dilute media with low bacterial concentrations (close to those found in natural aquatic environment) slowly flowing through a chamber were utilized. The flow rate was estimated to be similar to those of the slow flowing streams or waves brushing against stationary structures. Three common bacteria, *Pseudomonas aeruginosa*, *Escherichia coli*, and *Pseudomonas putida*, were employed. To evaluate if hydrophobic interactions play a role in initial bacterial attachment, experiments were carried out to determine the attachments of these bacteria to glass chambers modified with a hydrophobic organosilane, octadecyltrichlorosilane (OTS), and the results were compared to those obtained with the unmodified hydrophilic glass chambers. In addition to the attachment study made in the flow chambers, various properties of bacteria and substrates were measured so that the cell-substrate interaction energies at different separation distances can be calculated according to the XDLVO theory. In general, the interaction energy predicted by the DLVO or XDLVO theory shows two energy minima, a primary minimum at a very small d (e.g. d = 0 nm if such contact can be made) where the irreversible cell attachment would result, and a secondary minimum at a larger d (5 - 100 nm, [45, 90]) where the approaching cells would attach reversibly. In most cases, an energy barrier exists going from the secondary minimum to the primary minimum. The extents of initial bacterial attachment obtained in this study were correlated with the interaction energies computed, in particular the secondary minima and the energy barriers. The objectives were to verify the applicability of XDLVO theory to the bacteria-substrate combinations investigated in this study and, more importantly, to gain insights into the potential attachment mechanisms of bacteria in natural water environments.

4.1.2 Initial attachment on glass chambers

As shown in Figure 4.1, the number of attached cells increased with time and the increasing trends were similar for the three bacteria under study. PAO1 attachment number increased from 750 cells/mm^2 after 1 h to 1380 cells/mm^2 after 3 h; *P. putida* attachment number increased from 990 cells/mm^2 after 1 h to 1920 cells/mm^2 after 3 h; and *E. coli* attachment number increased from 1500 cells/mm^2 after 1 h to 3240 cells/mm^2 after 3 h. The saline rinse reduced the attachment by ~ 20%. Among the three species, *E. coli* gave the highest attachment and PAO1 the lowest, especially after 2 h and after 3 h. Also, a greater increase in attachment with attachment time was observed for *E. coli* as compared to the other two strains.

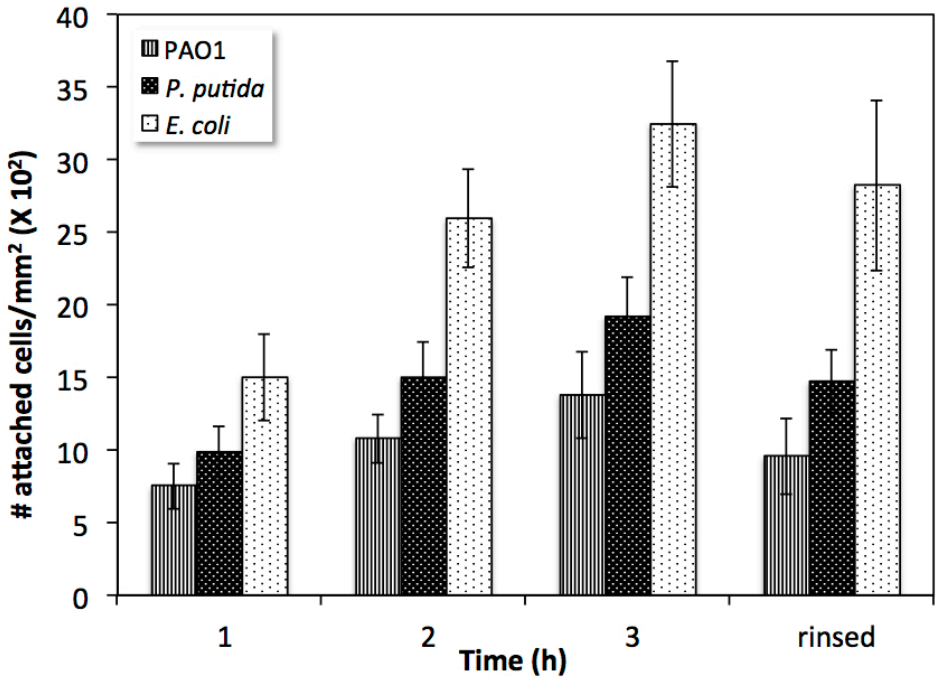

Figure 4.1 The initial attachments of three bacterial strains: PAO1, *P. putida* and *E. coli*, on the bottom surface of the glass chamber are shown. The error bars shown for each is the standard deviation value obtained for at least eight data points.

4.1.3 Initial attachment on OTS modified glass chambers

While the trends of increasing attachment as attachment time increased were still seen for the three bacterial strains, the completely opposite order of attachment with regard to the bacterial strains was observed in the hydrophobic OTS modified chambers. More specifically, the highest attachment (from 6210 after 1 h to 10930 cells/mm^2 after 3 h) of PAO1 and the lowest (from 660 after 1 h to 1950 cells/mm^2 after 3 h) of E. coli (Figure 4.2a) were resulted. *P. putida* also showed an increased in bacterial attachment on the OTS surface (from 3100 after 1 h to 5270 cells/mm2 after 3 h) as compared to that on the glass surface. When the relative attachment caused by the OTS modification was computed (i.e., the ratio of the attachment number on the OTS surface to that on the glass surface), the value was 8-10 for PAO1, about 3 for *P. putida* and 0.5-0.7 for *E. coli* (Figure 4.2b). These values indicated that for PAO1, the cell attachment on the OTS surface was about 8-10 times more than that on the glass surface, while for *E. coli*, the OTS modification reduced the cell attachment by 30%-50%. The chamber wall hydrophobicity clearly had very different effects on different bacteria, which had different cell surface properties as described in the following sections.

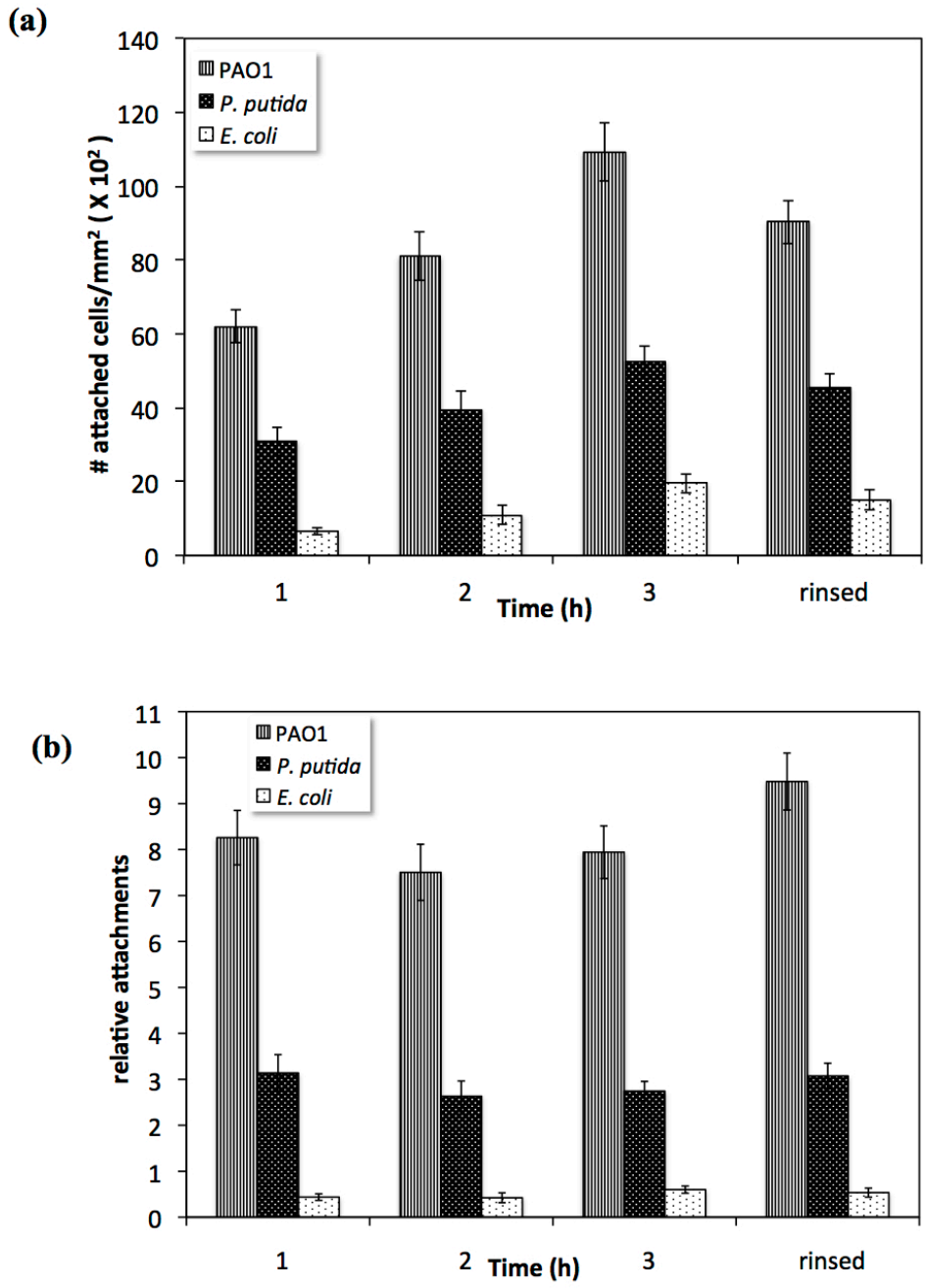

Figure 4.2 (a). The initial attachment of three bacterial strains: PAO1, *P. putida* and *E. coli*, on the bottom surface of the OTS modified glass chamber are shown. (b). To provide a better comparison of the hydrophobic effects of chamber wall, relative attachments of the initial attachment of PAO1, *P. putida* and *E. coli*, on the bottom surface of the OTS modified chambers to those on the un-modified glass surfaces are shown. The error bars shown for each is the standard deviation value obtained for at least eight data points.

4.1.4 Hydrophobic partitioning of bacterial cells to hexadecane

In an attempt to understand the cell attachment behaviors, partitioning of the three bacteria to the water-hexadecane interface was examined. Hexadecane (CH3(CH2)14CH3) is a hydrophobic organic solvent that has similar chemical structure and properties to the hydrocarbon tail of OTS (CH3(CH2)17Si≡Cl3). The percentage removal of cells from the original aqueous suspension to the water-hexadecane interface was determined to be 36.7 ± 4.5 % (highest) for PAO1 (in 4 repeated batches of experiments), 10.8 ± 2.8 % for *P. putida* (in 4 repeated batches), and 5.1 ± 4.7 % (lowest) for *E. coli* (in 5 repeated batches). The results suggested that PAO1 was the most hydrophobic among the three and *E. coli* was the least. The attachments of bacterial cells on the glass surfaces with and without OTS modification are plotted against the extents of cell partitioning to the water-hexadecane interface in Figure 4.3. Since PAO1 cells were relatively more hydrophobic than the other two strains, the highest attachment (6210 cells per mm^2 shown in Figure 4.2) on the hydrophobic OTS surface but the lowest (750 cells per mm^2 shown in Figure 4.1) on the glass surface were observed. On the other hand, *E. coli* cells were relatively hydrophilic, leading to the least attachment (660 cells per mm^2 shown in Figure 4.2) on the OTS surface but the most attachment (1500 cells per mm^2) on the glass surface. Qualitatively, it is clear that the cell attachment on the hydrophobic OTS modified substrate increased with increasing cell surface hydrophobicity while the attachment trend was opposite on the hydrophilic glass substrate.

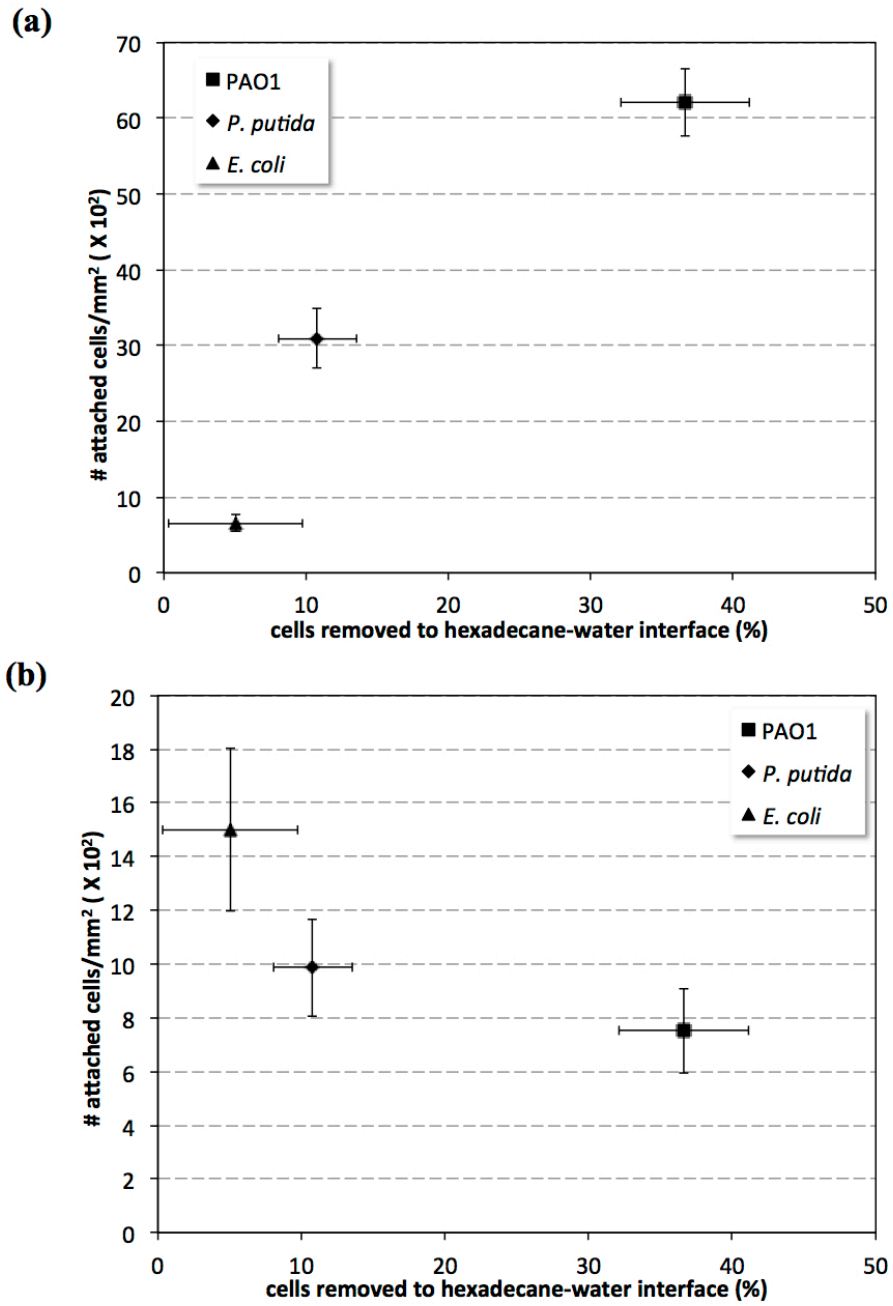

Figure 4.3 (a). The attachment of the three bacterial strains on the OTS surface is shown to have a positive linear relationship with the hydrophobic partitioning of cells to the water-hexadecane interface. (b). The attachment of the three bacterial strains on the glass surface decreases with the increase of the hydrophobic partitioning of cells to the water-hexadecane interface. The error bars shown for each is the standard deviation value obtained for at least eight data points.

4.1.5 Surface properties evaluations

The surface properties of bacterial cells and the chamber surfaces were characterized in more detail by contact angle measurements. For bacterial cells, the zeta potentials were also measured. In addition, the features, shape and size of the bacterial cells were assessed via AFM scans. Table 4.1 summarizes the obtained values and Figure 4.4 shows the representative topographic scans of the bacterial cells. The contact angles of water and ethylene glycol on the dried cell layers showed the same trend as the afore-mentioned water-hexadecane partitioning results, i.e., highest for PAO1 and lowest for *E. coli*. The results confirmed that PAO1 was the most hydrophobic and *E. coli* the least.

Table 4.1 The contact angles of water, methylene iodine, and ethylene glycol on the three bacterial lawns, zeta potential of PAO1, *P. putida* and *E. coli* in the medium suspension used for attachment study, and the equivalent bacterial size estimated from the AFM topographic scans are presented. Also presented are the surface energy and its components (LW and AB) of each surface of interests.

Bacteria/substrate	PAO1	*P. putida*	*E. coli*	glass	OTS
$\theta_W(°)$	23.6 ± 3.2	20.5 ± 0.9	17.6 ± 1.1	37.6 ± 6.0	96.2 ± 0.9
$\theta_{MI}(°)$	52.8 ± 4.8	66.7 ± 2.3	46.3 ± 1.5	33.0 ± 2.3	52.9 ± 1.3
$\theta_{EG}(°)$	25.5 ± 3.8	21.8 ± 0.6	17.6 ± 0.9	17.2 ± 1.6	72.0 ± 3.7
ζ(mV)	-32	-30	-36	-22[a]	-62[b]
R(μm)	0.39	0.52	0.70	-	-
γ	41.6	44.2	44.0	48.0	32.6
γ^{LW}	32.7	24.7	36.3	42.9	32.6
γ^{AB}	8.9	19.5	7.7	5.0	0.0
γ^+	0.3	1.4	0.2	0.2	0.0
γ^-	63.5	66.7	64.4	41.9	1.7

Note: The units of all g values are mJ/m^2.
a: value of zeta potential was taken from Ref. [95].
b: value of zeta potential was taken from Ref. [96].

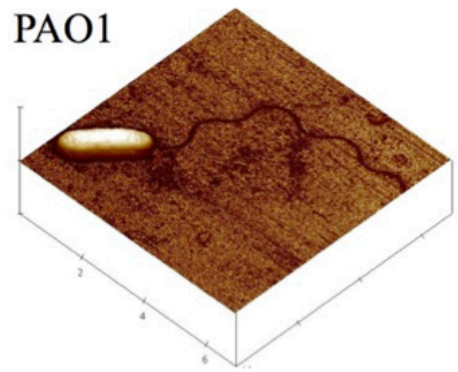

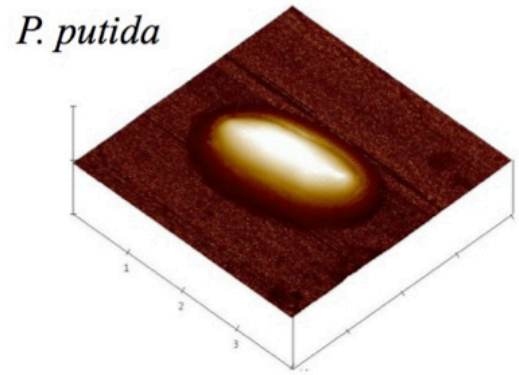

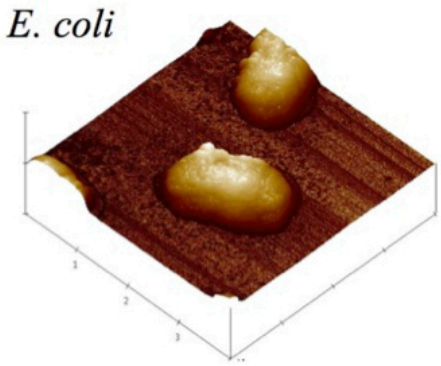

	L (μm)	*W* (μm)	*H* (μm)
PAO1	2.27±0.02	0.99±0.03	0.38±0.03
P. putida	2.19±0.02	0.93±0.02	0.59±0.06
E. coli	1.93±0.06	1.24±0.05	0.97±0.07

Figure 4.4 Atomic force microscopic (AFM) topography scans of the three bacterial strains. The length (L), width (W) and height (H) from the scans were utilized to estimate the equivalent radius, *R*, (by assuming the cell is spherical in shape) of the bacterial cell. The scan size for *E. coli* and *P. putida* is 3 x 3 mm2, and it is for 6 x 6 mm^2 PAO1 so the length of the flagella can be shown. The standard deviation value for each data point reported in the table is the results of at least ten cross-sectional measurements.

The estimated surface energy, based on the contact angle values of three probe liquids, and its (LW and AB) components for the three bacteria and the two types of surfaces are also given in Table 4.1. Estimation of these values followed the approach used by van Oss and co-workers [10, 11]. For the bacterial cells, *P. putida* and *E. coli* had similar surface energies (~ 44 mJ/m^2), while PAO1 had a slightly smaller surface energy (~ 40 mJ/m^2). When the components of the surface energy were compared, *E. coli* had the highest γ^{LW}, the Lifshitz-van der Waals interaction component, while the γ^{LW} values for PAO1 and *P. putida* were similar. However, E. coli had the lowest γ^{AB} (~ 8 mJ/m^2), the contribution from AB interactions. γ^{AB} was ~ 12 mJ/m^2 for PAO1 and ~ 20 mJ/m^2 for *P. putida*. Furthermore, all three bacteria had much higher γ^- than γ^+, indicating they were more negatively charged, which was confirmed by the zeta potential measurements.

For the chambers, the glass surface had a higher total surface energy as well as its γ^{LW} and γ^{AB} components than the OTS modified surface did. The OTS surface was apolar and its surface energy came from γ^{LW} only. After being grafted to the oxidized glass surface, the OTS molecules were expected to self-assemble into a monolayer with their terminal –CH3 group exposed on the outside surface.

4.1.6 Interpretation of the attachment data by the extended DLVO theory

With the surface energy components of cells and substrates determined, the values of $\Delta G_{d_0}^{LW}$ and $\Delta G_{d_0}^{AB}$, summarized in Table 4.2, could be obtained from equations (1) and (2), respectively, and the interaction energy between a single cell and the flat substrate plate separated at a certain distance (d) can be calculated using equations (4)-(6). The total interaction energies for various bacteria-substrate combinations are shown in Figure

4.5. (For less crowded presentation in the figure, the profiles for the PAO1–glass and *P. putida*–glass combinations are not shown. They were similar to that for the E. coli–glass combination.) For all three bacteria on the OTS-modified substrate, the interaction energy showed both primary and secondary minima, separated by an energy barrier. The values of interaction energy and d at the secondary minimum (i.e. ΔG_{sm}^{XDLVO} and d_{sm}) and the energy barrier are also given in Table 4.3. Compared to the primary minimum, the secondary minimum was much shallower, with its value ranging from -1.6 kT for *E. coli* to -0.4 kT for *P. putida*, occurred at a distance (d_{sm}) of 34 – 37 nm away from the substrate surface. The calculated energy barriers were significant, approximately 600, 800 and 1250 kT for PAO1, *P. putida*, and *E. coli*, respectively. On the other hand, for all three bacteria-glass combinations, the energy barriers would be in 16,000 to 30,000 kT occurred at a much smaller d (0.02 – 0.05 nm), so only the secondary minimum (at d_{sm} of 25 – 29 nm) was apparent in the interaction energy profiles at a separation distance of d_0 and greater [47]. The values of ΔG_{sm}^{XDLVO} were negative, indicating cell attachment at their corresponding d_{sm} were favorable; however, for the cells to attach at primary minima, the significant energy barriers between the primary and secondary minima had to be overcome.

Table 4.2 The values of $\Delta G_{d_0}^{LW}$ and $\Delta G_{d_0}^{AB}$ estimated using equations (2) and (3), respectively, are reported.

Bacteria	Substrate	$\Delta G_{d_0}^{LW}$	$\Delta G_{d_0}^{AB}$
PAO1	glass	-3.95	39.96
	OTS	-1.68	-15.89
P. putida	glass	-1.15	40.01
	OTS	-0.49	-7.45
E. coli	glass	-5.11	40.70
	OTS	-2.17	-16.08

Note: The units of all ΔG_{d_0} values are mJ/m^2.

Table 4.3 The secondary minima of interaction energies and the energy barriers between the secondary and primary minima of the three bacterial strains interacting with the two types of surfaces are summarized. For the three bacteria-glass combinations, primary minima were not found within the separation distance range ($d > d_0$).

Bacteria/substrate	energy barrier (kT)	ΔG_{sm}^{XDLVO} (kT)	d_{sm} (nm)
PAO1_glass	16525*	-2.0	26.0
PAO1_OTS	600	-0.7	34.1
*P. putida*_glass	23524*	-1.1	29.2
*P. putida*_OTS	800	-0.4	37.1
*E. coli*_glass	29150*	-4.7	25.4
*E. coli*_OTS	1250	-1.6	33.5

Note: ΔG_{sm}^{XDLVO} : the interaction energy at the secondary minimum.

d_{sm}: the separation distance between the cell and the substrate at the secondary minimum.
*: primary minima were not found within the separation distance range ($d > d_0$), these are the "would have been" values obtained when d continued to decrease to a value of 0.02 – 0.05 nm.

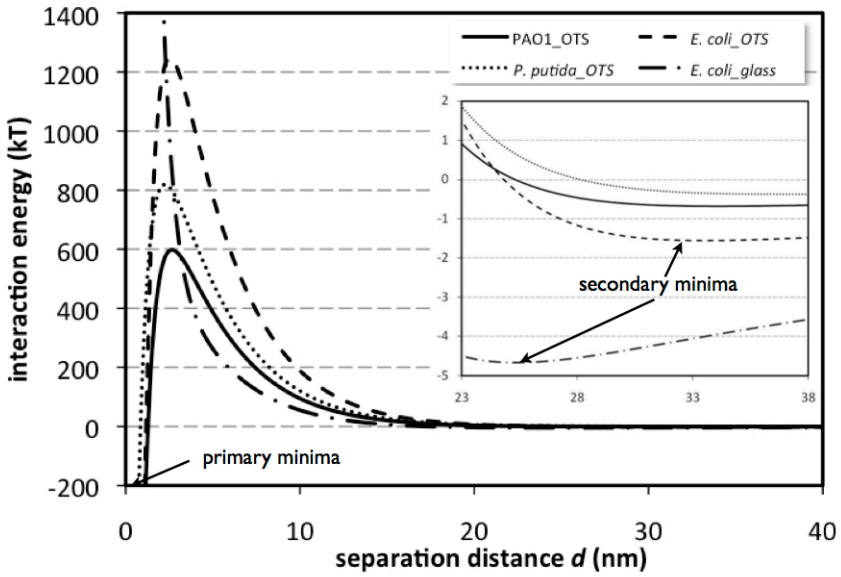

Figure 4.5 The total interaction energies, estimated by the XDLVO theory, vs. separation distance are shown for the PAO1-OTS combination (solid line), the *P. putida*-OTS combination (dotted line), the *E. coli*-OTS combination (dashed line) and the *E. coli*-glass combination (dashed-dotted line). While for the case of the OTS surface, the energy barriers for all three bacterial strains are resulted. The primary minima for the PAO1-OTS, *P. putida*-OTS, and *E. coli*-OTS combinations are not shown in the profiles, their values are -5116, -2774, and -8704 kT, respectively. For the case of the glass surface, only the secondary minima, at a distance of $d \geq d_0$, exist based on the calculation. The primary minima for all three bacteria-glass combinations would occur at $d < 0.015$ nm, which is outside the separation range ($d > d_0 = 0.158$ nm) we plotted.

The first attempt was to correlate the initial bacterial attachments with the attachment tendency at the secondary minima only; thus, all the attachment data (3 bacteria × 2 substrates) are plotted in Figure 4.6 against ΔG_{sm}^{XDLVO}. The correlation was conceptually reasonable for the attachments of all three bacteria on the hydrophilic glass surface and that of *E. coli* on the hydrophobic OTS surface: the attachments appeared to decrease as ΔG_{sm}^{XDLVO} became less negative (although the low attachments for bacteria-substrate combinations with very shallow ΔG_{sm}^{XDLVO}, about -2 kT to -1 kT, did not differ significantly). The correlation clearly failed for the attachments of PAO1 and *P. putida* on the OTS substrate: these attachments were much higher although the ΔG_{sm}^{XDLVO} values were larger (i.e., less negative) than -1 kT.

The above findings suggested the following: (1) The attachments of all 3 bacteria on glass and the attachment of *E. coli* on the OTS-modified substrate were likely at or near the secondary-minimum distances (d_{sm}). (2) While some PAO1 and *P. putida* cells might have attached on the OTS substrate at or near d_{sm}, much more could overcome the energy barriers to become attached corresponding to the primary minima, resulting in the much higher total attachments observed in these bacteria-substrate combinations. (3) The extent of primary-minimum attachment appeared to correlate with the energy barrier, with the highest attachment, e.g. 6210 cells/mm^2 attached after 1 h as shown in Figure 4.6 for the lowest energy barrier (600 kT) in the PAO1–OTS combination, and the second highest attachment, e.g. 3100 cells/mm^2 attached after 1 h for the second lowest energy barrier (800 kT) in the *P. putida*–OTS combination. The primary-minimum attachment diminished when the energy barrier was even higher, i.e., 1250 kT for the *E. coli*–OTS

combination and all the bacteria-glass combinations (where the energy barrier would be in tens of thousands of kT occurred at a d of ~ 0.02 to 0.05 nm ($< d_0$).

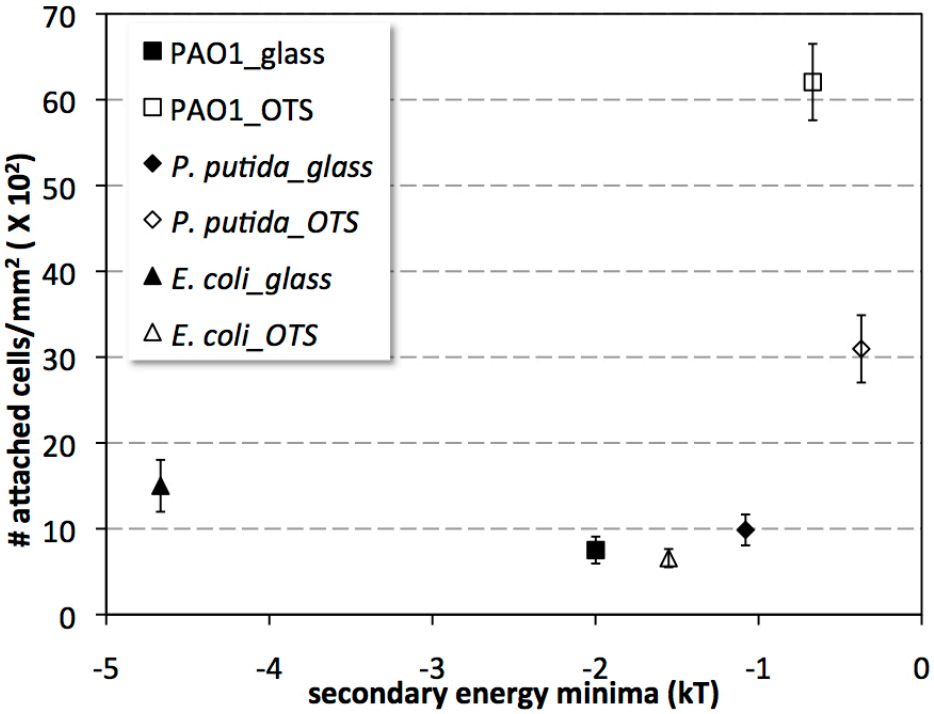

Figure 4.6 The attachment number is plotted against the secondary energy minima of the three bacterial strains on the two types of surfaces. The error bars for each attachment number are the standard deviation value obtained for at least eight data points.

While the experimental data clearly suggested the occurrence of primary-minimum attachments of PAO1 and *P. putida* cells on the OTS modified substrate, the calculated energy barriers for these bacteria-substrate combinations were significant, i.e., 600 kT for PAO1 and 800 kT for *P. putida*. In order to overcome such high energy barriers, other effects/properties needed to be taken into account. It has been reported that an energy barrier up to 100 kT might be overcome [44], although the authors gave no explanations for the responsible mechanisms. On the other hand, Azeredo et al. [47] studied the contribution of exopolymers in bacterial adhesion. They noticed that an energy barrier of ~ 300 kT was overcome to allow strong adhesion by a high exopolymer producing mutant of *Sphingomonas paucimobilis*. This was attributed to the formation of "polymeric bridges" due to the presence of extensive exopolymers on the cell surface. Other cell surface features (e.g. fimbriae, fibrils, flagellae) could also affect bacterial attachment or provide a means for the cell to overcome the energy barrier. These surface features have much smaller radii than those of the cell, and smaller radii correspond to lower interaction energies as shown in equations (4)-(6). Accordingly, the magnitude of energy barrier decreases linearly with decreasing contact radius. From our AFM scans (Figure 4.4), PAO1 cells were found to contain long flagella (with a radius of $\leq$ 15 nm and a length of 5 – 6 μm) and *P. putida* cells appeared to be covered by a layer of exopolymers. Both PAO1 and *P. putida* cells were also less rounded than *E. coli* cells. Early studies [44, 90] have indicated that the deviation of cell shape from a perfect sphere could allow the cells to attach with the end of smaller radius, thus encountering a lower energy barrier [93].

For PAO1 cells, the most elongated shape and the existence of flagella might lead to much lower "actual" energy barriers due to the reduced contact radii. For example, if the flagella, with a radius of ≤ 15 nm (a radius as small as < 5 nm has been reported [90]), were responsible for bringing the cells closer to the substrate for the primary-minimum attachment, the energy barrier would be ≤ 23 kT, significantly less difficult to overcome. *P. putida* cells could also lower the energy barrier due to their surface exopolymers and the elongated shape.

Future studies with more microorganisms and more substrate surfaces are warranted to evaluate the following two alternative hypotheses: (1) the extent of primary-minimum attachment correlates well simply with the energy barrier calculated using sphere-equivalent cell radius, and (2) the extent of primary-minimum attachment correlates better with the energy barrier calculated using the smaller/smallest radius of contact possible, by considering the cell shape and surface appendage. Concluding on these hypotheses and generating a broader data base through the systematic studies will be very valuable to the advancement of our capability of predicting initial cell attachment on different substrates.

4.1.7 Summary

In this section of study, we investigated the initial bacterial attachment of PAO1, *P. putida*, and *E. coli* on a hydrophilic glass surface and a hydrophobic OTS surface. On the glass surface, PAO1 was experimentally observed to have the lowest attachment, while *E. coli* to have the highest attachment. This result was roughly correlated to the secondary minima, estimated using the XDLVO theory, of the three bacterial strains-

glass combinations. However, on the OTS surface, the opposite was noticed, which could only be interpreted by using the energy barrier between the secondary and primary minima of the interaction energy profile predicted by the XDLVO theory. The ability of the PAO1 cells to overcome the energy barrier was likely attributed to the flagella present on their surfaces and the distortion of the cells from spheres. Cell distortion and a potential layer of exopolymers on the *P. pituda* cell could be the reason why some *P. pituda* cells also overcame their energy barrier to attach at their primary minima. However, for *E. coli*, the cells retained their rounded shape and the energy barrier was too high to be overcome. Also, because the depth of secondary minimum of *E. coli* on the OTS surface was smaller (i.e. less negative) than that of *E. coli* on the glass surface, a lower attachment of *E. coli* cells on the OTS surface was observed. The XDLVO theory thus provided insights into the potential cell attachment mechanisms for bacterial attachment under slow flow and low nutrient conditions mimicking the natural water environments.

4.2 Effects of shear on initial bacterial attachment in slow flowing systems

This part presents the results and discussion about effects of shear on initial bacterial attachment in slow flowing systems. The subsections include initial attachments, shear effects on initial attachment, gravitational settlement on initial attachment, convective diffusion on initial attachment, shear force and adhesion force, interaction energy and attractive force based on the XDLVO theory, and summary.

4.2.1 Introduction

Bacterial biofilm has many negative impacts especially in biomedical (e.g. infectious diseases, oral diseases) and environmental (e.g. ship fouling, microbiologically induced corrosion) fields [97-99]. Many bacteria prefer to adhere to a surface or to cell aggregates and form biofilm, which may provide a protective environment and a symbiotic community for more efficient use of available nutrients. Biofilm development relies on the ability of certain bacterial cells to initiate the attachment and grow into biofilm [100-102]. In order to prevent/reduce bacterial biofilm formation, it is important to evaluate the factors that affect the initial bacterial attachment. In addition to the surface and medium properties that determine the thermodynamic interactions between bacterial cells and a surface, the shear associated with flow conditions could be one of the most important factors affecting initial bacterial attachment [12].

The objectives of this part of work were to verify whether or not the XDLVO theory is applicable in predicting the critical shear stress for preventing attachment, hence the shear dependent behaviors of initial bacterial attachment and to gain a better understanding on initial bacterial attachment at low shears (< 100 mN/m^2). One Gram-

positive bacterium *S. epidermidis* and three Gram-negative bacteria: *P. aeruginosa*, *P. putida*, and *E. coli* were observed for their attachment behaviors onto two types of surfaces, glass and octadecyltrichlorosilane (OTS) modified glass. Most of the results obtained, especially the critical shear stress for preventing attachment, were explainable by the attractive force predicted by the XDLVO theory. For the results that could not be directly interpreted by the XDLVO analysis, the extracellular polymeric substances (EPS) and cell surface features (e.g. flagella) were found to contribute to the attachment behaviors.

4.2.2 Initial attachments

The attachment of positively charged amidine latex PS particles on both glass and OTS surfaces at a shear stress of 15 mN/m^2 is shown in Figure 4.7(a). The number of attached particles increased with time, and then decreased slightly by the rinse of fresh saline at the end of the 3rd hour attachment experiment. More particles (up to 30%) attached to glass than to the OTS surface. For glass, the attachment increased from 1770 particles/mm^2 after 1 h to 2990 particles/mm^2 (~ 70% higher) after 3 h, and then decreased (by ~ 10%) to 2730 particles/mm^2 after rinsing. The attachment number on the OTS surface increased from 1330 particles/mm^2 after 1 h to 2330 particles/mm^2 after 3 h, and decreased to 2030 particles/mm^2 after rinsing.

In term of attachment time, bacteria were found to behave similarly as PS particles, i.e. increase with attachment time and decrease after rinsing, to a particular surface type. As a result, only the attachment at the end of the 1st hour is presented and discussed for the rest of this paper. The 1st hour attachment numbers of the four bacteria

studied at a shear stress of 15 mN/m^2 are shown in Figure 4.7(b). On glass, PAO1 had the highest attachment number (1290 cells/mm^2), followed by *E. coli* (770 cells/mm^2) and *P. putida* (580 cells/mm^2); *S. epidermidis* had the lowest attachment (290 cells/mm^2). On the OTS surface, PAO1 again exhibited the highest attachment (12360 cells/mm^2), followed by *P. putida* (1160 cells/mm^2) and *E. coli* (540 cells/mm^2); *S. epidermidis* again showed the lowest attachment (420 cells/mm^2).

Besides the effect of different species, these data indicated that substrate surface wettability also played an important role in bacterial attachment. As compared to hydrophilic glass, the hydrophobic OTS surface caused dramatic increases in attachment of PAO1 (900% higher) and *P. putida* (100% higher). The attachment on the OTS surface was also ~ 50% higher for the Gram-positive *S. epidermidis*. Only *E. coli* attached less, by ~ 30%, on the OTS surface than on the glass surface.

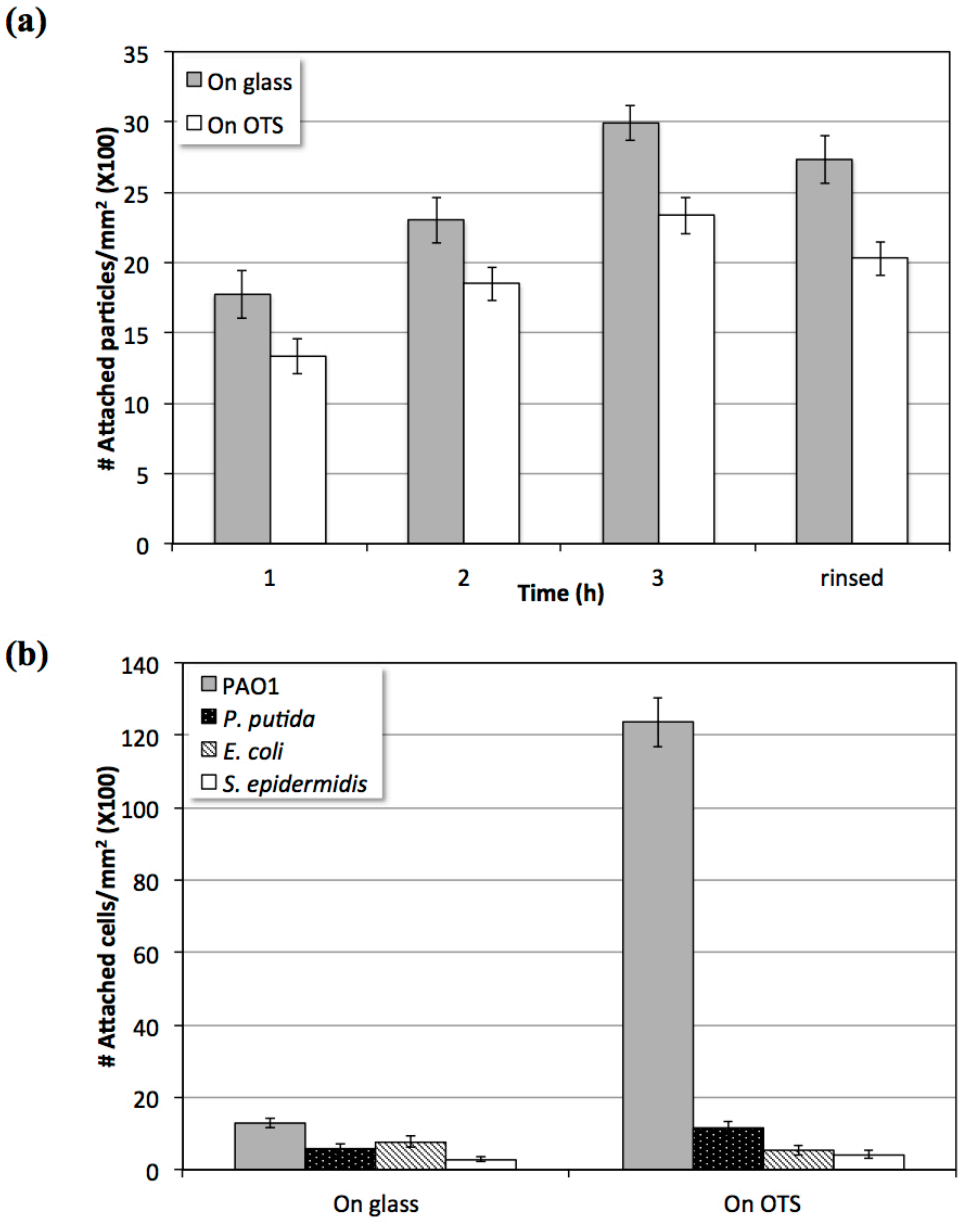

Figure 4.7 (a). The attachments of positively charged amidine latex (AL) PS particles on the surfaces of glass and OTS modified glass at the shear stress of 15 mN/m^2 are shown. (b). The attachments at the end of the 1st hour (we defined this as the initial attachments) of four bacterial strains: PAO1, *P. putida*, *E. coli*, and *S. epidermidis*, on the surfaces of glass and OTS at a shear stress of 15 mN/m^2 are shown. The errors shown for each data point is the standard deviation obtained from at least four sets of measurements.

4.2.3 Shear effects on initial attachment

Towards the two types of surfaces, particles and bacterial cells showed some differences in initial attachment at the shear stress of 15 mN/m^2. The 1st hour attachment numbers of the two types of PS particles (positively charged amidine latex, PS-AL, and negatively charged carboxylate modified latex, PS-CML) on glass and OTS surfaces under shear stresses of 0.1, 1, 2.5, 5, 15, 50, 150, 175, and 200 mN/m^2 are shown in Figure 4.8. On glass, the attachment of PS-AL continued increasing from 610 to 3600 particles/mm^2 as the shear stress increased from 0.1 to 175 mN/m^2. It plateaued (~ 3500 particles/mm^2) after about 150 mN/m^2 and then dropped sharply to 1710 particles/mm^2 at the highest shear stress (200 mN/m^2) tested. On the OTS surface, the attachment of PS-AL increased slightly at the very low shear range, from 2160 to 2450 particles/mm^2 as the shear stress increased from 0.1 to 2.5 mN/m^2. The attachment then started to decrease, more rapidly initially, with increasing shear stress. Very similar results were observed for PS-CML.

Shear effects on the 1st hour bacterial attachment on glass is shown in Figure 4.9(a). The attachment was investigated at the shear stresses of 1, 2.5, 5, 15, 25, and 50 mN/m^2. For *S. epidermidis*, the attachment on glass did not differ (p value = 0.56) from 1 to 5 mN/m^2 and then decreased as the shear stress increased from 5 to 50 mN/m^2. For *E. coli*, a continuous gradual decreasing trend for the attachment was noticed. For PAO1, the attachment numbers were basically the same (p value = 0.46) from 1 to 5 mN/m^2, and then decreased as the shear stress increased from 5 to 50 mN/m^2. The *P. putida*-glass combination showed a gradual decrease in attachment numbers as the shear stress

increased from 1 to 25 mN/m^2, and then remained almost constant when the shear stress increased from 25 to 50 mN/m^2.

On the OTS surface (Figure 4.9(b)), the trend of *S. epidermidis* attachment was similar to that on glass but with a lower critical shear stress (i.e. ~ 2.5 mN/m^2). The attachment of *E. coli* showed a similar trend as that on glass. For PAO1, an almost linear but rapid decreasing trend (from ~ 16,500 cells/mm^2 at 1 mN/m^2 to ~ 6,500 cells/mm^2 at 50 mN/m^2) was observed. For *P. putida*, the attachment numbers were statistically similar (p value = 0.25) from 1 to 25 mN/m^2, and then slightly increased from 25 to 50 mN/m^2. Over the entire shear stress range studied, fewer *E. coli* cells, slightly more *S. epidermidis* and *P. putida* cells, and significantly more PAO1 cells were found to attach on the OTS surface than on glass at the same shear stress.

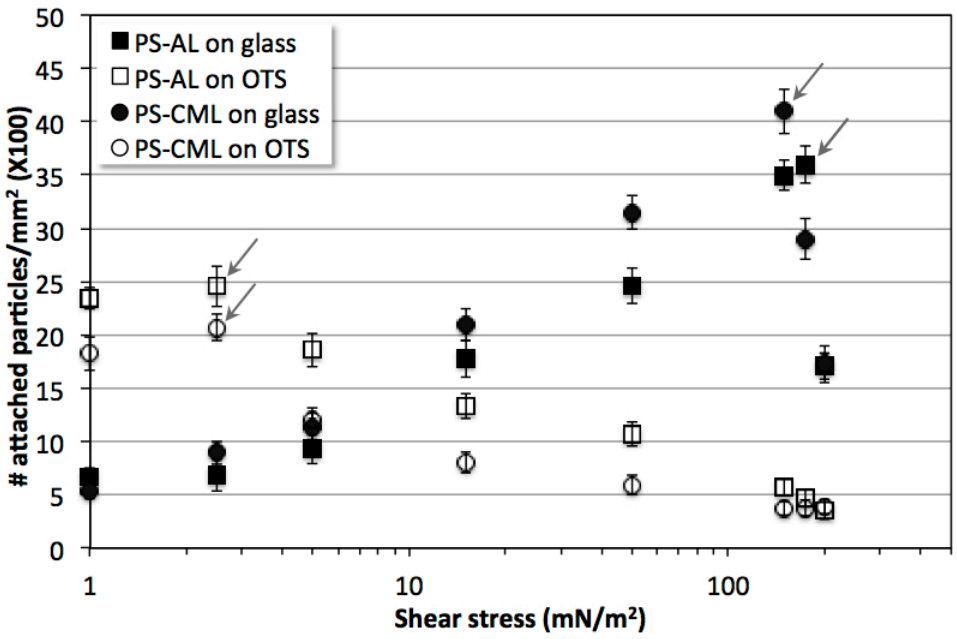

Figure 4.8 The initial attachments of particles on glass and the OTS surface under different shear stresses (0.1, 1, 2.5, 5, 15, 50, 150, 175, and 200 mN/m^2) for both positively charged and negatively charged (carboxylate modified latex, CML) PS particles are summarized. The errors shown for each data point is the standard deviation obtained from at least four sets of measurements. The arrows pointed out the maximum attachments occurred at the critical shear stresses.

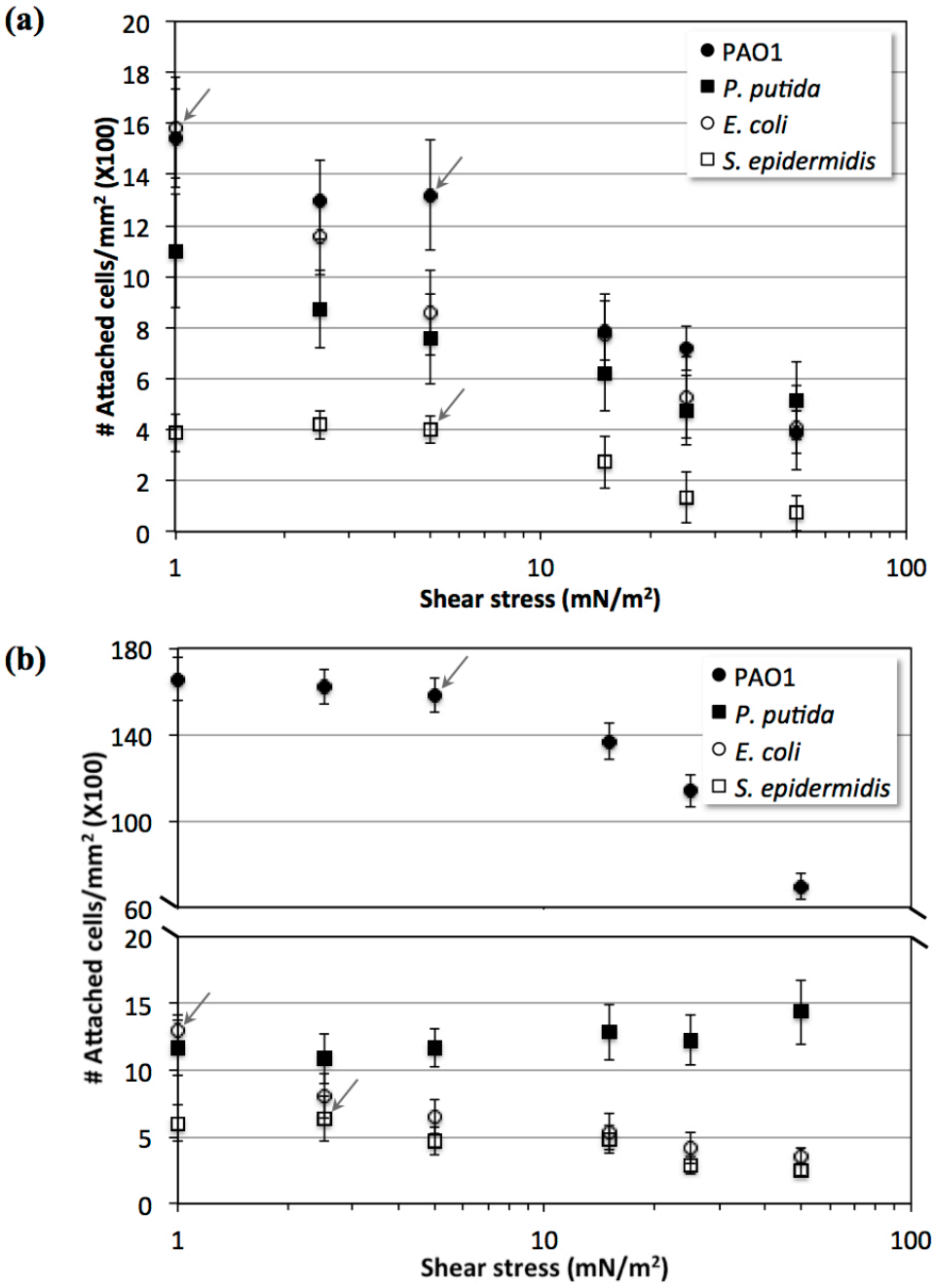

Figure 4.9 (a). The initial attachments of four bacterial strains: PAO1, *P. putida*, *E. coli*, and *S. epidermidis*, on glass under different shear stresses (1, 2.5, 5, 15, 25, and 50 mN/m^2) are shown. (b). The initial attachments of PAO1, *P. putida*, *E. coli*, and *S. epidermidis* on the OTS surfaces under different shear stresses (1, 2.5, 5, 15, 25, 50 mN/m^2) are summarized. The errors shown for each data point is the standard deviation obtained from at least four sets of measurements. The arrows pointed out the maximum attachments occurred at the critical shear stresses.

4.2.4 Gravitational settlement on initial attachment

The gravitational cell settlement in the flow chambers under different shears could be a factor for the observed attachment results. To examine this effect, the ratios of attached cells/particles to settled cells/particles were estimated and compared. The maximum settlement of cells/particles per unit time onto the bottom surface of a flow chamber with a laminar flow is QC, where Q and C are the volumetric flow rate and the concentration of cells/particles in the flow, respectively. On the per unit area basis, the settlement number (N) simply becomes $v_s\ C$, with v_s being the settlement velocity and having an expression of $v_s = \frac{2R^2(\rho_c - \rho)g}{9\mu}$, where R is the radius of the cell/particle, ρ_c is the density of cell/particle, ρ is the fluid density, g is the gravitational acceleration, and μ is the viscosity of the fluid. Therefore, the settlement number is independent of flow rate, and for specific cell concentration and fluid properties, N depends only on R^2 if the cells/particles have similar densities.

Table 4.4 summarizes the values of N for the PS particle and bacterial species used in this study. As shown in Table 4.4, the PS particle had the highest settlement (~ 4400 particles/h-mm^2), followed by *S. epidermidis* (~ 2300 cells/h-mm^2), and *E. coli*, PAO1 and *P. putida* had similar settlements (~1700, ~1600 and ~1400 cells/h-mm^2, respectively). The ratios (R_as) of the attached cells (experimentally observed) to the settled cells (estimated) at the shear stress of 15 mN/m^2 are also given in Table 4.4. Normally, the value of R_a was expected to be smaller than 1, which was observed for most cases presented in this study, except PAO1 on the OTS surface. Also, the ratios for most cases were 0.3 to 0.5. The low attachment/settlement ratio (< 0.3) of *S. epidermidis* could be the result of how the cells interacted with the surface. *S. epidermidis* cells are

diplococcic. It has been reported that they rotate more tempestuously [103] under flow as compared with other cocci or rod-shape cells. The constant rotation prior to attaching to the surface could lead to a lower attachment.

Table 4.4 The cells/particles gravitational settlement numbers N, ratios of cells/particles attachment to settlement (Ra) on both types of surface, the secondary energy minima (ΔG_{sm}^{XDLVO}) and the maximum attractive forces (F_{MAX}^{XDLVO}) estimated using the XDLVO theory, and critical shear stresses (σc)/forces ($F_{c-shear}$) determined experimentally are summarized.

		PS-AL	PS-CML	*S. epidermidis*	*E. coli*	PAO1	*P. putida*
N (cells/h-mm^2)		4400	4400	2300	1700	1600	1400
R_a (at 15 mN/m^2)	Glass	0.40	0.47	0.12	0.45	0.49	0.44
	OTS	0.30	0.18	0.21	0.32	8.54	0.91
ΔG_{sm}^{XDLVO} (kT)	Glass	-3.86	-3.55	-0.80	-0.12	-0.50	-0.31
	OTS	-0.102	-0.100	-0.025	-0.004	-0.016	-0.010
F_{MAX}^{XDLVO} (fN)	Glass	413	350	98 (77)[a]	8.5	42 (0.9)[a]	25
	OTS	7.2	6.8	2.2 (1.7)[a]	0.2	1.0 (0.02)[a]	0.6
σ_c (mN/m^2)	Glass	~ 175	~150	~5	<1	~5	-
	OTS	~2.5	~2.5	~2.5	<1	~5	-
$F_{c-shear}$ (fN)	Glass	~438	~375	~29 (23)[a]	<5	~9	-
	OTS	~6	~6	~15 (12)[a]	<5	~9	-

Note: [a]: The F_{MAX}^{XDLVO} estimated by cell shapes and surface features.

For PAO1 on OTS, R_a was about 8.5 at the shear stress of 15 mN/m^2. This high value could be attributed to the assistance of flagella during the attachment process [104-106]. Our PAO1 cell has a long flagellum with a length of ~ 10 mm and a radius of ~ 5 nm. Flagella, which consist of flagellin proteins that favor hydrophobic interactions [107], could initiate contact and immobilize the cell onto the hydrophobic OTS surface [108, 109]. It was estimated that about 1.0×10^5 cells/h-mm^2 passed through the chamber at the height of less than 10 mm away from the bottom surface of the chamber. This number was about 80 times higher than the settlement number. A R_a value of ~ 8.5 would mean that, at the shear stress of 15 mN/m^2, about one-tenth of these cells could become attached on the OTS surface via the flagellum-initiated mechanism.

If attachment was solely governed by the gravitational settlement, the attachment would remain more or less the same at different flow rates (i.e. shears) because the settling number was independent of flow rate, as mentioned earlier ($N = v_s C$); however, our experimental data for both PS particles and the four bacterial species clearly showed the attachment was shear dependent. Therefore, other factors, such as convective diffusion and interaction forces, could play more important roles and lead to the shear dependent attachment behaviors.

4.2.5 Convective diffusion on initial attachment

In addition to gravitational settlement, transporting particles/cells to the surface by flow, e.g. convective diffusion, could influence attachment. Attachment of bacteria can be expressed by initial deposition rate j_0 (cm^{-2}s^{-1}) [44], which is the number of attached bacterial cells per unit area, $n(t)$, over time, t, at a t closes to zero, i.e.:

$$j_0 = \frac{n(t)}{t}\Big|_{t=0} \tag{13}$$

The upper limit for bacterial deposition is an approximate solution of the convective – diffusion equation by assuming perfect sink conditions at the substrate surface. The expression, using the Von Smoluchowski-Levich (SL) approach, is [110]:

$$j_0^* = \frac{D_\infty c}{0.89r}\left[\frac{2}{9}\cdot\frac{bPe}{x}\right]^{1/3} \tag{14}$$

where D_∞ is the diffusion coefficient of the particles (taken as 4.25×10^{-13} m^2/s for 1 μm diameter bacteria in water at 20 °C [111]), c is the bacterial suspension concentration, r is the bacterial radius, x is the longitudinal distance from the flow chamber entrance, b is the half depth of the chamber and Pe is the Péclet number ($Pe = \frac{3Qr^3}{4wb^3D_\infty}$), where Q is the flow rate in the chamber and w is the width of the chamber. The ratio between j_0 and j_0^* is the deposition efficiency α.

Boks et al. [55] utilized the correlation between deposition efficiency and shear rate to determine the critical shear rates. Based on their approach, the critical shear rates to prevent adhesion (σ_{prev}) can be deduced from:

$$\alpha = \alpha_0 \cdot \exp\left\{-\frac{\sigma}{\sigma_{prev}}\right\} \tag{15}$$

in where α_0 is the extrapolated deposition efficiency in the absence of shear. Consequently, the critical shear stress (τ_{prev}) can be determined by

$$\tau_{prev} = \eta \cdot \sigma_{prev}$$

where η is the absolute viscosity of the bacterial suspension (e.g. 1×10^{-3} Pa s in our case).

According to the approach, the critical shear stress and critical shear forces of each bacterium-substrate combination can be calculated, which are listed in Table 4.5. Figure 4.10 shows an example of the approach based on Boks et al. using the PS-AL data on both glass and OTS surfaces. The values from our approach, directly using the transition point from the increased attachment to decreased attachment as shear stress increase, are also presented in Table 4.5 for comparison.

Compared with the estimated critical shear stress from both methods, the estimated values based on the approach by Boks et al. are all higher than our estimated values. For all four bacterial species, the critical shear obtained using the method of Boks et al. are very similar, even for *P. putida*, where the attachment was found to increase slightly with the increase of shear. Therefore, the deposition efficiency approach utilized by Bok et al. might not be suitable for estimating the critical shear stress in our case. Some modification to the approach might need to be made to better reflect the experimental results obtained in our study.

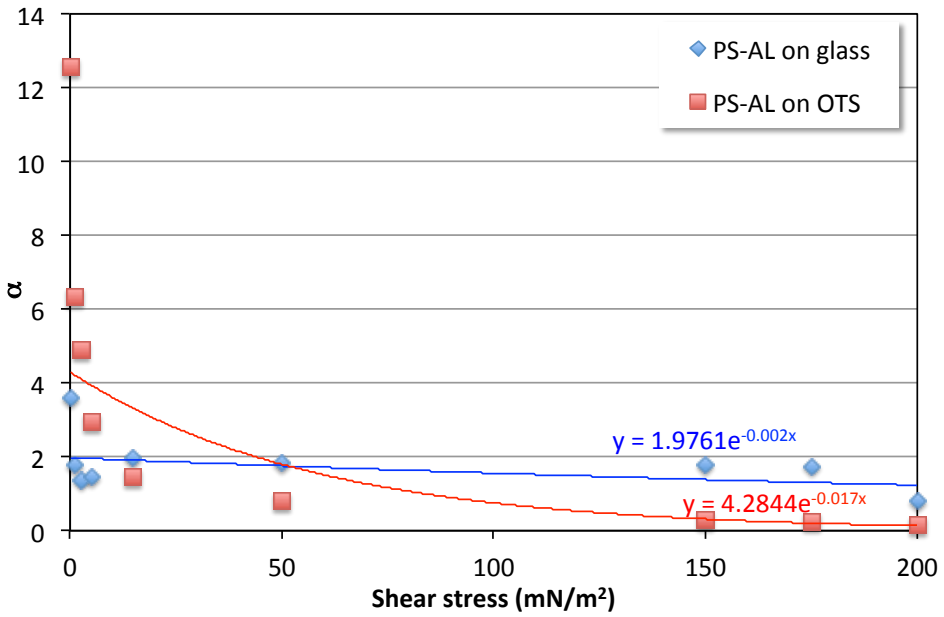

Figure 4.10 The PS-AL deposition efficiency, on both glass and OTS surfaces, as a function of shear stress. The trendlines are added based on the deposition efficiency approach.

Table 4.5 Critical shear stress/force by deposition efficiency and experimental results.

		Deposition efficiency analysis		Experimental	
		Critical shear stress (mN/m^2)	Critical shear force (fN)	Critical shear stress (mN/m^2)	Critical shear force (fN)
PS-AL	Glass	500	1250	~175	~438
	OTS	59	148	~2.5	~6
PS-CML	Glass	333	833	~150	~375
	OTS	63	158	~2.5	~6
S. epidermidis	Glass	16	94	~5	~29
	OTS	24	141	~2.5	~15
E. coli	Glass	21	105	<1	<5
	OTS	22	110	<1	<5
PAO1	Glass	20	37	~5	~9
	OTS	24	44	~5	~9
P. putida	Glass	27	237	-	-
	OTS	53	464	-	-

4.2.6 Shear force and adhesion force

The potential particle/bacterial adhesion process is illustrated in Figure 4.11. When the particle/cell is arriving to the substrate surface, the particle/cell might slide on the substrate for a certain distance before completely attaching onto the surface. During the process, the forces acting on the particle/cell control the attachment behavior.

In our case, the main forces the particle/cell is experiencing include the shear force acting parallel to the substrate and the attractive force acting perpendicular to the substrate. Under a steady state condition, the free body diagram of the forces on the particle/cell is presented in Figure 4.12. If the shear force exerted by the fluid flow on the particle/cell overcomes the maximum resistance force (i.e. $c\ (F_{MAX}^{XDLVO} + G)$), then the particle/cell will be moved by the flow; otherwise the particle/cell will be attached on the substrate. In our case, the gravitational force (G) is in the range of $10^{-17} \sim 10^{-15}$ N for different particles/bacterial cells, this force is considerably smaller than F_{MAX}^{XDLVO} ($10^{-15} \sim 10^{-13}$ N), thus being excluded from our analysis.

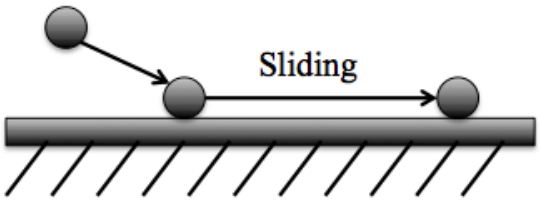

Figure 4.11 Particle/cell adhesion process onto a substrate.

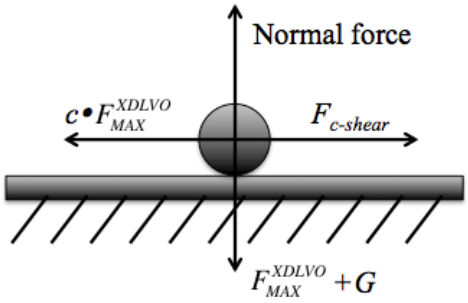

Figure 4.12 Schematic of forces applied on a particle/cell during attachment.

4.2.7 Interaction energy and attractive force based on the XDLVO theory

While transporting cells to the substrate surface, e.g. by settling and convective transport, is a pre-condition for cell attachment, the initiation of adhesion/attachment is likely dependent on the interaction energy and force between the particles/cells and the surface. Particles and cells will attach to the surface only when the interaction energy is negative. One way to estimate the interaction energy and the maximum attractive force is by applying the XDLVO theory.

Summarized in Table 4.6 are the experimentally measured quantities needed for the XDLVO analysis. These include the Lifshift-van der Waals (LW) (γ^{LW}) and acid-base (AB) (γ^{AB}) components ($\gamma^{AB} = 2\sqrt{\gamma^{+}\gamma^{-}}$, where γ^{+} and γ^{-} are the electron acceptor and electron donor parameter, respectively) of surface energies, calculated based on the contact angles (data provide in Supplementary Information) of water, methylene iodide, and ethylene glycol formed on the surface. Also included are the zeta potentials and the size of bacterial cells, with latter determined using AFM scans, examples of which are presented in Figure 4.13.

Table 4.6 The surface energies and their components of bacterial/particle lawns, the zeta potentials (ζ) and equivalent radius (R) of the bacteria/particles used in this study are summarized. Surface energy (γ) and its components (γ^{LW}, γ^{AB}, γ^{+}, and γ^{-}) are calculated based on contact angles of water, methylene iodide, and ethylene glycol formed on the lawns.

	γ	γ^{LW}	γ^{AB}	γ^{+}	γ^{-}	ζ (mV)	R^a (μm)
PS-AL	48.2	48.2	~ 0	4.2	~ 0	-18.9	0.26
PS-CML	49.5	49.5	~ 0	~ 0	43.7	-37.2	0.26
S. epidermidis	46.0	26.5	19.4	1.6	59.1	-31.8	0.51
E. coli	38.3	22.8	15.5	0.7	91.5	-36.0	0.26
PAO1	41.6	26.2	15.4	1.2	51.2	-32.0	0.24
P. putida	43.2	24.9	18.3	1.3	64.5	-30.0	0.22
glass	45.2	45.0	0.2	~ 0	64.6	-22[b]	-
OTS	23.0	22.7	0.3	0.1	0.4	-62[c]	-

Note: The unit of all g values is mJ/m^2.

[a]: The radius is estimated from the AFM image by assuming the cell is spherical and having an equivalent volume to that estimated from the 3D topographic scan.

[b]: Value from Ref. [95];

[c]: Value from Ref. [96].

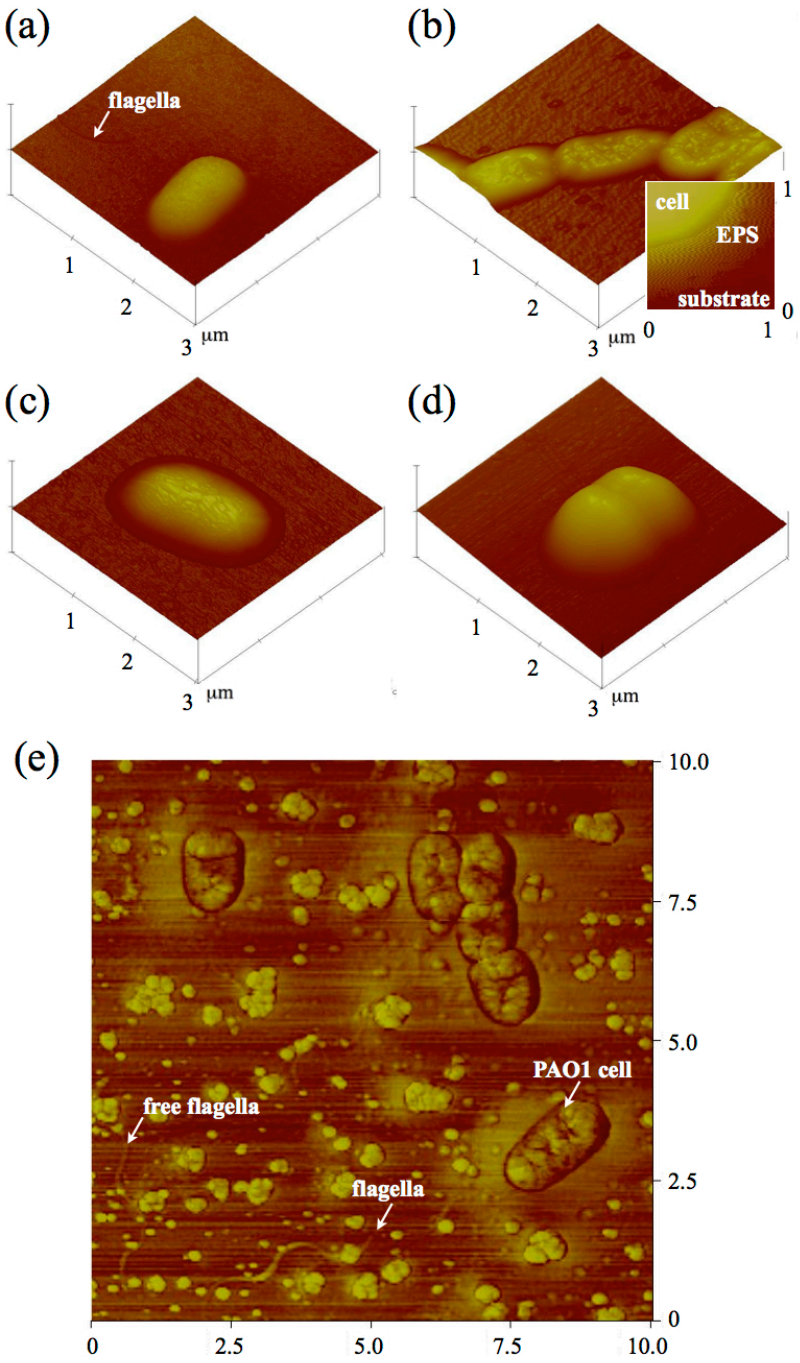

Figure 4.13 Atomic force microscopic (AFM) topography scans of the four bacterial strains: (a). PAO1, (b). *P. putida* (the inset is a more magnified AFM topographic scan showing EPS surrounding a cell when the cells are not washed prior to scanning), (c). *E. coli*, and (d). *S. epidermidis* are presented. The arrow in (a) pointed to a flagella that fell off the cell. Each of the scan is 3 × 3 mm^2, and the z-scale is 1000 nm. (e). The phase image (10 × 10 mm^2) of PAO1 and their flagella are presented. The harder deposits observed in the phase image could be salt aggregates formed as the medium dried up.

The secondary minimum interaction energies (ΔG_{sm}^{XDLVO}) and the maximum attractive forces (F_{MAX}^{XDLVO}) towards the secondary energy minimum for all the bacterial species/particle – substrate combinations are presented in Table 4.4. All of the twelve interaction energy curves (six of them are presented in Figure 4.14) showed negative secondary energy minima, which are the slight depressions in the XDLVO energy curves at a separation of 20 – 40 nm. All these curves also had a primary energy minimum at the smallest possible separation or 0.158 nm. The existence of negative secondary energy minima implies attractive interactions between cells and substrates for the attachment to occur. The value of F_{MAX}^{XDLVO} was obtained by differentiating the energy expression involved in the XDLVO theory with respect to distance.

Based on the experimental attachment vs. shear stress trend, the critical shear stress (s_c), at the point where the attachment started to decrease with the increase of shear, for each combination was obtained. The critical shear force ($F_{c\text{-}shear}$) acting on an particle/cell was then computed using $F_{c-shear} = (6\pi\mu RUc)f$, where U_c is the average fluid velocity of the flow having s_c at the liquid/chamber–wall interface when flowing through the chamber, and f is a coefficient of force acting on a sphere, which has a value ~ 1.7 [112-115]. The values of $F_{c\text{-}shear}$ for the twelve combinations are also presented in Table 4.4.

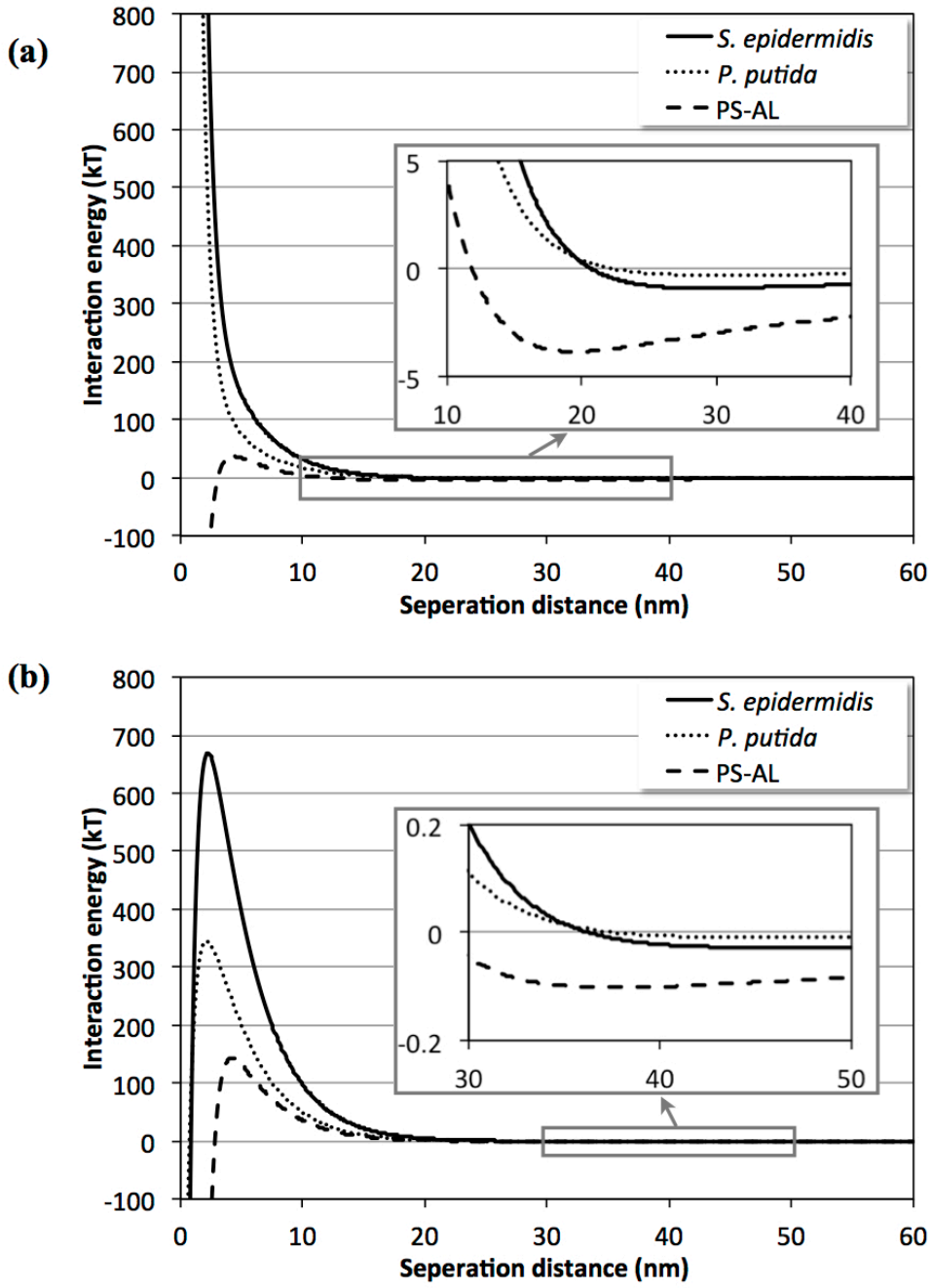

Figure 4.14 The XDLVO interaction energy curves of *S. epidermidis*, *P. putida*, and PS particles on (a). glass and (b). OTS surfaces are presented.

As indicated in the introduction, the interaction energy and force predicted by the DLVO/XDLVO theory are associated with initiation of attachment/adhesion between the particles/cells and the surface. When a particle/cell arrives to the surface, it will likely travel on the surface for some distance before attaching to the surface (see more details in the Supplemental Information). This indicates that $F_{c\text{-}shear}$ can be related to F_{MAX}^{XDLVO} as: $F_{c\text{-}shear} = c\,F_{MAX}^{XDLVO}$ (c is a coefficient) when the two forces are perpendicular to each other. In our case, the DLVO/XDLVO force acts perpendicularly to the surface, and the shear force exerted by the flow acts parallel to the surface. As a result, particles/cells will attach to the surface when the shear force is less than $F_{c\text{-}shear}$. If traveling on the surface prior to attachment is mainly sliding, c will be the coefficient of friction. With glass as the surface, the value of c is reported to be 0.1 to 1 [116], we would expect to see $F_{c\text{-}shear} = (0.1 - 1)\,F_{MAX}^{XDLVO}$ if no additional interactions/bonding is involved during attachment.

Polystyrene particles

For the PS-AL used in this study, F_{MAX}^{XDLVO} was ~ 410 fN on glass and was ~ 7.2 fN on the OTS surface. The critical shear stress obtained based on the experimental data was ~ 175 mN/m^2 for glass and ~ 2.5 mN/m^2 for the OTS surface, respectively (Figure 4.8), beyond which the attachment dropped sharply. These stress values corresponded to the shear forces of ~ 438 fN and ~ 6 fN. By applying $F_{c\text{-}shear} = c\,F_{MAX}^{XDLVO}$, a c value of ~ 1.07 and 0.83 for glass and the OTS modified glass, respectively, was obtained. These values are reasonable frictional coefficients for polystyrene sliding against glass. The data in Figure 4.8 also showed that before reaching the critical value, the attachment increased gradually with shear. Based on the XDLVO analysis, the maximum attractive force of

the cells/particles occurred at ~40-50 nm above the substrate, so the cells passing by, due to fluid flow and gravitational settlement, in this distance range could be attracted to attach to the surface, as long as the shear force was lower than the critical value.

Similar results were obtained by using PS-CML particles (Figure 4.9). In this case, the critical shear stress of particles on glass was found to be ~ 150 mN/m^2 (i.e. shear force ~ 375 fN), and it was ~2.5 mN/m^2 (i.e. shear force ~ 6 fN) for the OTS surface (Table 4.4). By dividing F_{MAX}^{XDLVO}, the value of *c* was ~ 1.07 and 0.88 for glass and the OTS modified glass, respectively, very similar to those values obtained for the PS-AL. Since both types of particles were polystyrene based, it was not surprising to find the frictional coefficient to be basically the same.

S. epidermidis

S. epidermidis is a Gram-positive bacterium with a rigid cell wall [117, 118]. It was expected that the *S. epidermidis* cells would behave more like inert particles as compared to the Gram-negative bacteria. The AFM scan (Figure 4.13(d)) showed the *S. epidermidis* cells were indeed more rigid, with no noticeable extracellular polymeric substances (EPS) or surface appendages. Using the XDLVO theory, the *S. epidermidis* attachment on glass was estimated to have a F_{MAX}^{XDLVO} ~ 98 fN. Experimentally, $F_{c\text{-}shear}$ was found to be ~ 29 fN (i.e. a shear stress of ~ 5 mN/m^2, Figure 4.9(a)), which lead to a *c* value of 0.30. The *S. epidermidis* attachment on the OTS surface had F_{MAX}^{XDLVO} ~ 2.2 fN. The experimentally obtained $F_{c\text{-}shear}$ was ~ 15 fN (i.e. a shear stress of ~ 2.5 mN/m^2, Figure 4.9(b)). In this case, the value of *c* was ~ 7.

E. coli

Due to the thicker outer cell membrane, the attachment of Gram-negative bacteria might be harder to explain by the XDLVO theory, which was developed for the interactions of inert particles. Among the three Gram-negative bacterial species investigated, the shear dependent attachment behaviors of *E. coli* appeared to follow the trend predicted by the XDLVO theory. This strain of *E. coli* (ATCC 11303) was rod-shaped with a smooth featureless surface as shown in Figure 4.13(c). The F_{MAX}^{XDLVO} estimated based on the XDLVO theory was ~ 8.5 fN for the *E. coli*-glass combination, and it was ~0.21 fN for the *E. coli*-OTS combination. The experimental values of $F_{c\text{-}shear}$ were found to be very small, i.e. < 5 fN (or < 1 mN/m^2 for the shear stress) for both cases, as shown in Figure 4.9. While the value of *c* could not be obtained under our flow condition (the smallest shear stress is 1 mN/m^2), it would likely be small (e.g. < 0.6) for glass, and it might still be high (e.g. < 250) for the case of OTS.

P. aeruginosa

As mentioned earlier in the settlement section, PAO1 cells likely initiated the contact for attachment onto surfaces, especially on hydrophobic surfaces, by their flagella [104-106, 108, 109]. Some cells were observed to lose their flagella during culture preparation, for example by centrifugation, as shown in the AFM scans in Figure 4.13(a) & (e). These cells would probably attach to the surface due to the negative ΔG_{sm}^{XDLVO}. For PAO1 cells attached by flagella (with a radius of ~ 5 nm), the F_{MAX}^{XDLVO} estimated using the XDLVO theory for glass and OTS were ~ 0.9 and 0.02 fN, respectively, both were very small. As this attractive force could be easily overcome, the attachment would be

expected to only show a decreasing trend with shear stress over the entire shear stress range investigated. However, for both glass and the OTS surface, the decreasing trend was only observed when the shear stress was greater than 5mN/m^2 (Figure 4.9), meaning the critical shear stress was ~ 5mN/m^2 or $F_{c\text{-}shear}$ of 9 fN. For PAO1 cells attached to the surface without using flagella, the estimated F_{MAX}^{XDLVO} was ~ 42 fN for glass, which lead to a *c* value of 0.21. While such a small frictional coefficient was possible, it was also possible that mixed extents of flagellum were involved in the attachment of PAO1 to glass, but predominately by the attractive interactions of PAO1 cells and the surface.

For PAO1 on OTS, the experimentally obtained $F_{c\text{-}shear}$ was ~ 9 fN (i.e. a shear stress of ~ 5 mN/m^2, Figure 4.9(b)), leading to a *c* value of 10 if attached by attractive interactions or 450 if attached via flagella. In either case, the value of *c* was much higher than anticipated.

P. putida

P. putida cells appeared to be surrounded by soft substances as shown in Figure 4.13(b), which could likely be the extracellular polymeric substances (EPS) they secreted [19, 119]. These EPS might help in anchoring *P. putida* cells to the substrate [119, 120]. Also Mittelman et al. [119] observed that the amounts and percentages of both proteins and carbohydrates in EPS increased with the increase of shear. As a result, the attachment of *P. putida* on the OTS surface, with the help of EPS, could be firmer and increasing with shear at a higher shear range (> 2.5 mN/m^2) as compared to that on glass (Figure 4.9). This could also explain why the ratio of attachment/settlement for *P. putida* on OTS was higher (i.e. 0.9) than the ratios (i.e. 0.3-0.5) observed for most of the other cases. On

glass, the F_{MAX}^{XDLVO} estimated was ~ 25 fN, while $F_{c\text{-}shear}$ could not be determined under our experimental flow conditions. Also it was observed that the *P. putida* attachment on glass also increased at higher shear stresses, between 25 and 50 mN/m^2. One possible reason could be that more EPS were secreted at higher shears and strengthened the cell attachment on the surface, as previously observed by Mittelman et al. for *Pseudomonas atlantica* [119].

Bacterial Attachment on OTS

It was initially surprising when the high coefficients (i.e. *c* values) were resulted for *S. epidermidis*, *E. coli* and PAO1 attached to the OTS surface. When examining it closely, we noticed that the LW component (22.7 mJ/m^2) of surface energy of OTS was very similar to that (21.8 mJ/m^2) of water, whose surface tension and its components were assumed to be the same as our culture medium used for the attachment study. The small difference between the two LW components led to the small attractive adhesive force. The value of 22.7 mJ/m^2 was obtained from the freshly prepared and well cleaned OTS surface. We re-evaluated the surface properties of the OTS after attachment and noticed that the LW component of the OTS surface had increased to a value of 27 – 32 mJ/m^2, even after the surface had been thoroughly rinsed with DI water. One possible reason could be the adsorption of proteins onto the highly hydrophobic OTS surface, and some common proteins have a LW component of 27 – 44 mJ/m^2 [42]. If a small amount of proteins secreted by bacterial cells did adsorb on the OTS surface during the bacterial attachment experiment, we should have taken this into account when estimating the interaction energies and forces. When we used 27 mJ/m^2 as the LW component for the

OTS surface, the values of F_{MAX}^{XDLVO} for *S. epidermidis*, *E. coli* and PAO1 on OTS were found to be 11 fN, 1 fN, and 10 fN (attached by attractive interactions), respectively, leading to the *c* value close to 1 for all three cases. The higher *c* values for these bacterial cells sliding against OTS as compared to sliding against glass could be that the cells were softer and their surface appendices (e.g. flagella) might interact more strongly with the OTS surface. While the frictional behaviors of different particle/cell-substrate combinations were not fully understood, our results indicated that the shear force could be associated with the attractive force and affected initial attachment. Therefore, for the attachment that involved particles/cells attaching to the surface as whole cells, it was likely the cells arrived on the surface and then slid on the surface for some distance under the attractive force prior to attachment. As a result, the shear force preventing the attachment of particles/cells could be related to the maximum attractive force predicted by the DLVO/XDLVO theory.

4.2.8 Summary

The effects of shear stress on initial attachment of PS particles and one Gram-positive bacterium and three Gram-negative bacteria on hydrophilic glass and hydrophobic OTS modified glass were investigated. In most cases, when shear increased beyond a critical value, the attachment number decreased. For PS particles as well as the bacterial cells of *S. epidermidis* and *E. coli*, which exhibit rather rigid and smooth surfaces (more particle-like), the shear dependent attachment behaviors could be associated with the maximum attractive force towards the secondary energy minimum predicted by the XDLVO theory. For these cases, the maximum attractive forces, F_{MAX}^{XDLVO}

were related to the experimentally obtained critical shear forces, for preventing attachment $F_{c-shear}$, as $F_{c-shear} = c \cdot F_{MAX}^{XDLVO}$. For bacteria having features/surface properties that derivate from those of inert particles, these features/properties (e.g. flagella of PAO1, EPS of *P. putida*) appeared to contribute to the un-anticipated attachment behaviors (e.g. much higher attachment of PAO1 on the hydrophobic OTS surface, and increased attachment vs. shear for *P. putida*). The results obtained and analyses performed in this work, i.e. correlating the critical shear force for preventing attachment and the attractive force from the XDLVO theory, could provide a good fundamental framework for further development and help to understand and, eventually, predict the effect of shear on initial cell attachment.

4.3 Corrosion of carbon steel and aluminum alloy in the presence of *Pseudomonas aeruginosa* and *Escherichia coli* biofilm

This part demonstrates the results and discussion about corrosion of carbon steel and aluminum alloy in the presence of *Pseudomonas aeruginosa* and *Escherichia coli* biofilm. The subsections include bacterial attachments and biofilm formation, corrosion behaviors, corrosion rate, and summary.

4.3.1 Introduction

Corrosion is a natural but costly process of destruction [1]. It causes untimely and expensive failures of plants, equipment and components and becomes a health/safety hazard, and ultimately it could have devastating impacts on economy and resources. While most materials, including ceramics, polymers, semiconductors, are all susceptible to corrosion, corrosion for metals and metal alloys has been the primary concern.

Microbiologically influenced corrosion (MIC) is one of the worst forms of corrosion for metals. Booth [4] believed that 50% of corrosion failures in pipelines involved microbes, and Flemming [3] suggested that about 20% of the all corrosion on metallic material surfaces was related to MIC. The initial stages of microbial attachment on metal surfaces serve as a precursor to MIC [121]. Researchers have studied the attachment of algae, invertebrate cells and bacteria to various ceramic and polymer surfaces, but the bacterial attachment on metal surfaces in natural environment or industrial processes where MIC is a serious issue has not been extensively studied [34-37].

In this part of study, to better understand the influence of bacterial attachment and subsequent biofilm development to MIC, a flow chamber that allows *in situ* monitoring of bacterial attachment and following the biofilm development and associated metal corrosion was utilized [44]. Using the flow chamber also allowed the flow rate of the bacterial suspension, one of the most important parameters in the attachment of bacteria to surfaces [78], to be easily tuned. A slow flow condition that mimics the natural water environment was chosen. Aluminum coupons and carbon steel (CS) coupons along with two common bacterial strains, *Pseudomonas aeruginosa* PAO1 and *Escherichia coli*, were used. For aluminum, no visible/measurable difference in corrosion behaviors was noticed for the two bacterial strains. For CS, lower corrosion in the presence of the dense PAO1 biofilm, as compared to the control and coupons in the presence of loose E. coli biofilm, was observed. The lower carbon steel corrosion could be the result of the dense biofilm created a protective layer that inhibited further corrosion of the CS.

4.3.2 Bacterial Attachments and Biofilm Formation

During the 3 h of bacterial attachment, the number of attached cells increased with time on both glass and Al thin film surfaces, and the attachment results were very similar to our recent study [19]. After removal of the circulating bacterial cell suspension and flowing an enriched cell free medium over the attached cells, the cells started to grow and divide, formed cell colonies, and finally the colonies connected together to form a biofilm on the inside chamber surfaces and on the coupons. The biofilm continued to grow from one layer into multi-layers. Figure 4.15 presents a series of representing images showing the growth of attached PAO1 cells on Al thin film surfaces as the

enriched medium flowed through the flow chamber. The entire process was observed under an optical microscope video system, and the process during the first 24 hours was continuously recorded. As seen in Figure 4.15, after 24 h, the entire surface was covered by a PAO1 biofilm, and the surface coverage had reached ~ 100%. Figure 4.16(a) summarizes surface coverage vs. time for both bacterial strains. For PAO1, the surface coverage increased dramatically from 6% at 16 h to 100% at 24 h. After that, the biofilm continued to develop in the thickness direction with growing of cells and attaching of cells and cell aggregates that detached from the biofilm and grew in the medium. For *E. coli*, as the doubling time was found to be shorter than PAO1 under the same growth condition, a faster biofilm formation was noticed. The surface coverage of *E. coli* jumped from about 6% in 12 h to ~ 100% in 19 h, and the biofilm thickness continued to increase with time. Meanwhile, the thicknesses of biofilms on metal surface were also measured. Figure 4.16(b) presents PAO1 and *E. coli* biofilm thickness on CS coupon surface. The growth trends for both bacteria were similar: growing dramatically/exponentially during the first 6 days, and then the rate of growth slowed down during day 6 to day 9. After 9 days, the thicknesses of biofilms were stabilized at ~ 130 μm for PAO1 and ~ 105 μm for *E. coli*.

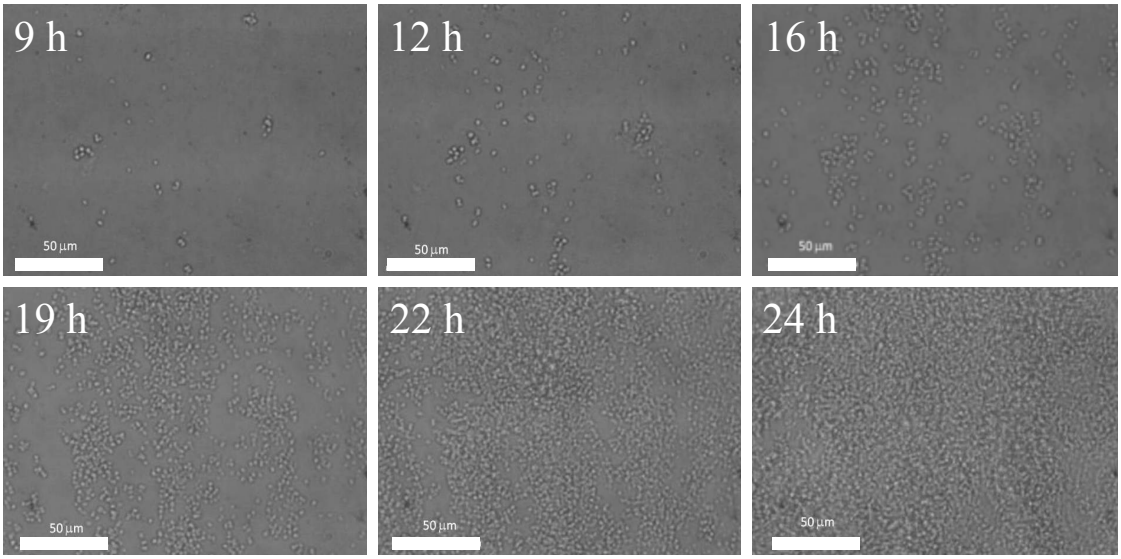

Figure 4.15 A series of representing images show the growth of attached PAO1 cells on Al thin film surfaces as the enriched medium flowed through the samples. Scale bars represent 50 μm.

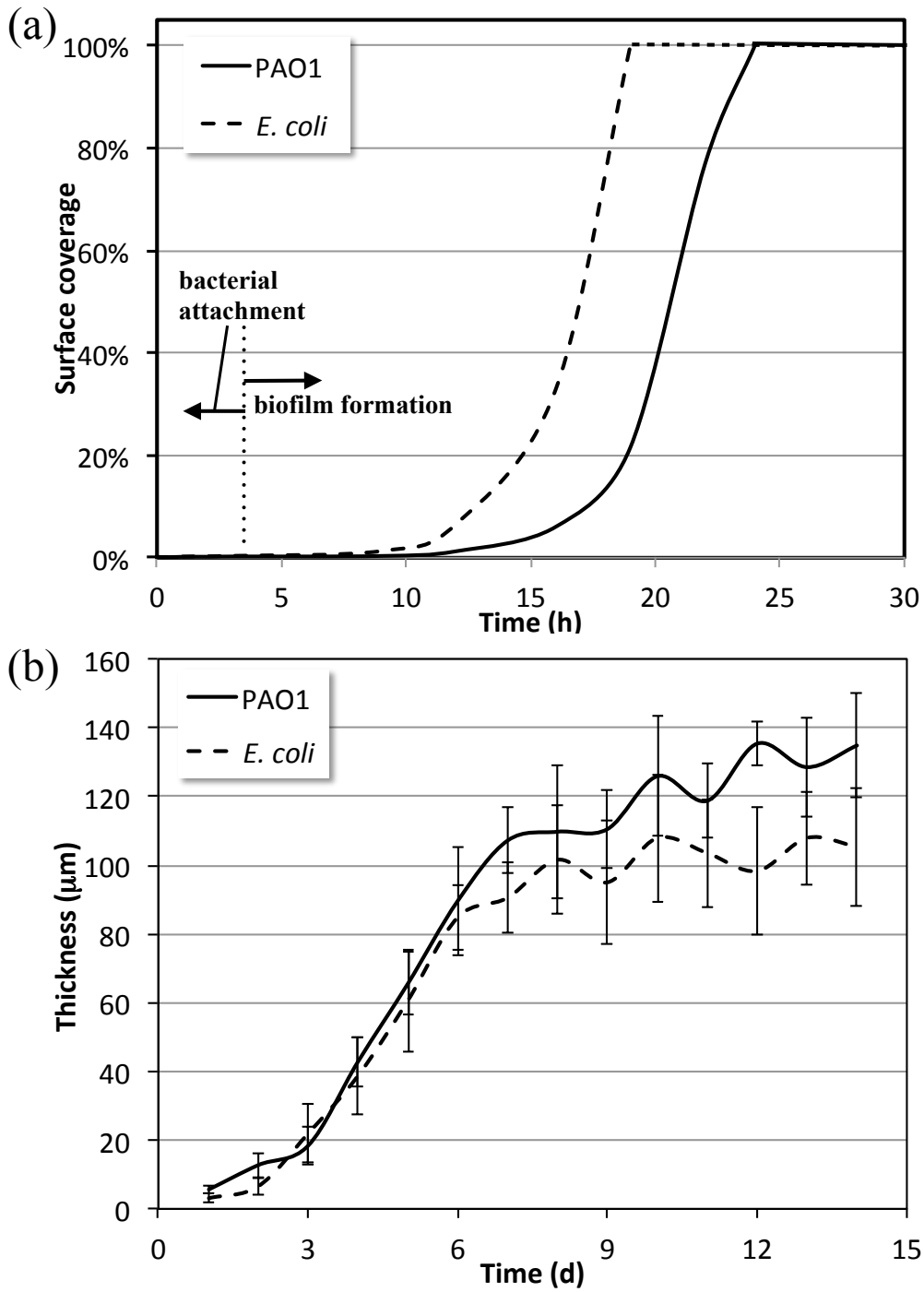

Figure 4.16 (a). The surface coverage of PAO1 and *E. coli* vs. time is summarized. (b). PAO1 and *E. coli* biofilm thickness vs. time on CS coupon surface is presented.

4.3.3 Corrosion Behaviors

As enriched medium continuously flowing over the coupons and the biofilm being formed inside the flow chambers, corrosion happened on the CS coupons surfaces. After a few days, coupons were covered by biofilms, and some yellow-brownish corrosion products surrounding the CS coupons were noticed. Close up views of the CS coupons show a sufficient amount of corrosion products was covering the control samples as well as the coupons in the chamber containing *E. coli* (Figure 4.17(a) and Figure 4.17(c)). The CS coupons in the chambers containing PAO1, on the other hand, were found to be covered by a uniform layer of pinkish/brownish slim and underneath the slim grey/black materials (Figure 4.17(b)).

After 14 days, the coupons were taken out of the chambers and the biofilms morphology and structure were examined by confocal microscopy after stained by Live/Dead, green SYTO 9/red propidium iodide fluorescent staining solution. The representative 3-D biofilm structures of PAO1 and *E. coli* were presented in Figure 4.18. According to the 3-D biofilm structures, the thicknesses of PAO1 and *E. coli* biofilm were ~ 120 μm and ~ 110 μm, respectively, which agreed with the results, shown in Figure 4.16(b), obtained using the optical microscope. In the 3-D images, each green dot, size ranging from 0.5-2 μm, was a bacterial cell. In this case, the biofilm of PAO1 was much denser than that of *E. coli*. The density of bacterial biofilm might affect oxygen diffusion from the bulk medium to the metal coupon surface, and thus affecting the bacterial metabolism of those cells underneath the biofilm and in direct contact with the metal coupon.

After the coupons were cleaned by following the standard cleaning procedure and dried with compressed N_2, optical microscope pictures were taken to compare the changes in surface morphology. The Al coupons did not show much difference between the controls and those coupons in the chamber containing PAO1 or *E. coli* biofilm (data not shown). The CS coupons (Figure 4.17(d)-(g)) of control and the ones with *E. coli* were also similar; both showed relatively rougher surfaces as compared to those coupons prior to the run. The CS coupons in the chambers containing PAO1 showed a smoother surface as compared to controls and those with *E. coli*. It was likely that the uniform black layer on the CS coupon in the chamber containing PAO1 biofilm had some protection for the CS surface from further corrosion. This result agreed with the results obtained from the surface roughness obtained from the IFM images, which was presented in Table 4.7. The surface roughness of all Al coupons was quite similar with an average surface roughness (Ra) of ~ 670 nm, indicating the cell medium and these two strains of bacteria caused no corrosion for this Al alloy (3003 H14). For CS C1010, post run coupons had higher surface roughness than those prior to the experiments. Comparing the post run coupons, controls and those with *E. coli* showed similar surface roughness (Ra ~ 1600 nm), while the coupons with PAO1 biofilm presented had a smoother surface (Ra ~ 1000 nm) with fewer shallow pits as compared to those of control and those with *E. coli*.

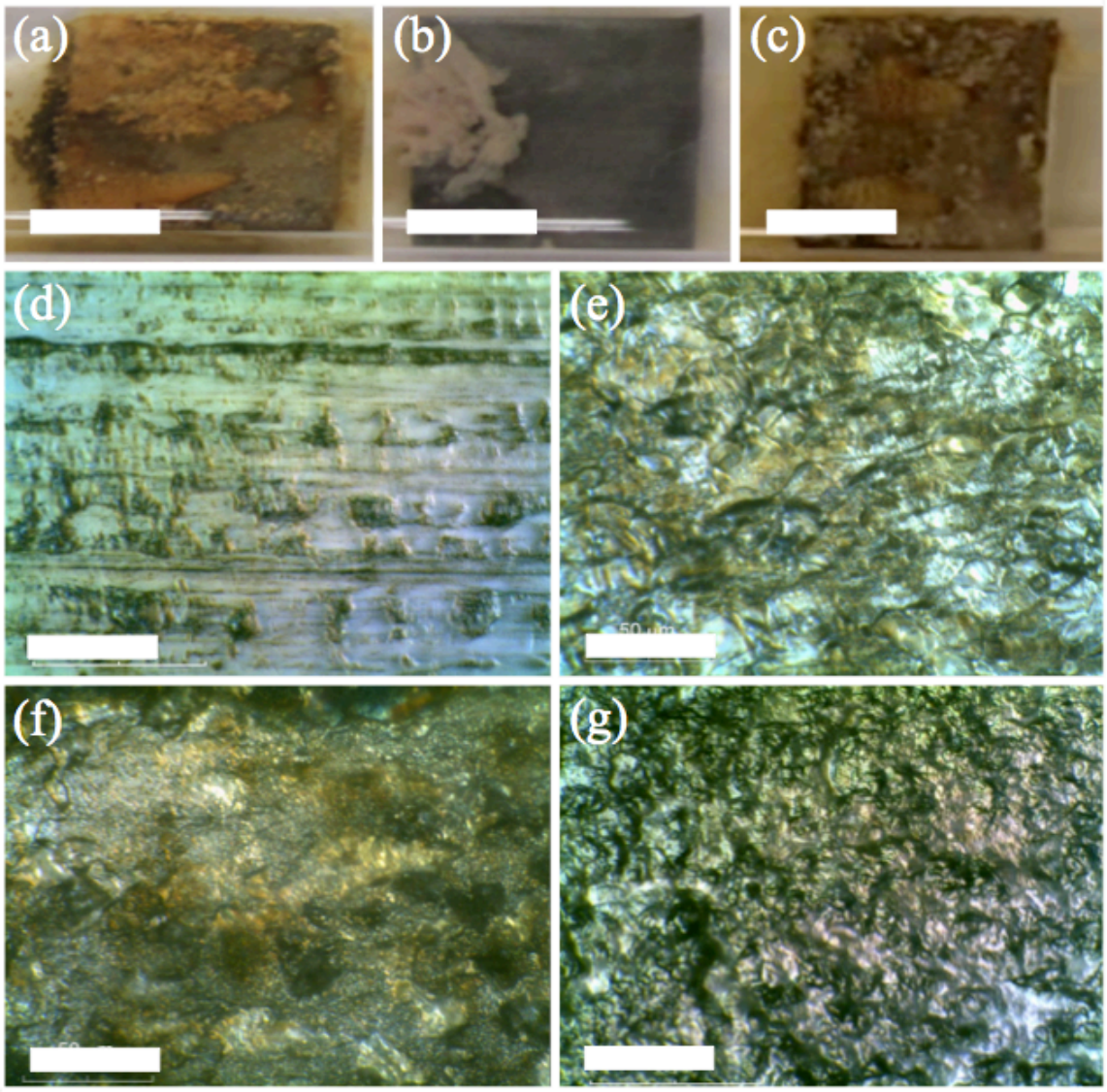

Figure 4.17 The respective digital and optical microscope images of CS coupons in (a) & (e). control, (b) & (f). with PAO1, and (c) & (g). with *E. coli* after 14 days inside the flow chamber are presented. (d) is the optical microscope image of CS coupon prior to the run. Scale bars represent 5 mm in (a) – (c) and 50 μm in (d) – (g).

Table 4.7 The table summarizes the average roughness (Ra) of Al and CS coupons prior to the runs, and of the coupons submerged 14 days in control flow chambers and in flow chambers with PAO1, and with *E. coli*.

Ra (nm)	Al	CS
Prior to run	674.9 ± 63.0	813.1 ± 89.6
Control	670.3 ± 57.8	1656.8 ± 111.2
w. PAO1	664.4 ± 75.1	1047.5 ± 155.0
w. *E. coli*	682.9 ± 62.5	1596.6 ± 94.0

PAO1 biofilm

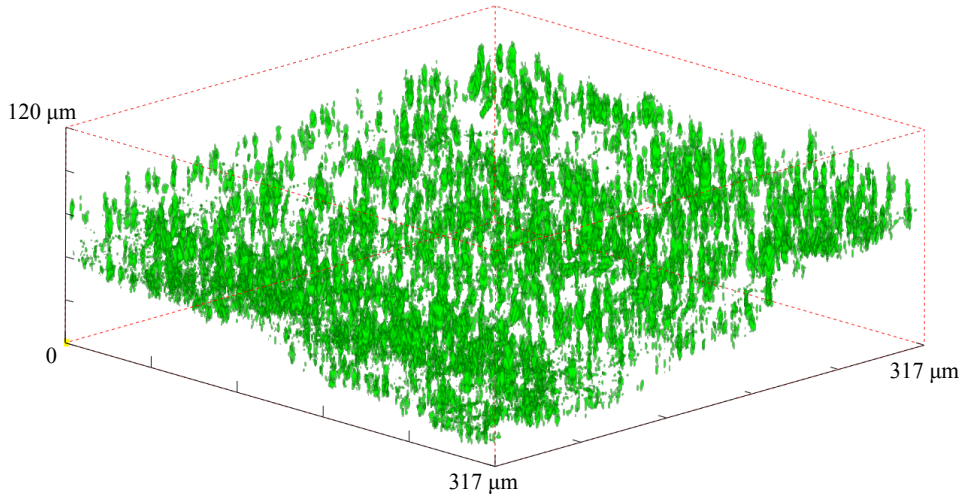

E. coli biofilm

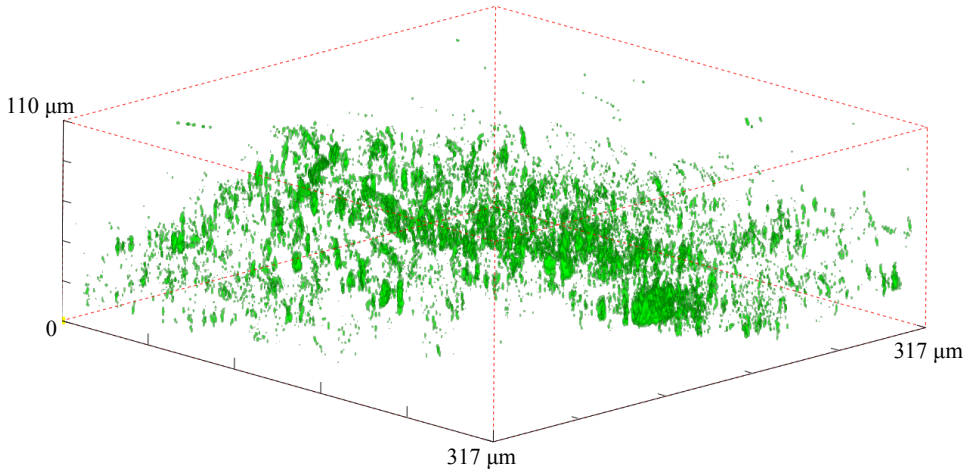

Figure 4.18 The 3-D laser scanning confocal microscopy images of PAO1 and *E. coli* biofilm stained with Live/Dead fluorescent stain solutions are presented. The green dots are live bacterial cells.

4.3.4 Corrosion Rate

The corrosion rates were calculated based on the weight loss of coupons and using Eq. (1). For the Al coupons, corrosion rate was found to be close to zero for all three systems (data not shown), indicating little to no corrosion of these Al coupons under our experimental condition, with or without bacterial biofilm. Corrosion was observed for CS in all three systems. Table 4.8 summarizes the corrosion rates of CS coupons in the three systems at two time periods, 7 d and 14 d. The control CS coupons had the highest average corrosion rate of 5.8 mpy over the first 7 days, and the average rate decreased slightly to 3.4 mpy over the 14 d period. The CS coupons with *E. coli* biofilm had similar corrosion rates as those of controls: 5.5 mpy over the first 7 days, and decreased to 3.4 mpy over the 14 d period. The CS coupons with PAO1 biofilm had the lowest corrosion rate of 4.4 mpy over the first 7 days, and decreased slightly to 2.8 mpy over 14 d. The lower corrosion rate for the coupons with PAO1 biofilm could be due to the protection from the corrosion product layer and biofilm formed on CS coupon surface.

To determine how the different corrosion behaviours could be caused by metabolism of bacterial cells within the biofilm, the dissolved oxygen (DO) levels under PAO1 and *E. coli* biofilm as well as in the control system were followed and presented in Figure 4.19. Briefly, in control system, without any biofilm, the dissolved oxygen level maintained at ~ 75 % air saturation; while under both PAO1 and *E. coli* biofilms, the dissolved oxygen level dropped dramatically from the initial of ~ 75 % air saturation to ~ 0 after 2 d, as such the cells underneath the biofilm would need to survive with anaerobic metabolism 2 d after forming the biofilm. Under the oxygen depleted condition, CS

coupon corrosion caused by the presence of water and oxygen could be reduced/inhibited to result in a lower corrosion rate. In addition, metabolites generated by cells under anaerobic condition could affect corrosion behavior of metal coupon. Under anoxic condition while with sufficient carbon source and nutrient, *E. coli* cells can produce organic acid by converting carbon source, thus lowering the pH of local environment at and near the metal surface [122], which could accelerate metal corrosion. This phenomenon could counteract the reduced corrosion by the low oxygen level; hence the total corrosion of CS in the presence of *E. coli* biofilm was similar to that of control. On the other hand, PAO1 not only can utilize nitrate as the electron acceptor to generate nitrogen gas [123], but also can employ Fe(III) as the electron acceptor to produce Fe(II) under the anaerobic respiration [124, 125]. This might be the reason for the formation of the grey/black uniform layer noticed on the CS coupon surface in the presence of PAO1 biofilm. In this case, the presence of Fe(II) layer on the CS coupon surface could further inhibit corrosion due to the increased consumption of oxygen by the Fe(II) layer trapped under PAO1 biofilm [126].

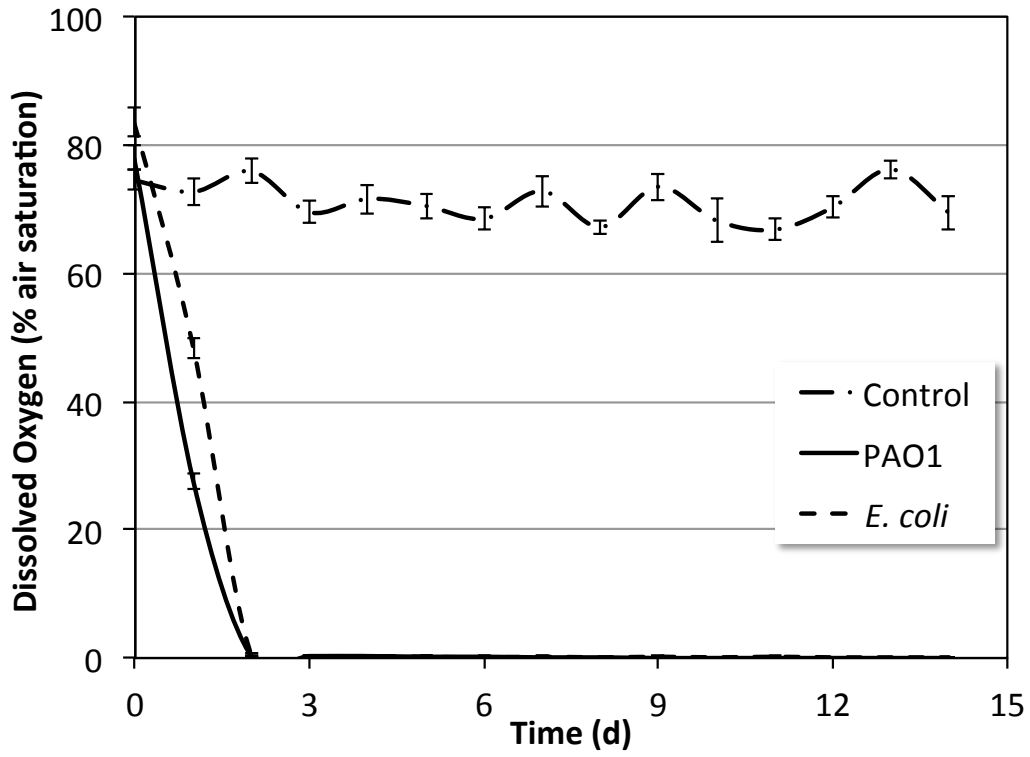

Figure 4.19 The dissolved oxygen (DO) level in the control system and underneath the PAO1 and *E. coli* biofilm are shown.

Table 4.8 The corrosion rate of CS coupons in control, with PAO1, and with *E. coli* after submerged in the flow chambers for 7 d and 14 d are presented.

Material/bacteria	Corrosion rate (mpy)	
	Over 7 days	Over 14 days
CS coupons/control	5.8 ± 0.6	3.4 ± 0.4
CS coupons/PAO1	4.4 ± 0.5	2.8 ± 0.3
CS coupons/*E. coli*	5.5 ± 0.5	3.3 ± 0.5

4.3.5 Summary

Some preliminary correlations between the biofilm development and MIC behaviors were obtained in this study. By using the flow chamber system, we were able to monitor the bacterial attachment and biofilm formation, in term of bacterial coverage and biofilm morphology/thickness, respectively. Some real time corrosion behaviors were also observed, in particular with the corrosion products generated on the CS coupons. In general, aluminum surfaces showed no noticeable corrosion in the presence of these two bacterial strains. However, corrosion was found to be quite significant for CS, and the extent of CS corrosion in the presence of bacterial biofilm depended on the bacterial species. *P. aeruginosa* PAO1 biofilm was found to have some inhibition effect on the corrosion of the CS coupon. The inhibition could be the result of the biofilm formed by the PAO1 cells, which could create an oxygen-free or oxygen-limited environment at/near the metal surface, reducing the oxidation induced corrosion of CS. On the other hand, little difference on CS corrosion was noticed between CS coupons in the control systems and those covered by *E. coli* biofilm.

4.4 Corrosion behaviors of carbon steel C1010 and stainless steel 304 in the presence of iron oxidizing bacteria *Acidithiobacillus ferrooxidans*

This part provides the results and discussion about corrosion behaviors of carbon steel C1010 and stainless steel 304 in the presence of iron oxidizing bacteria *Acidithiobacillus ferrooxidans*. The subsections include bacterial attachment and biofilm formation, corrosion evaluation, potential mechanism, CS coupon corrosion characterization, and summary.

4.4.1 Introduction

Iron-oxidizing bacteria induced aerobic corrosion is suggested to be a significant portion of MIC [21], and was also isolated and identified from different environments such as water tank [22] and pipelines [23]. *Acidithiobacillus ferrooxidans*, formerly *Thiobacillus ferrooxidans* [24], plays an important role of the metal oxidative activity [25]. The chemolithotrophic and acidophilic species utilizes ferrous (Fe(II)) as the sole energy source for CO_2 fixation at pH range from 2.0 to 4.5 condition [68]. Prior to this study, the real role of iron-oxidizing bacteria in carbon steel corrosion is still unclear [26]. Some attributed the corrosion caused by iron-oxidizing bacteria to the crevice corrosion mechanism, in which cells related to the formation of condensed oxygen zones and partition of the metal surface into small anodic sites [27, 28].

This part of study is designed to gain better understanding of the iron-oxidizing bacteria (*A. ferrooxidans*) corrosion behavior and mechanism. In this study, both carbon steel (CS) and stainless steel (SS) metal coupons were utilized and exposed in the cell medium with *A. ferrooxidans* cells. For SS coupon, no corrosion was detected after up to

28 days' exposure; while for CS coupon, after ruling out the pH effect on those coupons, *A. ferrooxidans* cells accelerated corrosion and even initiated pitting corrosion on the coupon surface right after 7 days' exposure.

4.4.2 Initial attachments in flow chamber system

As shown in Figure 4.20, during the 3 h of bacterial attachment, the number of attached cells increased with time and the increasing trends were similar on all three substrates. *A. ferrooxidans* attachment numbers for those on CS and OTS modified glass surface were similar. The attachment increased from 200 cells/mm^2 after 1 h to 330 cells/mm^2 after 3 h on CS and OTS modified glass; and increased from 100 cells/mm^2 after 1 h to 170 cells/mm^2 after 3 h on glass surface.

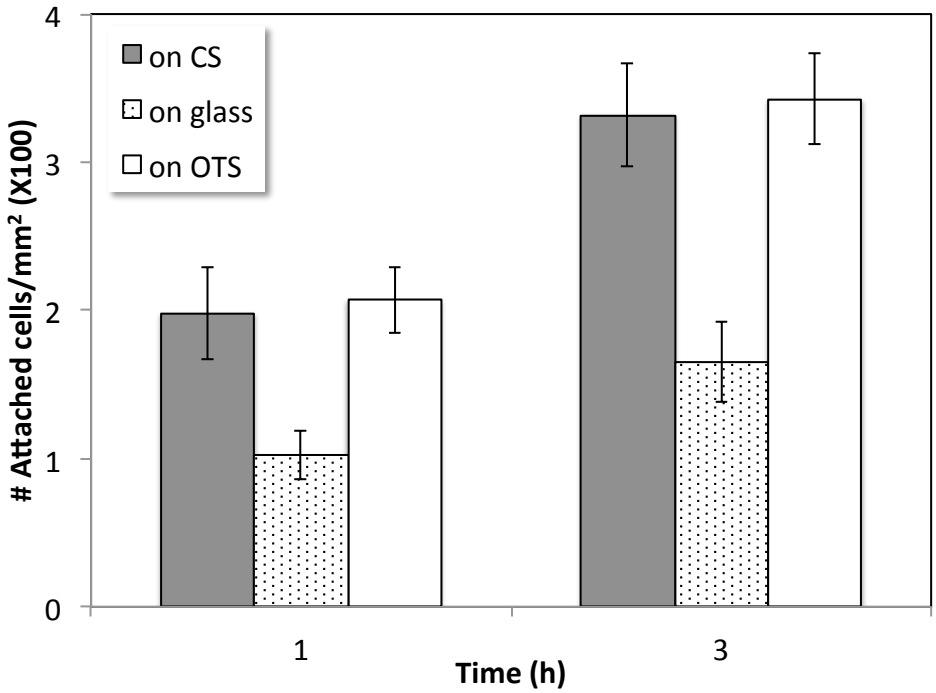

Figure 4.20 The initial attachments of *A. ferrooxidans* on the surfaces of CS, glass and OTS modified glass are shown. The errors shown for each data point is the standard deviation obtained from at least four sets of measurements.

4.4.3 Bacterial attachment and biofilm formation

To investigate the effect of *A. ferrooxidans* cell activities on metal corrosion, cell attachment and biofilm formation of *A. ferrooxidans* cells on CS and SS coupons were monitored and presented in Figure 4.21(a)-(f). After 1 d, some cells were randomly attached onto CS (Figure 4.21(a)) and SS (Figure 4.21(b)) surfaces. 7 d later, more cells were observed on the CS coupon surface, but no continuous biofilm was noticed. On the surface of SS coupons, very few cells were found. After gently rinsing the coupons with basal salts solution, most of the attached cells were removed from the CS coupon surface (Figure 4.21(c)), indicating a very weak attachment. For SS coupons, after rinsing, hardly any cells were found.

The cell concentration in the bulk medium (Figure 4.21(g)) was followed; initially, both systems, with CS or SS coupons, had a cell concentration of ~ 2×10^7 cells/mL, which decreased over time. For the system with CS coupons, the cell concentration decreased to ~ 1.2×10^7 cells/mL after 7 d, and then to ~ 0.75×10^7 cells/mL after 14 d, and basically remained at this value towards the end of the experiments (28 days). For the system with SS coupons, the cell concentration dramatically decreased to ~ 0.4×10^7 cells/mL after 7 d, and then to ~ 0 after 14 d.

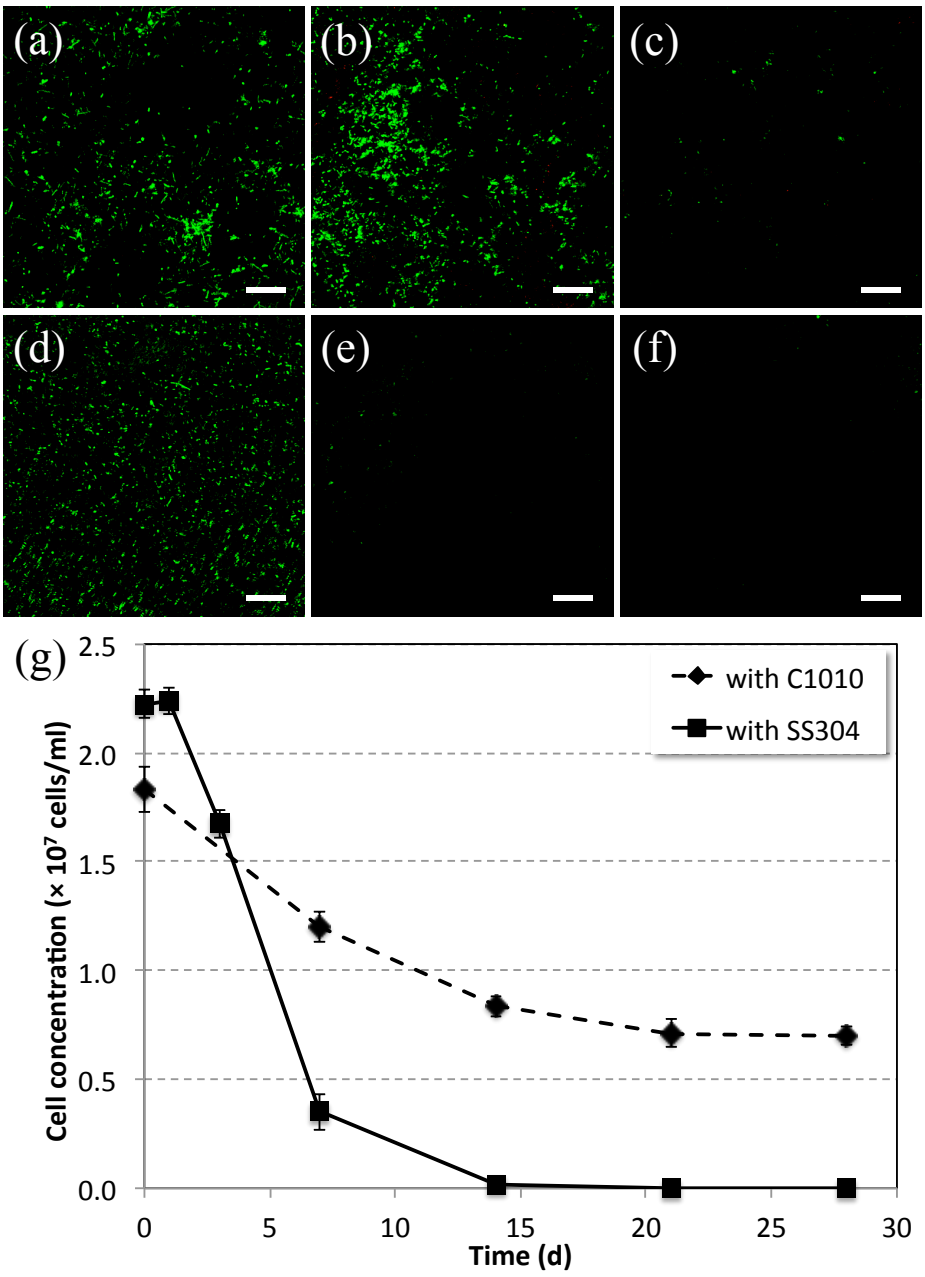

Figure 4.21 (a)-(c). The fluorescent confocal images of attached *A. ferrooxidans* cells on CS coupon surfaces after 1 d, 7 d, and after rinsed with diluted basal salts solution, respectively. Scale bars represent 20 μm. (d)-(f). The fluorescent confocal images of attached *A. ferrooxidans* cells on SS coupon surfaces after 1 d, 7 d, and after rinsed with diluted basal salts solution, respectively. Scale bars represent 20 μm. (g). The bacterial cell concentrations in bulk medium of with CS and SS coupon systems vs. time are presented. The errors shown for each data point is the standard deviation obtained from at least six sets of measurements.

4.4.4 Corrosion evaluation

Corrosion behaviors of CS coupons in control (pH ~ 2 DI water), cell medium (pH ~ 2), and in medium with cells (pH ~ 2) for 1, 3, 7, 14, 21, and 28 d, respectively, were briefly assessed by the weight loss method (ASTM D2688-05), and corrosion rates were calculated accordingly. As shown in Figure 4.22(a), in all three systems, weight loss of CS coupons increased as exposure time increased. Weight losses of CS coupons in control and in cell medium were similar during the initial 3 d. After 3 d, the weight losses in cell medium were ~ 50% higher than that of control system. For CS coupons submerged in the medium with cells, at every time period, much higher weight loss was observed as compared to those of control and those in the medium without cells. In particular, the weight loss was 4-5 times of that in the cell medium without cells. For the three systems, the corrosion rates (Figure 4.22(b)) of CS coupons decreased as exposure time increased. To be specific, the corrosion rate of CS coupons in the control system decreased from ~ 31 mpy over first day to ~ 7 mpy over the first 14 d, and then maintained at this corrosion rate afterwards. Similar results were found for CS coupons in the cell medium, corrosion rate decreased from ~ 28 mpy over day 1, to ~ 11 mpy over the first 14 d, and maintained at ~ 11 mpy over the rest of the experimental period (i.e. 28 days). For CS coupons in the medium with cells, the corrosion rate dropped from ~ 140 mpy over day 1 to ~ 60 mpy over first 3 days, and then the corrosion rate retained at ~ 40 mpy over a time period greater than 14 d.

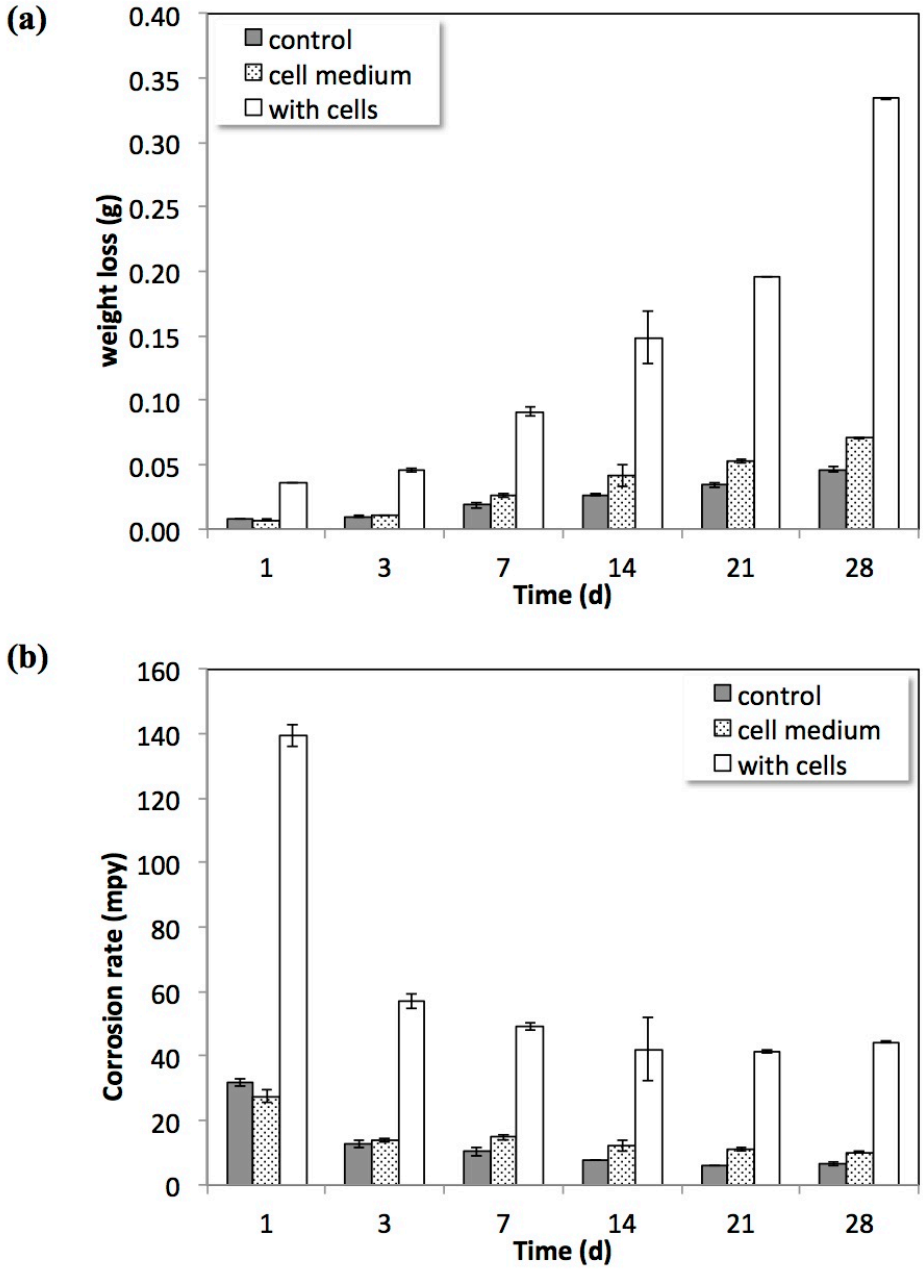

Figure 4.22 (a). The weight loss of CS C1010 coupons exposed in control (pH ~ 2 DI water), cell medium (pH ~ 2), and in cell medium with cells (pH ~ 2) for 1, 3, 7, 14, 21, and 28 days are shown. The errors shown for each data point is the standard deviation obtained from at least eight sets of measurements. (b). The corrosion rate of CS C1010 coupons exposed in control, cell medium, and with cells, all started with a pH of ~ 2, for 1, 3, 7, 14, 21, and 28 days are shown. The errors shown for each data point is the standard deviation obtained from at least eight sets of measurements.

On the contrary, the SS coupons were relatively stable in all three systems. After submerged SS coupons in all three systems for 28 d, no weight loss or corrosion rate was detected, the slight difference in weights measured for coupons before and after submersion could be due to the sensitivity (+/- 0.0002g, p=1) of the analytical balance used. These results might indicate that no corrosion occurred for SS coupon in the presence or absence of this iron oxidizing bacterium: *A. ferrooxidans*.

To evaluate surface morphological change of the coupons, IFM scanning and additional surface roughness analysis was conducted, and the data is summarized in Table 4.9. For CS coupons, those submerged in control and cell medium had similar average roughness (Ra), which was also similar to those of coupons prior to be used for the experiments (p=0.40). The results could suggest a uniform corrosion induced by the pH ~ 2 acidic conditions. Ra of the CS coupons submerged in the medium with cells showed a dramatically increase, from ~ 800 nm originally to ~ 2800 nm after 28 d of submersion. This result indicated that *A. ferrooxidans* cell activity might enhance corrosion occurred on the CS coupon surface. On the contrary, for SS coupons submerged in all three systems for over various time periods, no difference in surface roughness (p=1, Ra ~ 390 nm) was obtained, which was also basically the same as those non-submerged coupons. Combined with the non-detectable corrosion, it would be possible that SS coupon were immune to the pH ~ 2 acid solutions and *A. ferrooxidans* cells during the 28 d of submersion.

Table 4.9 Surface roughness of CS and SS in control, cell medium, and with cells systems prior to run, after 7 d, 14 d, 21 d, and 28 d's exposure, respectively.

Ra	CS			SS		
(nm)	Control	Cell medium	With cells*	Control	Cell medium	With cells
0 d	813.1 ± 89.6			380.9 ± 67.2		
7 d	799.0 ± 68.5	842.8 ± 76.2	1557.9 ± 167.8	392.9 ± 51.1	380.9 ± 54.7	385.3 ± 34.3
14 d	817.3 ± 80.9	856.5 ± 75.7	1704.9 ± 150.9	380.9 ± 67.2	406.9 ± 46.4	389.1 ± 41.8
21 d	820.8 ± 67.8	851.4 ± 66.7	2079.7 ± 266.4	406.2 ± 65.6	384.0 ± 55.8	404.9 ± 42.6
28 d	818.5 ± 68.0	852.1 ± 65.5	2768.8 ± 299.8	400.4 ± 64.3	401.7 ± 58.6	396.6 ± 50.9

Note: *: Pits were not included in the surface roughness analysis.

4.4.5 Potential mechanism

To further verify if there were reactions, especially proton (H^+) consumption, occurred on the CS and SS coupons surfaces in all three systems, pH of the solutions were followed and presented in Figure 4.24. For CS coupons (Figure 4.23(a)), the pH of medium with cells system remained at ~ 2. However, the pH of control and of cell medium both increased, from ~ 2 to ~ 4.5 and ~ 4, respectively, after one day. Afterwards, pH maintained at ~ 5 for control and ~ 4 for cell medium system containing CS coupons. During first day, gas bubbles were clearly observed in control and cell medium system, indicating that protons (H^+) were consumed by the Fe(0) oxidizing reaction, and generating Fe(II) and hydrogen (H_2) gas. While for systems containing SS coupons (Figure 4.23(b)), the pH of all three systems remained at ~ 2, and no noticeable physical or chemical properties change were observed on those coupon surface. This could suggest that no proton (H^+) was consumed, or no Fe(0) was oxidized during the 28 d of experiment.

As noticed in Figure 4.23(a), the pH of control and cell medium systems increased to ~ 5 and ~ 4 from ~ 2 after one day. In order to verify more corrosion occurred for CS in system with *A. ferrooxidans* was caused by cell metabolism rather than by the lower pH (Figure 4.23(a)), pH effect on CS coupon corrosion was evaluated in control and pH adjusted systems without cells. For the control system, CS coupons were submerged in pH ~ 2 DI water, weight loss and corrosion rate of the coupons, and pH of the solutions were measured after 1, 2, 4, 8, and 24 h, respectively. For the pH adjusted system, similar processes were followed; the only difference was the pH of the solutions was adjusted back to ~ 2 after each measurement, manually maintaining the pH

of the solutions at ~ 2. The weight loss, corrosion rate of the coupons and pH change of the solutions were shown in Figure 4.24. According to the results, CS coupons weight loss increased as exposure time increased for both systems. After 1 h, the weight loss of coupons in the control and pH adjusted systems were similar, afterwards, the weight loss of coupons in the pH adjusted system was found to be slightly higher than those in the control system. After 24 h, the average weight loss of CS coupons in the control system was ~ 0.008 g and that of the pH adjusted system was ~ 0.011 g. The corrosion rates for both systems were similar for the initial three hours, after 3 h, the corrosion rates decreased with time. In general, weight loss and corrosion rate of CS coupons in the pH adjusted system were slightly higher than those of coupons in the control system due to the lower pH (Figure 4.24(b)) that slightly increased the conversion of Fe(0) to Fe(II) in the solutions.

In the pH adjusted system, the corrosion rate was ~ 60% higher than that of control system after 24 h. However, in the with cells system, after 24 h, the corrosion rate was ~ 340% higher than that of control system, which was significantly enough to denote that the higher corrosion rate for CS coupons submerged in medium with *A. ferrooxidans* cells was probably contributed by cell metabolic activity of *A. ferrooxidans* (Figure 4.25).

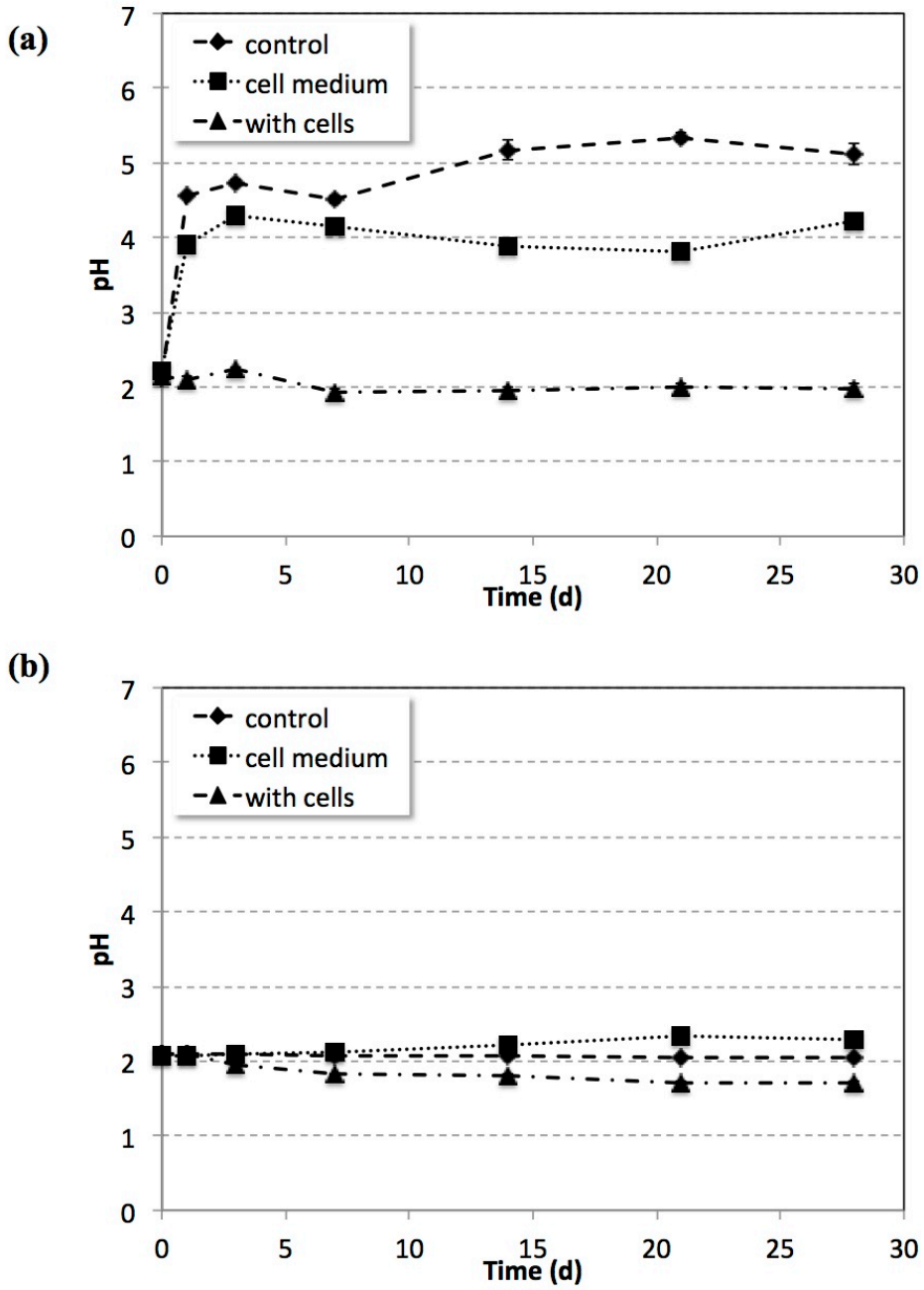

Figure 4.23 (a). The pH changes of acid/water, cell medium, and cell medium + cell culture with CS C1010 coupon in control, cell medium, and with cells systems, respectively, vs. time are shown. The errors shown for each data point is the standard deviation obtained from at least eight sets of measurements. (b). The pH changes of acid/water, cell medium, and cell medium + cell culture with SS 304 coupon in control, cell medium, and with cells systems, respectively, vs. time are shown. The errors shown for each data point is the standard deviation obtained from at least eight sets of measurements.

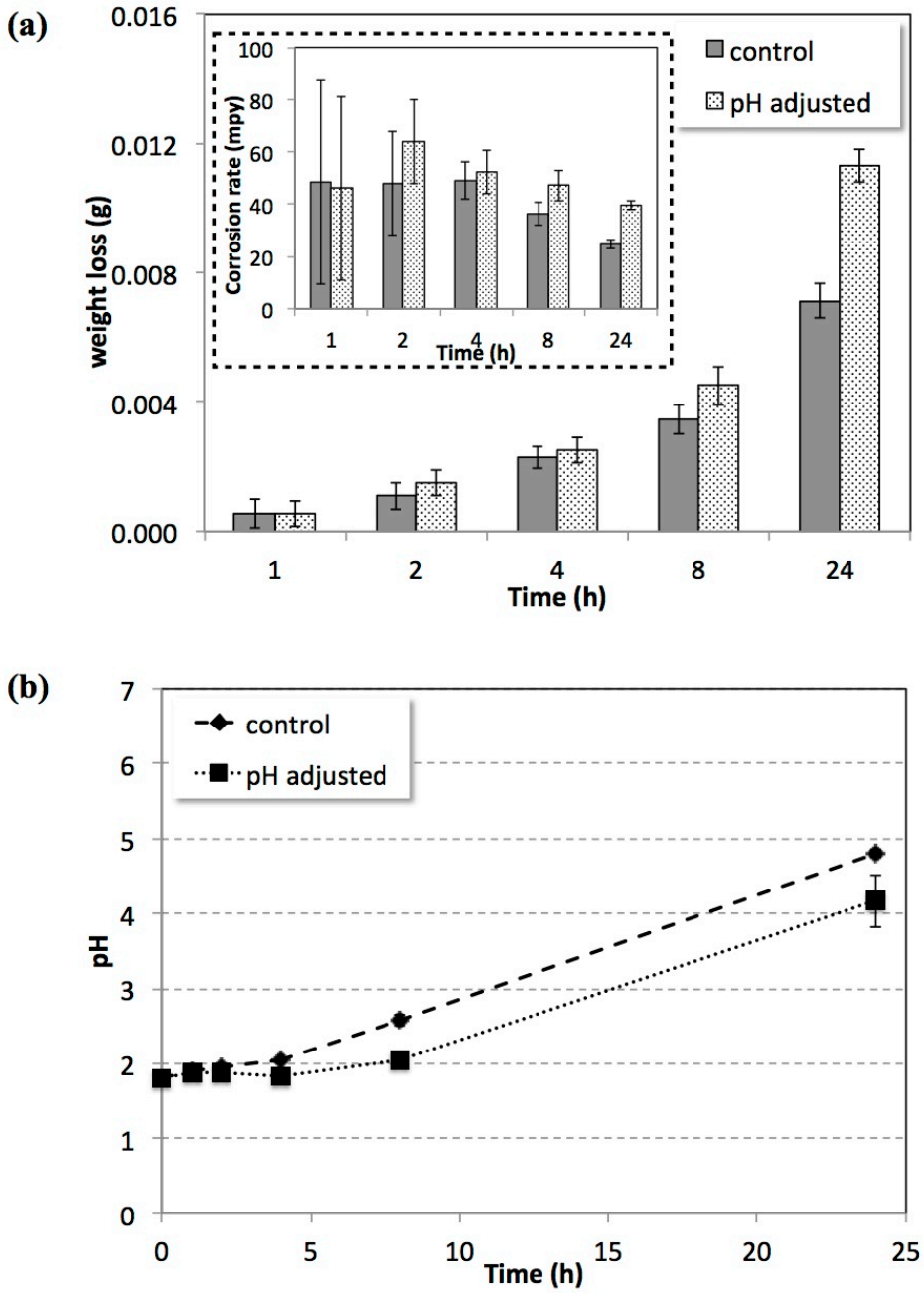

Figure 4.24 (a). The weight loss of CS C1010 coupons exposed in control and pH adjusted systems for 24 h are shown. The errors shown for each data point is the standard deviation obtained from at least eight sets of measurements. The insert is the corrosion rate of CS C1010 coupons exposed in control and pH adjusted systems for 24 h. The errors shown for each data point is the standard deviation obtained from at least eight sets of measurements. (b). The pH change of control and pH adjusted systems for 24 h are shown.

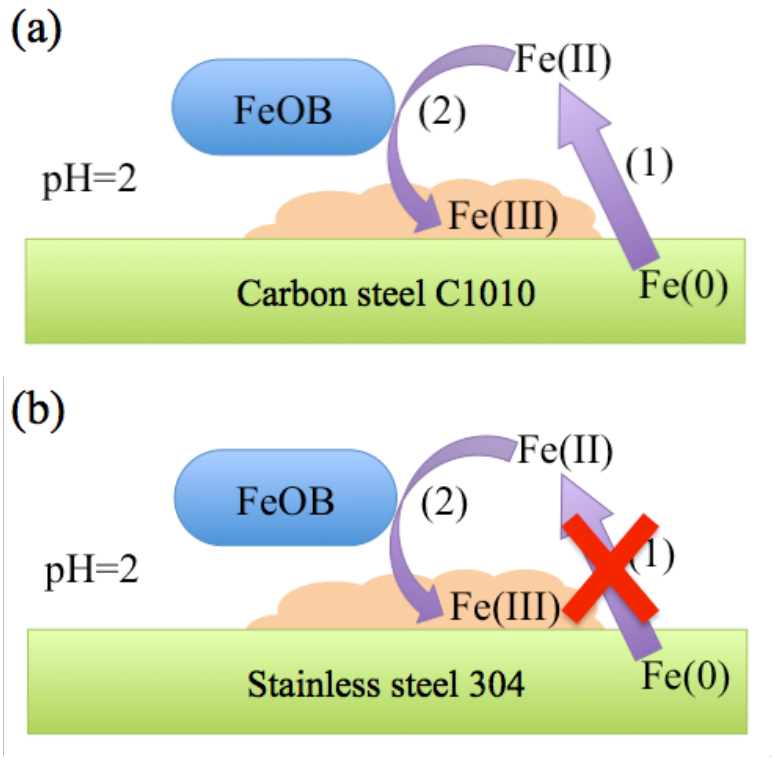

Figure 4.25 Schematic of the iron (Fe) reaction pathways of *A. ferrooxidans* with (a) Carbon steel C1010 and (b) Stainless steel 304.

The presence of *A. ferrooxidans* cells in the medium accelerated the oxidation of Fe(II) to Fe(III) by Reaction (11) in place of Reaction (9), dramatically increased the reaction rate of the rate-limiting step as compared to cell-free systems. As a consequence, for systems with CS coupons, the reactions forms a iron oxidizing cycle: Firstly, the low pH environment could continuously consumed protons to oxidize Fe(0) to Fe(II) by Reaction (8) and transfer them to the bulk medium as the energy source for *A. ferrooxidans* cells. Then cells converted Fe(II) to Fe(III) for their survival by Reaction (11). Afterwards, as Fe(III) accumulated in the medium, $Fe(OH)_3$ precipitation formed and more protons produced by Reaction (10) to maintain the system pH at ~2, and Reaction (8) could be continued by the protons produced in Reaction (10). However, for SS, since SS 304 consists of an austenitic matrix and possesses good corrosion resistance in most atmospheres and oxidizing acids, pH ~2 sulfuric acid can not attack it [127], neither can iron-oxidizing bacteria alone [128]. Additional lab test results (data not shown) showed that at room temperature (~ 23°C), SS 304 coupons had noble corrosion resistance towards sulfuric acid, no apparent change of SS 304 coupons was noticed until the sulfuric acid concentration raised up to 0.5 mol/L, i.e. pH ~0. In this case, no Fe(0) oxidation occurred for SS 304, thus no additional Fe(II) to the cell medium. After Fe(II) in cell medium depleted, *A. ferrooxidans* cells died out due to the deficiency of energy source.

For systems with CS coupons, a significant number of cells (~ 0.75×10^7 cells/mL) lived in bulk medium rather than attached onto the CS coupon surface for survival (Figure 4.21(g)). The relatively high concentration of cells in bulk medium implied that *A. ferrooxidans* cells could simply utilize Fe(II), in the bulk medium,

resulted from dissolution of iron (Fe(0)) by the acidic condition to survive. This non-contact surviving mechanism is different from the direct contact mechanism [129], in which cells need to attach (direct contact) to the substrate surface with the assistant of extracellular polymeric substances (EPS) to conduct Fe(II) oxidization.

4.4.6 CS coupon corrosion characterization

Corrosion occurred after CS coupons submerged in all three systems. Figure 4.26(a) shows the topography of CS coupons (from left) prior to submersion, in control, in cell medium, in medium with cells for 7 d. The prior to submersion coupon was shinny and smooth, while the one in the control system was covered by a black thin layer that would probably be composed by Fe(II). The one in the cell medium system was similar to that of in the control system, but, instead of a black thin layer, it was covered by a light brownish deposit, which could probably be composed of Fe(III). The one in the cell medium with cells was covered by a thick brownish layer, likely Fe(III) precipitations, similar deposit was found on the SS coupon in cell medium with cells as, which could mainly be from the medium when Fe(II) was converted to Fe(III) by metabolism of *A. ferrooxidans* cells.

After removing all the precipitations and corrosion products on the coupons, pitting corrosion was detected on CS coupon surfaces after the coupons had been submerged in medium with *A. ferrooxidans* for 7 days. An optical microscope image and its color converted 3-D image of typical CS coupon after 7 days of submersion were presented in Figure 4.26(b)-(c). The diameter of the pits was in a range of 450~500 μm, and the depth ranged from 60~170 μm. As shown in Figure 4.26(c), other than the two

larger pits, the surface had countless small dents with a depth ranging from 5~20 μm, which caused the increase in surface roughness (Table. 4.9).

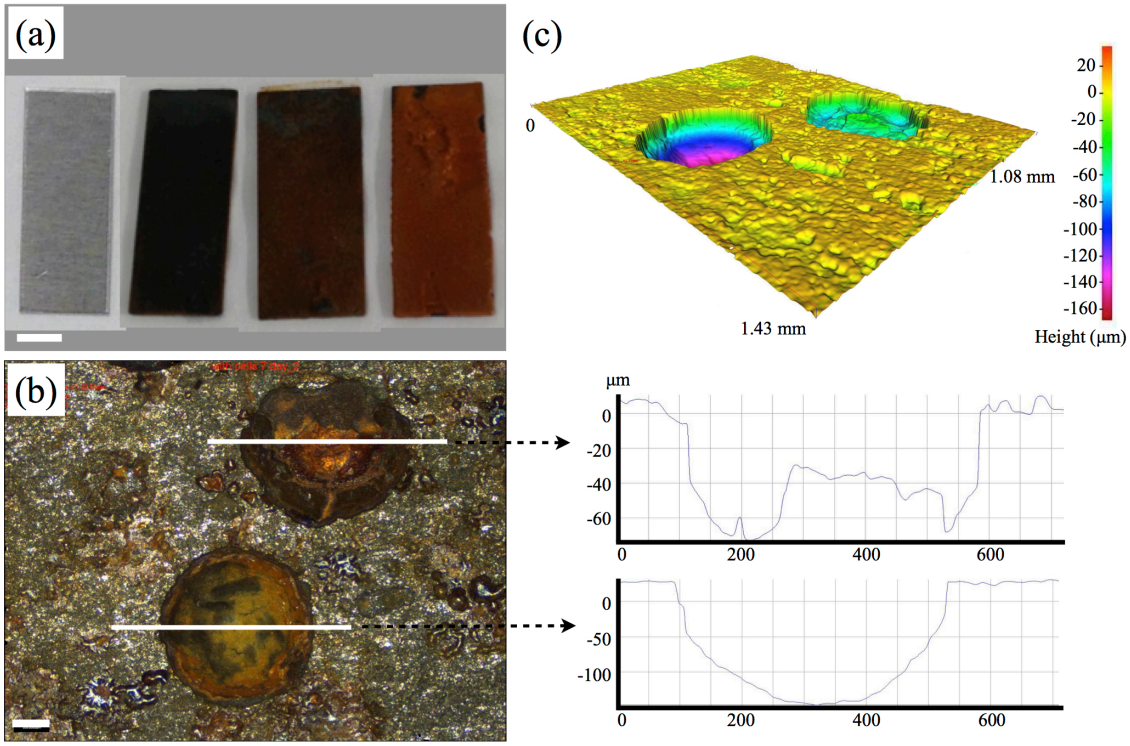

Figure 4.26 (a). The digital images of CS coupons (from left) prior to run, in control, in cell medium, and with cells after 7 days, respectively, are shown. Scale bar represents 5 mm. (b). An optical microscope image of typical pitting corrosion of CS coupon in with cells system after 7 d is presented. Scale bar represents 100 μm. The inserts are the cross sections of the two main pits on the coupon surface. (c). The color converted 3-D image of (b) is shown.

Two possible mechanisms might result in the pitting corrosion. The first is the crevice corrosion mechanism: oxygen concentrated zones can be created by the dense $Fe(OH)_3$ precipitation layer, which was formed by the metabolism of *A. ferrooxidans* cells. The precipitation layer and oxygen zones can initiate crevice corrosion on the CS coupon surface [26]. In such a case, the CS surface beneath a dense $Fe(OH)_3$ precipitation layer could form small anodic sites, as oxygen reacted with H_2O and accepted electrons from Fe(0) to form hydroxyl, which combined with Fe(III) to form the insoluble $Fe(OH)_3$ and lower the pH. At the anodic site, Fe(0) oxidization continued, ultimately formed a pit on the CS coupon surface. The other possible mechanism is related to the attachment of *A. ferrooxidans* cells and iron-oxidizing activity. Since the CS coupon surface was not completely smooth, cells could attach into the valleys of some of the rough spots. As cells accelerated the conversion of Fe(II) to Fe(III) by Reaction (11), the valley of the rough spot developed into a pit [129]. Meanwhile, $Fe(OH)_3$ precipitation formed and filled in the pit, created a small local environment that allowed the cycle of Reactions (8), (10), and (11). Due to the low pH and high oxidation rate of Fe(II), the corrosion rate in the pit could be higher than that on a smooth/uniform surface. Eventually, a wide and deep pit could form under the precipitation layer. One or both of these two mechanisms might cause the pit formation; more study is needed to further elucidate the corrosion mechanism of CS C1010 in the presence of *A. ferrooxidans*.

4.4.7 Summary

In this part of study, we evaluated corrosion behaviors of CS C1010 and SS 304 in the presence of an iron-oxidizing bacterium: *A. ferrooxidans*. Severe corrosion was

found on CS C1010 associated with *A. ferrooxidans.* The corrosion rate was ~ 3.4 to 6 x as compared to those in systems without *A. ferrooxidans*. A potential cause could be the microbial metabolism, which oxidized Fe(II) to Fe(III) faster than that in the control system. However, SS showed a good corrosion resistance to pH ~2 acidic conditions and even the system with *A. ferrooxidans* cells. As pH ~2 sulfuric acid/water could not convert Fe(0) to Fe(II), *A. ferrooxidans* cells were not able to obtain enough energy source (Fe(II)) to survive. In addition, the results from this part of study showed that *A. ferrooxidans* cells did not need to attach onto CS surface to cause corrosion; accelerated corrosion for CS could result by oxidizing Fe(II) in the bulk medium, from oxidizing Fe(0) under acidic condition, to Fe(III) and maintaining the system pH at ~ 2. While uniform corrosion was expected, pitting corrosion was found on the CS coupon surface, which could be caused by crevice corrosion or the localized environment due to the attached cells. More studies are needed to elucidate the accelerated corrosion of CS C1010 in the presence of *A. ferrooxidans*.

4.5 Corrosion evaluations of aluminum alloy (Al 2024) in the presence of *Trichoderma reesei* and *Aspergillus niger*

This part provides the results and discussion about corrosion evaluation of aluminum alloy (Al 2024) in the presence of *Trichoderma reesei* and *Aspergillus niger*. The subsections include fungal attachment, corrosion evaluation, and summary.

4.5.1 Fungal attachment

After 7 days of exposure in both with *T. reesei* and with *A. niger* systems, Al coupons were collected and the fungal attachment was evaluated. As shown in Figure 4.27, on the Al coupon surfaces, only auto-florescent machined lines could be detected; no fungal attachment was found, indicating that *T. reesei* or *A. niger* fungal biofilm could not firmly attach onto Al coupon surfaces. Similar results of fungal attachment were discovered in the flow chamber system.

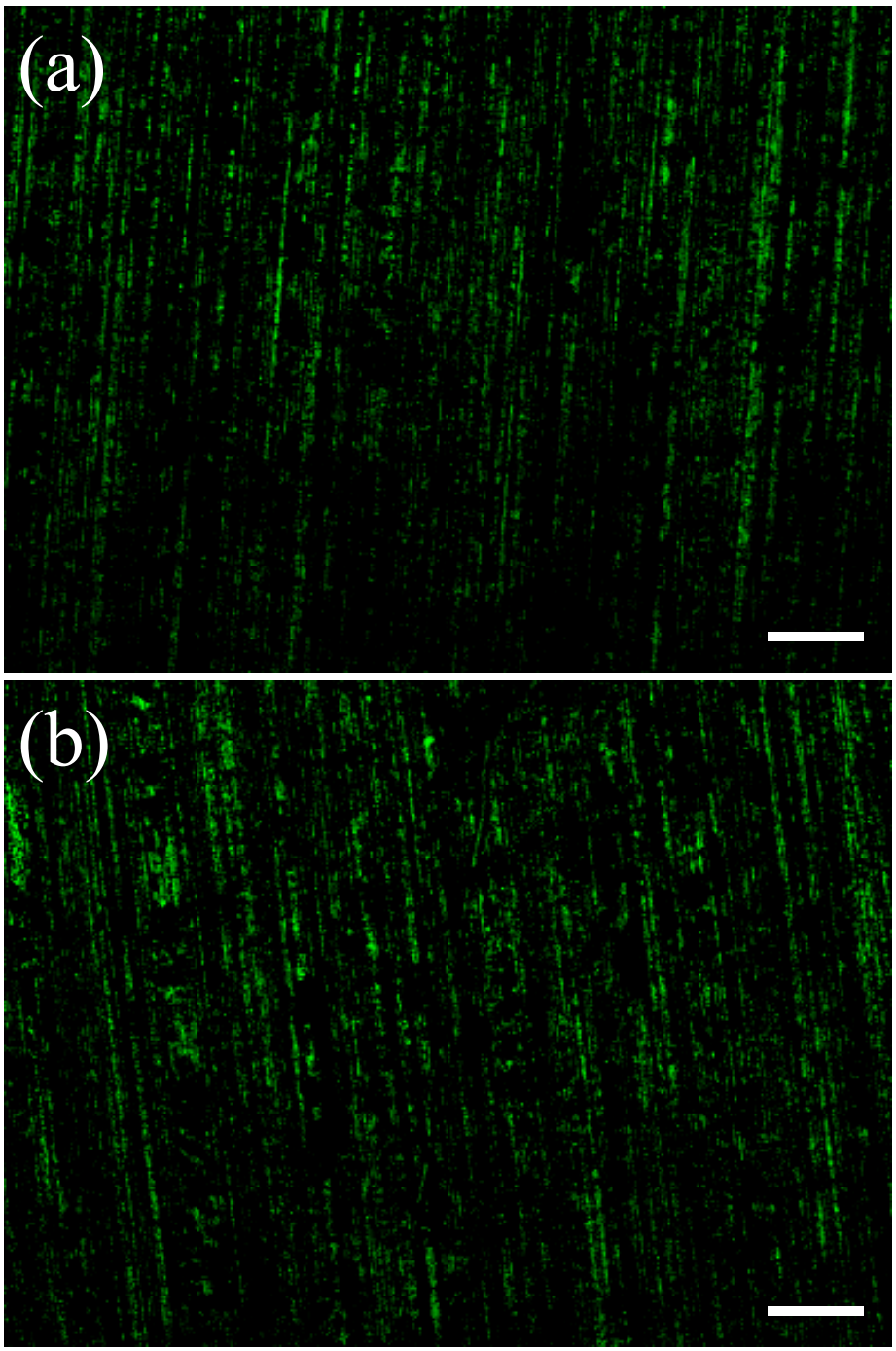

Figure 4.27 (a) The fluorescent confocal image of Al 2024 surface in with *T. reesei* system after 7 days, after rinsed with DI water. Scale bars represent 100 μm. (b). The fluorescent confocal image of Al 2024 surface in with *A. niger* system after 7 days, after rinsed with DI water. Scale bars represent 100 μm.

4.5.2 Corrosion evaluation

Corrosion behaviors of Al coupons in the control (pH 3 and 5), and in the medium with fungal cells (pH 3 and 5) for 7 and 14 d, respectively, were briefly assessed by the weight loss method (ASTM D2688-05), and the corrosion rates were calculated accordingly. In both the control and the *T. reesei* systems under pH 5 conditions, no weight loss was found for Al coupons ($p=0.50$ for 7 d and $p=0.67$ for 14 d, between coupons in control and *T. reesei* systems). Accordingly, the corrosion rates of Al coupons were ~ 0.

Similar results were obtained in both the control and the *T. reesei* systems under pH 3 conditions. The weight loss and corrosion rates for Al coupons in both the control and the *T. reesei* systems were all ~ 0 ($p=0.45$ for 7 d and $p=0.34$ for 14 d, between coupons in control and *T. reesei* systems). Results indicated that *T. reesei* had no corrosion effect on Al 2024 at either pH 5 or 3 conditions.

For the *A. niger* system, Al coupon corrosion habeviors were similar to that of *T. reesei*. In both the control and the *A. niger* systems, with pH 5 ($p=0.51$ for 7 d and $p=0.90$ for 14 d, between coupons in control and *T. reesei* systems) or pH 3 ($p=0.30$ for 7 d and $p=0.75$ for 14 d, between coupons in control and *T. reesei* systems) conditions, no corrosion was detected.

To verify the pH effect on Al coupon corrosion, a series of pH (water/H_2SO_4, pH 2, 3, 4, 5, 6, and 7) solutions were utilized to study the Al coupon weight loss and corrosion rates. Al coupons were exposed to acid solutions for 7 and 14 d. The weight loss of Al coupons in the pH 2 solution was ~ 0.001 g after 7 and 14 d. While in other (pH 3, 4, 5, 6, and 7) solutions, no weight loss was detected ($p=0.52$ for 7 d and $p=0.74$

for 14 d). Accordingly, the corrosion rates in the pH 2 solution was ~ 1.2 mpy during 7 days, and ~ 0.6 mpy during 14 days.

4.5.3 Summary

In this part of the study, we evaluated the *T. reesei* and *A. niger* attachments and corrosion behaviors on Al 2024 in the presence of these two fungi. Neither *T. reesei* nor *A. niger* can firmly attach onto the Al coupon surfaces to form a biofilm. Meanwhile, no corrosion was detected for the Al coupons in the control, the *T. reesei* or the *A. niger* systems. Further pH effect study showed that Al 2024 could not be corroded in pH 3, 4, 5, 6, or 7, but in the pH 2 acid solution. The results indicated that for Al coupons with fungal system, the pH was not low enough for the Al to be corroded. Fungal cell metabolism could not influence Al coupons due to the low cell attachment and the relatively short exposure time (14 d).

CHAPTER V

CONCLUDING REMARKS

This work presents the effects of microbial attachment and biofilm formation on microbiologically influenced corrosion (MIC).

In the first part of this study, the initial attachment of three bacteria, *Pseudomonas aeruginosa*, *Escherichia coli* and *Pseudomonas putida*, on two substrates, glass and octadecyltrichlorosilane (OTS) modified glass, was examined in flow chambers. The flow chambers were designed and operated to mimic slow moving water bodies and minimize the gravitational settlement of cells. The hydrophobicity of bacterial surfaces was evaluated by partitioning of cells to the water-hexadecane interface and the liquid contact angles on cell layers collected on filter papers. On the more hydrophilic glass surface, the attachment trend was found to be *E. coli* > *P. putida* > *P. aeruginosa*, while the opposite trend was observed on the hydrophobic, OTS modified surface. The attachment trend on glass could be explained by the secondary minima and energy barriers as predicted by the extended Derjaguin-Landau-Verwey-Overbeek (XDLVO) theory. The much higher attachments of *P. aeruginosa* and *P. putida* on the OTS-modified substrate, on the other hand, suggested that these cells could overcome the energy barrier between the primary and secondary minima of interaction energy to become attached to the primary minima. The extent of primary minimum

attachment appeared to correlate with the scale of the energy barrier, with higher attachments in the bacteria-substrate combinations of lower energy barriers. This part of the study generated some insights into the effects of cell and substrate surface properties on initial bacterial attachment.

In the second part of this study, four bacteria: *Staphylococcus epidermidis*, *Pseudomonas aeruginosa*, *Pseudomonas putida*, and *Escherichia coli*, were examined for their attachment to glass and OTS modified glass under different shears. Polystyrene particles were used to verify that their shear dependent attachment on glass and OTS could be interpreted using the analysis of the XDLVO theory. In particular, the critical shear force ($F_{c\text{-}shear}$) could correlate with the maximum attractive force (F_{MAX}^{XDLVO}) towards the secondary energy minimum as $F_{c-shear} = c \cdot F_{MAX}^{XDLVO}$. For these particles, c of ~ 1 was obtained; the value was within the coefficient range (0.1 – 1) of substances sliding over glass. For *S. epidermidis, E. coli* and *P. aeruginosa* on glass, c was 0.3, < 0.6 and 0.2, respectively. When considering potential protein adsorption on OTS during bacterial attachment, c of these species on OTS was slightly above 1. A greatly enhanced attachment of *P. aeruginosa* on OTS was also observed, probably due to the presence of flagella. For *P. putida*, the attachment first decreased slightly or maintained with shear and then increased. Such behaviors were probably caused by the increased secretion of extracellular polymeric substances (EPS) at higher shears by *P. putida*. The results from this part of study suggested that, without complications from surface features/EPS, the analysis based on the XDLVO theory could provide a basis for understanding shear effect on initial bacterial attachment.

The third part of the study intends to evaluate how the early stages of biofilm formation affect the MIC of carbon steel and aluminum alloy. Flow chamber systems were utilized to allow the *in situ* monitoring of biofilm development and its influences on corrosion. In this part of the study, aluminum films, aluminum alloy (Al 3003 H14) coupons and carbon steel (CS C1010) coupons were used, along with two common bacterial strains, *Pseudomonas aeruginosa* PAO1 and *Escherichia coli*. Under our experimental conditions, the Al films and Al 3003 H14 coupons showed no corrosion in the presence of these two bacterial biofilms. However, for CS coupons, similar corrosion rates were found for control and with the *E. coli* biofilm, while a lower corrosion rate was observed for coupons covered by the PAO1 biofilm. The inhibited corrosion of CS in the presence of the PAO1 biofilm was likely caused by the oxygen deficient environment and the Fe(II) layer generated by the anaerobic respiration of the PAO1 cells.

In the fourth part of this study, the corrosion behaviors of CS C1010 and SS 304 in the presence of iron-oxidizing bacteria: *Acidithiobacillus ferrooxidans* was examined. Results showed that, due to the extremely high oxidizing rate of Fe(II) to Fe(III), *A. ferrooxidans* cells can accelerate CS corrosion at a rate of 3 to 6 times faster than that without *A. ferrooxidans* present. SS 304 showed a good corrosion resistance to a pH ~2 solution of sulfuric acid, under which converting Fe(II) to Fe(III) from SS was found to be infeasible. *A. ferrooxidans* cells could not survive due to the deficiency of Fe(II) as the energy source. For the CS coupons, *A. ferrooxidans* cells accelerated corrosion by oxidizing the Fe(II) to Fe(III) and maintaining the system pH at ~ 2 to retain the reaction cycle. Pitting corrosion was also found on CS coupons. Two possible mechanisms were

proposed: crevice corrosion or localized corrosion resulting from the extreme environment caused by attached cells.

In the last part, the corrosion behaviors of Al 2024 in the presence of *Trichoderma reesei* and *Aspergillus niger* were evaluated. Static vessel systems were utilized to control and maintain the system pH. Results showed that *T. reesei* or *A. niger* could not firmly attach to Al coupon surfaces in an aqueous environment. The corrosion evaluation showed that under the pH 3 and 5 conditions, *T. reesei* and *A. niger* cannot corrode Al 2024. It could be due to the good corrosion resistance of the Al coupon to the pH 3 and 5 acid solutions, or that fungal cell metabolism could not influence the Al coupon due to the low cell attachment.

REFERENCES

[1] Gerhardus H. Koch, Michiel P.H. Brongers, Neil G. Thompson, Y. Paul Virmani, J.H. Payer, NACE International, Houston, 2001.

[2] Brenda J. Little, J.S. Lee, Microbilogically influenced corrosion, John Wiley & Sons, Inc., New Jersy, 2007.

[3] H.-C. Flemming, Microbial Deterioration of Material, Springer, Heidelberg, 1996.

[4] G.H. Booth, Journal of Applied Microbiology, 27 (1964) 174-181.

[5] R. Zuo, Applied Microbiology and Biotechnology, 76 (2007) 1245-1253.

[6] Brenda J. Little, Patricia Wagner, F. Mansfeld, Electrochimica Acta, 37 (1992) 2185-2194.

[7] Sonia Bayoudh, Ali Othmane, Laurence Mora, H.B. Ouada, Colloids and Surfaces B: Biointerfaces, 73 (2009) 1-9.

[8] E.J.W. Verwey, J.T.G. Overbeek, Elsevier Publishing Company, Inc., Amsterdam, 1948.

[9] B. V. Derjaguin, L. Landau, Acta Physicochim URSS, 14 (1941) 633-662.

[10] C.J.v. Oss, Colloids and Surfaces B: Biointerfaces, 5 (1995) 91-110.

[11] C.J. van Oss, R.J. Good, M.K. Chaudhury, Journal of Colloid and Interface Science, 111 (1986) 378-390.

[12] Aeri Park, Heon-Ho Jeong, Jintae Lee, Keun Pil Kim, C.-S. Lee, BioChip Journal, 5 (2011) 236-241.

[13] M. Reza Nejadnik, Henny C. van der Mei, Henk J. Busscher, W. Norde, Applied and Environmental Microbiology, 74 (2008) 916-919.

[14] Astrid Roosjen, Niels P. Boks, Henny C. van der Mei, Henk J. Busscher, W. Norde, Colloids and Surfaces B: Biointerfaces, 46 (2005) 1-6.

[15] Wendy E. Thomas, Elena Trintchina, Manu Forero, Viola Vogel, E.V. Sokurenko, Cell, 109 (2002) 913-923.

[16] Z.J. Li, N. Mohamed, J.M. Ross, Biotechnology Progress, 16 (2000) 1086-1090.

[17] N. Mohamed, T.R.R. Jr., J.M. Ross, Biotechnology and Bioengineering, 68 (2000) 628-636.

[18] Donald E. Brooks, T.J. Trust, Journal of General Microbiology, 129 (1983) 3661-3669.

[19] Hua Wang, Maysam Sodagari, Yajie Chen, Xin He, Bi-min Zhang Newby, L.-K. Ju, Colloids and Surfaces B: Biointerfaces, 87 (2011) 415-422.

[20] Héctor A. Videla, L.K. Herrera, International Microbiology, 8 (2005) 169-180.

[21] Congmin Xu, Yaoheng Zhang, Guangxu Cheng, W. Zhu, Materials Science and Engineering A, 443 (2007) 235-241.

[22] G. Kobrin, Materials Performance, 15 (1976) 38-42.

[23] Terunobu Maeda, Atsunori Negishi, Hiromi Komoto, Yuko Oshima, Kazuo Kamimura, T. Sugio, Journal of Bioscience and Bioengineering, 88 (1999) 300-305.

[24] Donovan P. Kelly, A.P. Wood, International Journal of Systematic and Evolutionary Microbiology, 50 (2000) 511-516.

[25] Denise Bevilaqua, Heloisa A. Acciari, Fabiana A. Arena, Assis V. Benedetti, Cecílio S. Fugivara, Germano Tremiliosi Filho, O.G. Júnior, Minerals Engineering, 22 (2009) 254-262.

[26] David Starosvetsky, Robert Armon, Josef Yahalom, J. Starosvetsky, International Biodeterioration and Biodegradation, 47 (2001) 79-87.

[27] B. J. Little, P. Wagner, Materials Performance, 36 (1997) 40-44.

[28] R.E. Tatnall, Materials Performance, 20 (1981) 32-38.

[29] V. F. Smirnov, D. V. Belov, T. N. Sokolova, O. V. Kuzina, V.R. Kartashov, Applied Biochemistry and Microbiology, 44 (2008) 192-196.

[30] D. V. Belov, T. N. Sokolova, V. F. Smirnov, O. V. Kuzina, L. V. Kostyukova, V.R. Kartashov, Protection of Metals, 44 (2008) 737-742.

[31] W.A. Ferrando, Journal of Materials Engineering, 11 (1989) 299-313.

[32] Patricia Wagner, B. Little, Materials Selection and Design, 32 (1993) 65-68.

[33] Flore Laurent, Brigitte Grosgogeat, Lucien Reclaru, Francis Dalard, M. Lissac, Biomaterials, 22 (2001) 2273-2282.

[34] Andrew Scardino, Rocky De Nys, Odette Ison, Wayne O'Connor, P. Steinberg, Biofouling, 19 (2003) 221-230.

[35] Nolan T. Flynn, Thanh Nga T. Tran, Michiel J. Cima, R. Langer, Langmuir, 19 (2003) 10909-10915.

[36] Teresa R. Scheuerman, Anne K. Camper, M.A. Hamilton, Journal of Colloid and Interface Science, 208 (1998) 23-33.

[37] Tao Liu, Lihua Dong, Tong Liu, Y. Yin, Electrochimica Acta, 55 (2010) 5281-5285.

[38] C.J.v. Oss, Colloids and Surfaces A: Physicochemical and Engineering Aspects, 78 (1993) 1-49.

[39] A. Grabbe, R.G. Horn, Journal of Colloid and Interface Science, 157 (1993) 375-383.

[40] D.J. Shaw, Introduction to Colloid and Surface Chemistry, Butterworths, London, 1980.

[41] Y. Liu, Q. Zhao, Biophysical Chemistry, 117 (2005) 39-45.

[42] C.J.v. Oss, Interfacial Forces in Aqueous Media, Marcel Dekker, New York, 1994.

[43] K.C. Marshall, J.A. Breznak, G.B. Calleja, G.A. Mcfeters, P.R. Rutter, Microbial Adhesion and Aggregation, Springer-Verlag, New York, 1984.

[44] J.M. Meinders, H.C. van der Mei, H.J. Busscher, Journal of Colloid and Interface Science, 176 (1995) 329-341.

[45] Mark C. M. van Loosdrecht, Willem Norde, Johannes Lyklema, A.J.B. Zehnder, Aquatic Science, 52 (1990) 103-114.

[46] Sharron McEldowney, M. Fletcher, Applied and Environmental Microbiology, 52 (1986) 460-465.

[47] J. Azeredo, J. Visser, R. Oliveira, Colloids and Surfaces B: Biointerfaces, 14 (1999) 141-148.

[48] S. C. Dexter, J. J. D. Sullivan, I. J. Williams, S.W. Watson, Applied Microbiology, 30 (1975) 298-308.

[49] S.C. Dexter, Journal of Colloid and Interface Science, 70 (1979) 346-354.

[50] Matthew Whitfield, Tia Ghose, W.E. Thomas, Biophysical Journal, 99 (2010) 2470-2478.

[51] Marc B. Habash, Henny C. van der Mei, Gregor Reid, H.J. Busscher, Microbiology, 143 (1997) 2569-2574.

[52] Matthew S. Shive, Sakeena M. Hasan, J.M. Anderson, Journal of Biomedical Materials Research, 46 (1999) 511-519.

[53] Henk J. Busscher, H.C.v.d. Mei, Clinical Microbiology Reviews, 19 (2006) 127-141.

[54] Akhila Raya, Maysam Sodagari, Neissa M. Pinzon, Xin He, Bi-min Zhang Newby, L.-K. Ju, Environmental Science and Pollution Research, 17 (2010) 1529-1538.

[55] Niels P. Boks, Willem Norde, H.C.v.d. Mei, H.J. Busscher, Microbiology, 154 (2008) 3122-3133.

[56] M. Katsikogianni, Y.F. Missirlis, European Cells and Materials, 8 (2004) 37-57.

[57] C. K. Stover, X. Q. Pham, A. L. Erwin, S. D. Mizoguchi, P. Warrener, M. J. Hickey, F.S. L. Brinkman, W. O. Hufnagle, D. J. Kowalik, M. Lagrou, R. L. Garber, L. Goltry, E. Tolentino, S. Westbrock-Wadman, Y. Yuan, L. L. Brody, S. N. Coulter, K. R. Folger, A. Kas, K. Larbig, R. Lim, K. Smith, D. Spencer, G. K.-S. Wong, Z. Wu, I. T. Paulsen, J. Reizer, M. H. Saier, R. E. W. Hancock, S. Lory, M.V. Olson, Nature, 406 (2000) 959-964.

[58] G.A. O'Toole, R. Kolter, Molecular Microbiology, 30 (1998) 295-304.

[59] Markus Michael Müller, Barbara Hörmann, Christoph Syldatk, R. Hausmann, Applied Microbiology and Biotechnology, 87 (2010) 167-174.

[60] R. Bentley, R. Meganathan, Microbiological Reviews, 46 (1982) 241-280.

[61] Leonardo De La Fuente, Emilie Montanes, Yizhi Meng, Yaxin Li, Thomas J. Burr, H. C. Hoch, M. Wu, Applied and Environmental Microbiology, 73 (2007) 2690-2696.

[62] H.C. Berg, E. coli in Motion, Springer-Verlag, New York, USA, 2004.

[63] K. E. Nelson, C. Weinel, I. T. Paulsen, R. J. Dodson, H. Hilbert, V. A. P. Martins dos Santos, D. E. Fouts, S. R. Gill, M. Pop, M. Holmes, L. Brinkac, M. Beanan, R. T. DeBoy, S. Daugherty, J. Kolonay, R. Madupu, W. Nelson, O. White, J. Peterson, H. Khouri, I. Hance, P. Chris Lee, E. Holtzapple, D. Scanlan, K. Tran, A. Moazzez, T. Utterback, M. Rizzo, K. Lee, D. Kosack, D. Moestl, H. Wedler, J. Lauber, D. Stjepandic, J. Hoheisel, M. Straetz, S. Heim, C. Kiewitz, J. Eisen, K. N. Timmis, A. Düsterhöft, B. Tümmler, C.M. Fraser, Environmental Microbiology, 4 (2002) 799-808.

[64] Eun Na Choi, Min Chul Cho, Youngsoo Kim, Chi-Kyung Kim, K. Lee, Microbiology, 149 (2003) 795-805.

[65] Cuong Vuong, Jovanka M. Voyich, Elizabeth R. Fischer, Kevin R. Braughton, Adeline R. Whitney, Frank R. DeLeo, M. Otto, Cellular Microbiology, 6 (2004) 269-275.

[66] J.T. Parisi, Microbiological Reviews, 49 (1985) 126-139.

[67] Rey-Chang Chang, Shu-Jen Chou, J.-F. Shaw, Journal of Agricultural and Food Chemistry, 49 (2001) 2619-2622.

[68] William W. Leathen, Norma A. Kinsel, S. S. A. Braley, Journal of Bacteriology, 72 (1956) 700-704.

[69] A.K. Lee, D.K. Newman, Applied Microbiology and Biotechnology, 62 (2003) 134-139.

[70] K. Konhauser, Introduction to Geomicrobiology, Blackwell, Malden, MA, USA, 2007.

[71] D. T. Lacey, F. Lawson, Biotechnology and Bioengineering, 12 (1970) 29-50.

[72] Diego Martinez, Randy M Berka, Bernard Henrissat, Markku Saloheimo, Mikko Arvas, Scott E Baker, Jarod Chapman, Olga Chertkov, Pedro M Coutinho, Dan Cullen, Etienne G J Danchin, Igor V Grigoriev, Paul Harris, Melissa Jackson, Christian P Kubicek, Cliff S Han, Isaac Ho, Luis F Larrondo, Alfredo Lopez de Leon, Jon K Magnuson, Sandy Merino, Monica Misra, Beth Nelson, Nicholas Putnam, Barbara Robbertse, Asaf A Salamov, Monika Schmoll, Astrid Terry, N. Thayer., Ann Westerholm-Parvinen, Conrad L Schoch, Jian Yao, Ravi Barabote, Mary Anne Nelson, Chris Detter, David Bruce, Cheryl R Kuske, Gary Xie, Paul Richardson, Daniel S Rokhsar, Susan M Lucas, Edward M Rubin, Nigel Dunn-Coleman, Michael Ward, T.S. Brettin, Nature Biotechnology, 26 (2008) 553-560.

[73] S. Kishen Tangnu, Harvey W. Blanch, C.R. Wilke, Biotechnology and Bioengineering, 23 (1981) 1837-1849.

[74] Herman J Pel, Johannes H de Winde, David B Archer, Paul S Dyer, Gerald Hofmann, Peter J Schaap, Geoffrey Turner, Ronald P de Vries, Richard Albang, Kaj Albermann, Mikael R Andersen, Jannick D Bendtsen, Jacques A E Benen, Marco van den Berg, Stefaan Breestraat, Mark X Caddick, Roland Contreras, Michael Cornell, Pedro M Coutinho, Etienne G J Danchin, Alfons J M Debets, Peter Dekker, Piet W M van Dijck, Alard van Dijk, Lubbert Dijkhuizen, Arnold J M Driessen, Christophe d'Enfert, Steven Geysens, Coenie Goosen, Gert S P Groot, Piet W J de Groot, Thomas Guillemette, Bernard Henrissat, Marga Herweijer, Johannes P T W van den Hombergh, Cees A M J J van den Hondel, Rene T J M van der Heijden, Rachel M van der Kaaij, Frans M Klis, Harrie J Kools, Christian P Kubicek, Patricia A van Kuyk, Jürgen Lauber, Xin Lu, Marc J E C van der Maarel, Rogier Meulenberg, Hildegard Menke, Martin A Mortimer, Jens Nielsen, Stephen G Oliver, Maurien Olsthoorn, Karoly Pal, Noël N M E van Peij, Arthur F J Ram, Ursula Rinas, Johannes A Roubos, Cees M J Sagt, Monika Schmoll, Jibin Sun, David Ussery, Janos Varga, Wouter Vervecken, Peter J J van de

Vondervoort, Holger Wedler, Han A B Wösten, An-Ping Zeng, Albert J J van Ooyen, Jaap Visser, H. Stam, Nature Biotechnology, 25 (2007) 221-231.

[75] Eimutis Juzeliunas, Rimantas Ramanauskas, Albinas Lugauskas, Konstantinas Leinartas, Meilute Samuleviciene, Aloyzas Sudavicius, R. Juskenas, Corrosion Science, 49 (2007) 4098-4112.

[76] Eimutis Juzeliunas, Rimantas Ramanauskas, Albinas Lugauskas, Meilute Samulevičiene, K. Leinartas, Electrochemistry Communications, 7 (2005) 305-311.

[77] J.M. Meinders, H.C. vanderMei, H.J. Busscher, Journal of Colloid and Interface Science, 176 (1995) 329-341.

[78] Jennifer W. McClaine, R.M. Ford, Biotechnology and Bioengineering, 78 (2002) 179-189.

[79] J. Pawley, Handbook of Biological Confocal Microscopy, Springer, Madison, WI, USA, 2006.

[80] T.J. Fellers, M.W. Davidson, National High Magnetic Field Laboratory, Olympus Fluoview Resource Center, 2013.

[81] Hartmuth Schroettner, Mario Schmied, S. Scherer, Microchim Acta, 155 (2006) 279-284.

[82] P.J.D. Pablo, Methods in Molecular Biology, 783 (2011) 197-212.

[83] E. Meyer, Progress in Surface Science, 41 (1992) 3-49.

[84] G. Binning, C.F. Quate, C. Gerber, Physical Review Letters, 56 (1986) 930-934.

[85] ASTM, Standard test method for corrosivity of water in the absence of heat transfer (weight loss method), D2688-05, 2005.

[86] Melvin P. Silverman, D.G. Lundgren, Journal of Bacteriology, 77 (1959) 642-647.

[87] Manuel Simões, Lúcia C. Simões, Sara Cleto, Maria O. Pereira, M.J. Vieira, International Journal of Food Microbiology, 121 (2008) 335-341.

[88] H.J. Busscher, M.-N. Bellon-Fontaine, N. Mozes, H.C. van der Mei, J.Sjollema, A.J. Léonard, P.G. Rouxhet, O. Cerf, Journal of Microbiological Methods, 12 (1990) 101-115.

[89] K.J. Bundy, L.G. Harris, B.A. Rahn, R.G. Richards, Cell Biology International, 25 (2001) 289-307.

[90] M. Hermansson, Colloids and Surfaces B: Biointerfaces, 14 (1999) 105-119.

[91] A. Zita, M. Hermansson, Applied and Environmental Microbiology, 63 (1997) 1168-1170.

[92] H.C. van der Mei, A.H. Weerkamp, H.J. Busscher, FEMS Microbiology Letters, 40 (1987) 15-19.

[93] Jürgen Feldner, Wolfgang Bredt, I. Kahane, Journal of Bacteriology, 153 (1983) 1-5.

[94] M. Hermansson, S. Kjelleberg, T.K. Korhonen, T. Stenstrom, Arch Microbiol, 131 (1982) 308-312.

[95] Cristina Gómez-Suárez, Henk J. Busscher, H.C.v.d. Mei, Applied and Environmental Microbiology, 67 (2001) 2531-2537.

[96] Mitsuhisa Ichiyanagi, Seiichi Sasaki, Yohei Sato, K. Hishida, Journal of Micromechanics and Microengineering, 19 (2009) 045021.

[97] J.D. Boyle, H. Lappin-Scott, Biofouling, 22 (2006) 117-123.

[98] Kelly Oliveira, Tereza Oliveira, Pilar Teixeira, Joana Azeredo, R. Oliveira, Brazilian Journal of Microbiology, 38 (2007) 318-323.

[99] M. Wahl, Marine Ecology Progress Series, 58 (1989) 175-189.

[100] Karen D. Xu, Philip S. Stewart, Fuhu Xia, Ching-Tsan Huang, G.A. McFeters, Applied and Environmental Microbiology, 64 (1998) 4035-4039.

[101] Maureen E. Callow, J.A. Callow, Biologist, 49 (2002) 4-10.

[102] R. Bakke, M.G. Trulear, J.A. Robinson, W.G. Characklis, Biotechnology and Bioengineering, 26 (1984) 1418-1424.

[103] Philip J. Wyatt, D.T. Phillips, Journal of Theoretical Biology, 37 (1972) 493-501.

[104] Teresa R. De Kievit, Richard Gillis, Steve Marx, Chris Brown, B.H. Iglewski, Applied and Environmental Microbiology, 67 (2001) 1865-1873.

[105] Suzanne M. J. Fleiszig, Shiwani K. Arora, Rajana Van, R. Ramphal, Infection and Immunity, 69 (2001) 4931-4937.

[106] Reuben Ramphal, Lilia Koo, Karyn S. Ishimoto, Patricia A. Totten, J. Cano Lara, S. Lory, Infection and Immunity, 59 (1991) 1307-1311.

[107] Koji Yonekura, Saori Maki-Yonekura, K. Namba, Nature, 424 (2003) 643-650.

[108] K. Triandafillu, D.J. Balazs, B.-O. Aronsson, P. Descouts, P. Tu Quoc, C. van Delden, H.J. Mathieu, H. Harms, Biomaterials, 24 (2003) 1507-1518.

[109] J.-P. Piette, E.S. Idziak, Applied and Environmental Microbiology, 57 (1991) 1635-1639.

[110] M. Elimelech, Separations Technology, 4 (1994) 186-212.

[111] J. Gregory, Particles in Water: Properties and Processes, Particles in Water: Properties and Processes, CRC Press, London, UK, 2005.

[112] W. Richard Bowen, Adam S. Fenton, Robert W. Lovitt, C.J. Wright, Biotechnology and Bioengineering, 79 (2002) 170-179.

[113] H. Morisaki, Journal of General Microbiology, 137 (1991) 2649-2655.

[114] M.E. O'Neill, Chemical Engineering Science, 23 (1968) 1293-1298.

[115] A.J. Goldman, R.G. Cox, H. Brenner, Chemical Engineering Science, 22 (1967) 653-660.

[116] D.H. Buckley, NASA Technical Note, NASA TN D-7529, 1973.

[117] Madhumita Mahalanabis, Hussam Al-Muayad, M. Dominika Kulinski, Dave Altman, C.M. Klapperich, Lab on a Chip, 9 (2009) 2811-2817.

[118] Aubrey F. Mendonca, Terry L. Amoroso, S.J. Knabel, Applied and Environmental Microbiology, 60 (1994) 4009-4014.

[119] M. W. Mittelman, D. e. Nivens, C. Low, D.C. white, Microbial Ecology, 19 (1990) 269-278.

[120] Brenda J. Little, Robert K. Pope, Tyrone L. Daulton, R.I. Ray, NACE International, Houston, TX, 2001, pp. 1-18.

[121] Iwona B. Beech, C.C. Gaylarde, Revista de Microbiologia, 30 (1999) 177-190.

[122] D.P. Clark, FEMS Microbiology Reviews, 63 (1989) 223-234.

[123] Daniel J. Hassett, John Cuppoletti, Bruce Trapnell, Sergei V. Lymar, John J. Rowe, Sang Sun Yoon, George M. Hilliard, Kislay Parvatiyar, Moneesha C. Kamani, Daniel J. Wozniak, Sung-Hei Hwang, Timothy R. McDermott, U.A. Ochsner, Advanced Drug Delivery Reviews, 54 (2002) 1425-1443.

[124] Che Y. O'May, Kevin Sanderson, Louise F. Roddam, Sylvia M. Kirov, D.W. Reid, Journal of Medical Microbiology, 58 (2009) 765-773.

[125] Ryan C. Hunter, Adam P. Hitchcock, James J. Dynes, Martin Obst, T.J. Beveridge, Environmental Science and Technology, 42 (2008) 8766-8772.

[126] M. Dubiel, C.H. Hsu, C.C. Chien, F. Mansfeld, D.K. Newman, Applied and Environmental Microbiology, 68 (2002) 1440-1445.

[127] Hui-Ping Feng, Cheng-Hsun Hsu, Jung-Kai Lu, Y.-H. Shy, Materials Science and Engineering A, 347 (2003) 123-129.

[128] I.G. Chamritski, G.R. Burns, B.J. Webster, N.J. Laycock, Corrosion, 60 (2004) 658-669.

[129] Wolfgang Sand, T. Gehrke, Research in Microbiology, 157 (2006) 49-56.

[130] Willem Norde, J. Lyklema, Colloids and Surfaces, 38 (1989) 1-13.

[131] Theodora S. Tsapikouni, Y.F. Missirlis, Materials Science and Engineering B, 152 (2008) 2-7.

[132] Marina V. Backer, Timur I. Gaynutdinov, Vimal Patel, Brian T. Jehning, Eugene Myshkin, J.M. Backer, Bioconjugate Chemistry, 15 (2004) 1021-1029.

[133] Yuncheng Liang, Nidal Hilal, Paul Langston, V. Starov, Advances in Colloid and Interface Science, 134-135 (2007) 151-166.

[134] C.J. van Oss, A. Docoslis, W. Wu, R.F. Giese, Colloids and Surfaces B: Biointerfaces, 14 (1999) 99-104.

[135] Megan Farrell, S. Beaudoin, Colloids and Surfaces B: Biointerfaces, 81 (2010) 468-475.

[136] A. Docoslis, W. Wu, R.F. Giese, C.J.v. Oss, Colloids and Surfaces B: Biointerfaces, 22 (2001) 205-217.

[137] Wenju Wu, G.H. Nancollas, Colloids and Surfaces B: Biointerfaces, 14 (1999) 57-66.

[138] Yangjun Cai, B.-m.Z. Newby, Langmuir, 24 (2008) 5202-5208.

[139] Sadhana Sharma, Ketul C. Popat, T.A. Desai, Langmuir, 18 (2002) 8728-8731.

[140] Emanuele Ostuni, Robert G. Chapman, R. Erik Holmlin, Shuichi Takayama, G.M. Whitesides, Langmuir, 17 (2001) 5605-5620.

[141] S.I Jeon, J.H Lee, J.D Andrade, P.G.D. Gennes, Journal of Colloid and Interface Science, 142 (1991) 149-158.

APPENDIX

Applicability of the XDLVO theory for interpreting adsorption of bovine serum albumin on solid surfaces

Protein adsorption is the prerequisite for bacterial attachment and cellular adhesion, which are critical for many biomedical applications. To understand protein adsorption onto substrates, predictive models are generally informative prior to experimental studies. In this study, the extended Derjaguin-Landau-Verwey-Overbeek (XDLVO) theory was employed to determine whether or not it could interpret the protein adsorption behaviors. The experimental results of fluorescein isothiocyanate labeled bovine serum albumin (FITC-BSA) adsorbed on six different surfaces: glass, octadecyltrichlorosilane modified glass, 2-[methoxypoly(ethyleneoxy)propyl]trimethoxy-silane (PEG)-modified glass, polystyrene, poly(dimethylsiloxane), and poly(methyl methacrylate) were utilized. The XDLVO interaction energy curves obtained using the surface properties of substrates and BSA molecules qualitatively predict/interpret the protein adsorption behaviors on these surfaces. Some derivation of the experimental results from the prediction was noticed for the glass and the PEG-modified glass. When including a hydration layer to the PEG-modified glass surface, the non-fouling characteristic of PEG-modified glass by proteins was also elucidated by the XDLVO theory.

A.1 Introduction

Interactions between proteins and different solid substrates are very important in many technological applications and scientific fields. Bacteria are believed to normally adhere to substrates that carry an adsorbed protein layer. The adsorption of protein will affect the bacterial attachment through both by building polymer bridging and changing the interaction energies between bacterial cells and substrates [130]. Once a substrate is introduced into a biological environment, the surface will be covered by proteins within seconds due to the protein-surface interactions, and followed by the bacterial attachment, reproduction and propagation [131]. Consequently, protein adsorption is critical in various biomedical, environmental and maritime systems. Indeed, protein adsorption has some negative impacts, such as modulating bacterial attachment and biofilm formation, which can lead to biofouling. On the other hand, protein adsorption can be beneficial in some applications. Especially in the medical applications and tissue engineering, protein adsorption plays a significant role, such as influencing drug delivery when adapters are used for targeted delivery [132].

To study the protein absorption onto substrates, predictive models of the biomolecular protein-substrate interactions are required. The classical Derjaguin–Landau–Verwey–Overbeek (DLVO) theory was originally developed to describe the forces between two charged surfaces in a liquid medium [8, 9].

Since established, the DLVO and, especially, the XDLVO theory have been found to adequately interpret/predict the adhesion/attachment behaviors in many fields, such as colloid adhesions [133, 134], and bacterial attachments [7, 19]. Compare to the micron sized colloid particles and bacterial cells, nanometer sized protein molecules are far more

complicated in structures and surface charges, which can dramatically influence the interactions during the adsorption process between the protein molecules and the substrates. For example, "soft" protein structures could be rearranged by extra driving force (non-XDLVO), leading to an enhanced adsorption, while the actual mechanism/process is still unclear [130]. Nevertheless, researchers have utilized the DLVO theory to interpret protein adsorption onto surfaces [11, 135]. In a particular case, the XDLVO theory has been employed to determine the kinetic constants of protein adsorption following the approach of von Smoluchowski's flocculation kinetics of suspended particles [134, 136, 137]. However, to the best of our knowledge, the XDLVO theory has not been employed to thermodynamically predict/interpret protein adsorption onto surfaces.

Since the XDLVO theory is based on the LW, AB, and EL interactions, in a short-range region (separation distance < 5 nm), we hypothesized that all three interactions, especially AB interaction, are critical in governing the protein adsorption process. As such, the adsorption of a protein to a substrate can be predicted according to the interaction energies estimated using the XDLVO theory. In order to verify the hypothesis, adsorption of a model protein - bovine serum albumin (BSA) on six types of surfaces: poly(ethylene glycol) (PEG) modified glass, octadecyltrichlorosilane (OTS) modified glass, polystyrene (PS), poly(dimethylsiloxane) (PDMS), and poly(methyl methacrylate) (PMMA) and glass surfaces was utilized. The results indicated that the interaction energies estimated using the XDLVO theory did roughly agree with the experimental BSA adsorption on these surfaces.

A.2 Experimental section

A.2.1 Surface preparation

Glass slides were cut into 1 × 1 cm^2 pieces and cleaned by sonication in hexane, ethanol, and deionized (DI) water for 5 min, respectively, prior to use. The cleaning of the glass slide was carried out by immersing in a freshly prepared piranha solution (70/30 v/v 98% H_2SO_4/30% H_2O_2) heated at 80 °C for 1 h and copious rinsing with DI water, then dried with compressed N_2.

The PEG-silane-modified surface (PEG surface) was prepared according to the previous method [138]. Briefly, cleaned glass slides (1×1 cm^2) were oxidized with UV/ozone oxidation for 6 min. Modification was done by immersing the samples in a solution of PEG-silane in HPLC-grade toluene (3 mM with 0.8 mL of HCl_{conc}/L) for 18 h at room temperature. Afterwards, the samples were washed once in toluene, twice in ethanol, and twice in DI water and sonicated in DI water for 2 min to remove the nongrafted PEG molecules. Then the samples were dried with compressed N_2.

The OTS-silane-modified surface (OTS surface) was also prepared according to the previous method [19]. Briefly, followed by the cleaning and oxidization procedures described above, glass slides (1×1 cm^2) modification was done by immersing in a solution of 0.168 wt% of OTS in HPLC-grade hexane for 30 min at room temperature. After removing the OTS/hexane solution, the samples were sonicated in hexane for 5 min to remove the nongrafted OTS molecules, then rinsed thoroughly with ethanol and DI water, and finally dried with compressed N_2.

PS thin film was prepared by spin coating PS toluene solution (1 wt%) onto piranha solution cleaned (described above) glass slides (1×1 cm^2), then dried at room temperature for 2 h before use.

The PDMS surface was prepared by curing a mixture of the silicone prepolymer and its curing agent (in a 10:1 mass ratio) inside a polystyrene petri dish onto an OTS-modified glass slide at 70°C for 4 h. The thickness of the surface (1 mm, similar to that of glass slide) was controlled by the amount of silicone mixture poured into the petri dish.

The PMMA surface was prepared by hot-melt (~ 120°C, between the glass transition temperature and melting temperature) pressing in between a glass slide and an OTS-modified glass slide. The thickness of the surface (1 mm, similar to that of glass slide) was controlled by the amount of PMMA utilized.

A.2.2 Surface characterization

Contact angles of DI water, methylene iodide (MI), and ethylene glycol (EG) on the surfaces were measured to determine the surface energy of the substrate. They were measured by the sessile drop technique using a Rame-Hart contact angle goniometer under ambient conditions (1 atm, 24 ± 2 °C). Both advancing and receding angles were measured on two randomly chosen spots on each of the triplicate samples. One-Touch Video Capture was used to record the drop shapes, and ImageJ was used to measure the contact angles.

A.2.3 FITC-BSA Protein adsorption and surface coverage analysis

A 100 μl of 20 μg/mL FITC-BSA in phosphate buffered saline (PBS, pH 7.4) was deposited on each sample surface and covered the entire surface. Adsorption was carried out for 20 min at room temperature. Upon removal from the BSA solution, the samples were washed thoroughly with PBS and DI water to remove non-adsorbed BSA molecules and residual salt from the buffer.

The fluorescence of FITC-BSA was imaged using a microscope fitted with appropriate filters (Axiovert 200, Carl Zeiss) and a digital camera. To determine the FITC-BSA adsorption, the mean-gray-values of adsorption images were quantified by ImageJ. The mean-gray-values were obtained from 8 images.

A.3 Results and Discussion

A.3.1 Surface properties evaluations

The surface energies and their components of all the interested surfaces were estimated using measured contact angle values. Three probe liquids, deionized (DI) water, methylene iodide (MI) and ethylene glycol (EG), were employed. The surface energy of substrates were estimated based on the contact angle of probe liquids and the approach of van Oss and co-workers [10]:

$$(1+\cos\theta)\gamma_L = 2(\sqrt{\gamma_S^{LW}\gamma_L^{LW}} + \sqrt{\gamma_S^{+}\gamma_L^{-}} + \sqrt{\gamma_S^{-}\gamma_L^{+}}) \quad (16)$$

where L denotes probe liquid and S denotes substrate surface.

Table A.1 summarizes the obtained values of water, MI and EG contact angles on glass, OTS-modified glass, PEG modified glass, PS, PDMS, and PMMA surfaces. According to the results, the freshly cleaned glass surface was the most hydrophilic (a

water contact angle of ~ 7.9°), and PEG and PMMA surfaces were also hydrophilic, while PS, PDMS and OTS-modified surface were hydrophobic with the OTS-modified glass being the most hydrophobic (a water contact angle of ~ 102.9°).

The estimated surface energies and their (LW and AB) components for the surfaces are also summarized in Table A.1. Glass showed the highest AB component, with a value of ~ 8 mJ/m^2, leading to its surface energy of 45 mJ/m^2. The PEG-modified glass and PMMA had similar surface energies, ~ 47 mJ/m^2, and their LW (44 – 45 mJ/m^2) and AB (2 – 3 mJ/m^2) components. Glass and the PEG modified glass had relatively higher γ^- than γ^+, denoting that the surfaces were negatively charged due to likely the exposed –OH group. The OTS-modified glass and PDMS had the lowest surface energy of ~ 24 mJ/m^2, primarily contributed by their LW component. Also contributed by its LW component was the surface energy of PS, which had a value of ~ 42 mJ/m^2. The small values of γ^+ and γ^- of these three surfaces indicated that the surfaces were basically non-charged.

The surface roughness of all six surfaces was measured; the average surface roughness (Ra) for all the surfaces was very similar. Therefore, surface roughness could only have minimal effects on the different of BSA adsorbed on these surfaces.

A.3.2 FITC-BSA Protein adsorption

The FITC-BSA adsorption amount was estimated using the mean-gray values from the fluorescent microscopic images (Figure A.1a – e). According to the images, the PS surface (Figure A.1d) had the most proteins adsorbed, followed by the PMMA surface (Figure A.1f). The OTS surface (Figure A.1b) and the PDMS surface (data not shown)

had similar but less proteins adsorbed than on PMMA, and glass (Figure A.a) had even less proteins adsorbed. The surface with the least proteins adsorbed, as expected, was the PEG surface (Figure A.c), whose mean-gray-value (Figure A.2) was similar to the surface (Figure A.f) prior to protein adsorption. According to the estimation based on the assumption that the PS surface was fully covered with a layer of randomly oriented BSA molecules and the size of BSA molecule (4 nm × 4 nm × 14 nm), the PS surface had a protein coverage of ~ 0.69 $\mu g/cm^2$, followed by PMMA (~ 0.50 $\mu g/cm^2$), OTS (~ 0.29 $\mu g/cm^2$), PDMS (~ 0.28 $\mu g/cm^2$), and then glass (~ 0.12 $\mu g/cm^2$), while the PEG surface had the lowest protein coverage of ~ 9 ng/cm^2. Similar results on PEG and silicon wafer (surface properties similar to that of glass) were obtained by Sharma et al. [139], who also used fluorescence intensity from fluorescence images, and confirmed by ellipsometry measurements, to determine the amounts of protein adsorbed.

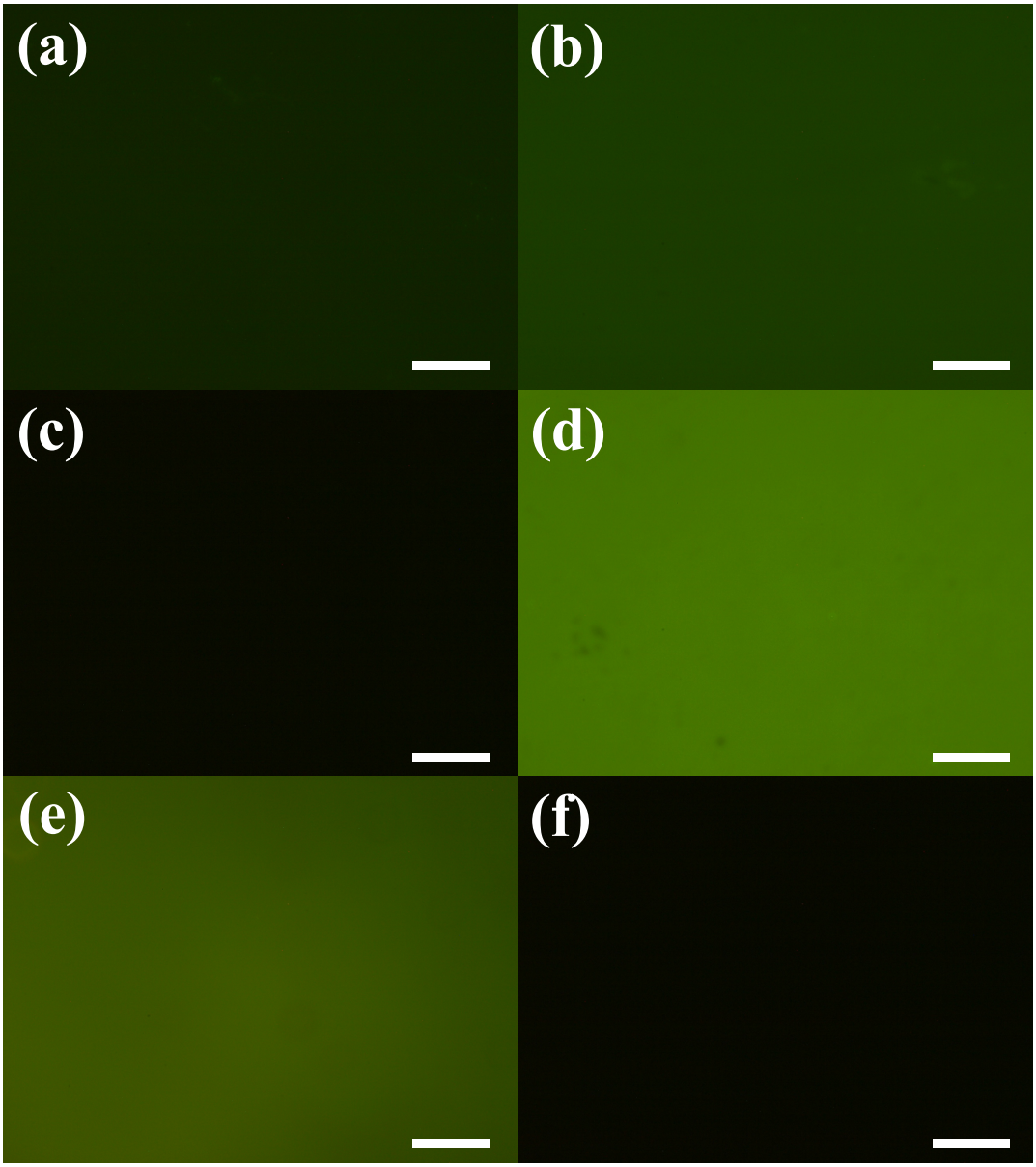

Figure A.1 Fluorescent microscope images of FITC-BSA adsorbed on (a). glass, (b). OTS, (c). PEG, (d). PS, and (e). PMMA surfaces are shown. (f) is the fluorescent image for glass prior to adsorption. The pictures were taken under exactly same conditions (e.g. light intensity and exposure time). Scale bars represent 50 μm.

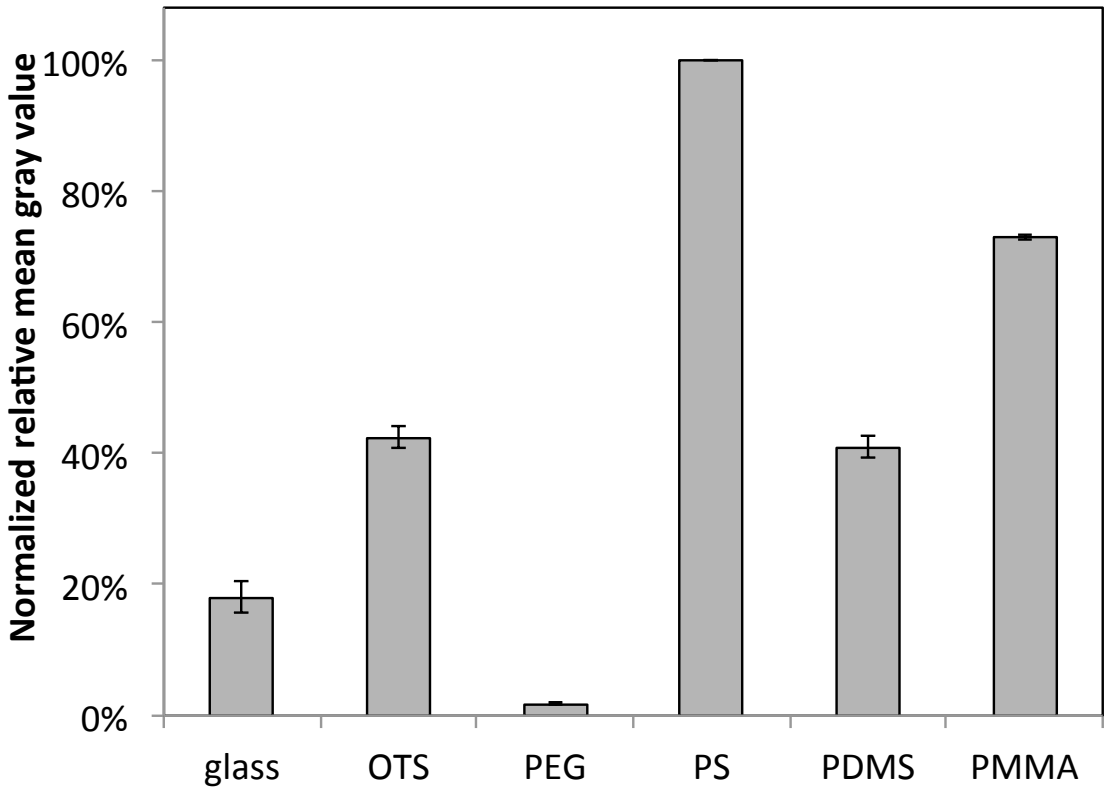

Figure A. 2 The normalized relative mean gray values of FITC-BSA on the six surfaces are shown.

Table A.1 The contact angles of the three probe liquids on the six surfaces along with surface energy and its components as well as zeta potential of BSA and the six substrate surfaces are summarized.

	glass	OTS	PEG	PS	PDMS	PMMA	BSA
θ_W (°)	7.9 ± 0.3	102.9 ± 0.8	39.8 ± 0.4	83.1 ± 0.5	98.0 ± 0.4	52.1 ± 0.5	54
θ_{MI} (°)	45.6 ± 0.8	69.3 ± 1.4	27.3 ± 1.6	35.2 ± 1.2	69.9 ± 0.7	29.5 ± 0.9	38
θ_{EG} (°)	12.9 ± 0.6	80.3 ± 1.9	21.0 ± 0.4	66.7 ± 0.6	79.3 ± 0.8	31.5 ± 0.6	5
ζ (mV)	-22	-62	-8	-25	-30	-31	-13
γ	44.7	23.5	47.9	41.9	23.1	46.4	50.3
γ^{LW}	36.7	23.3	45.3	41.9	22.9	44.4	40.6
γ^{AB}	8.02	0.19	2.59	0.22	0.12	1.92	9.65
γ^{+}	0.24	0.01	0.04	0.08	0	0.03	1.16
γ^{-}	68.27	1.10	39.92	0.15	3.05	27.9	20.03
Energy barrier* (kT)	58.6	-	10.6	-	-	-	-

A.3.3 Interpretation of the FITC-BSA adsorption by the XDLVO theory

Using surface energies and their components of BSA and substrates, the profiles of the DLVO and XDLVO interaction energies between FITC-BSA molecules and all six surfaces were generated. The energy curves for four combinations: BSA-glass and BSA-PEG are presented in Figure A.3; and BSA-OTS and BSA-PMMA are presented in Figure A.4.

For the glass surface (Figure A.3a), both DLVO and XDLVO interaction energy curves showed negative secondary energy minima, and energy barriers between the primary minima and secondary minima. For the BSA-PEG surface combination (Figure A.3b), the DLVO interaction energy curve only exhibited the primary minimum without the secondary minimum or the energy barrier; while the XDLVO interaction energy curve showed a secondary minimum and a relatively high energy barrier in addition to the primary minimum. The shapes of interaction energy curves for BSA-OTS (Figure A.4a), BSA-PS, BSA-PDMS, and BSA-PMMA (Figure A.4b) combinations were similar. For these four combinations, with the DLVO theory, energy barriers existed between primary minima and secondary minima; whereas for the XDLVO theory, the energy curves went directly down to the primary minima without the secondary minima or the energy barriers.

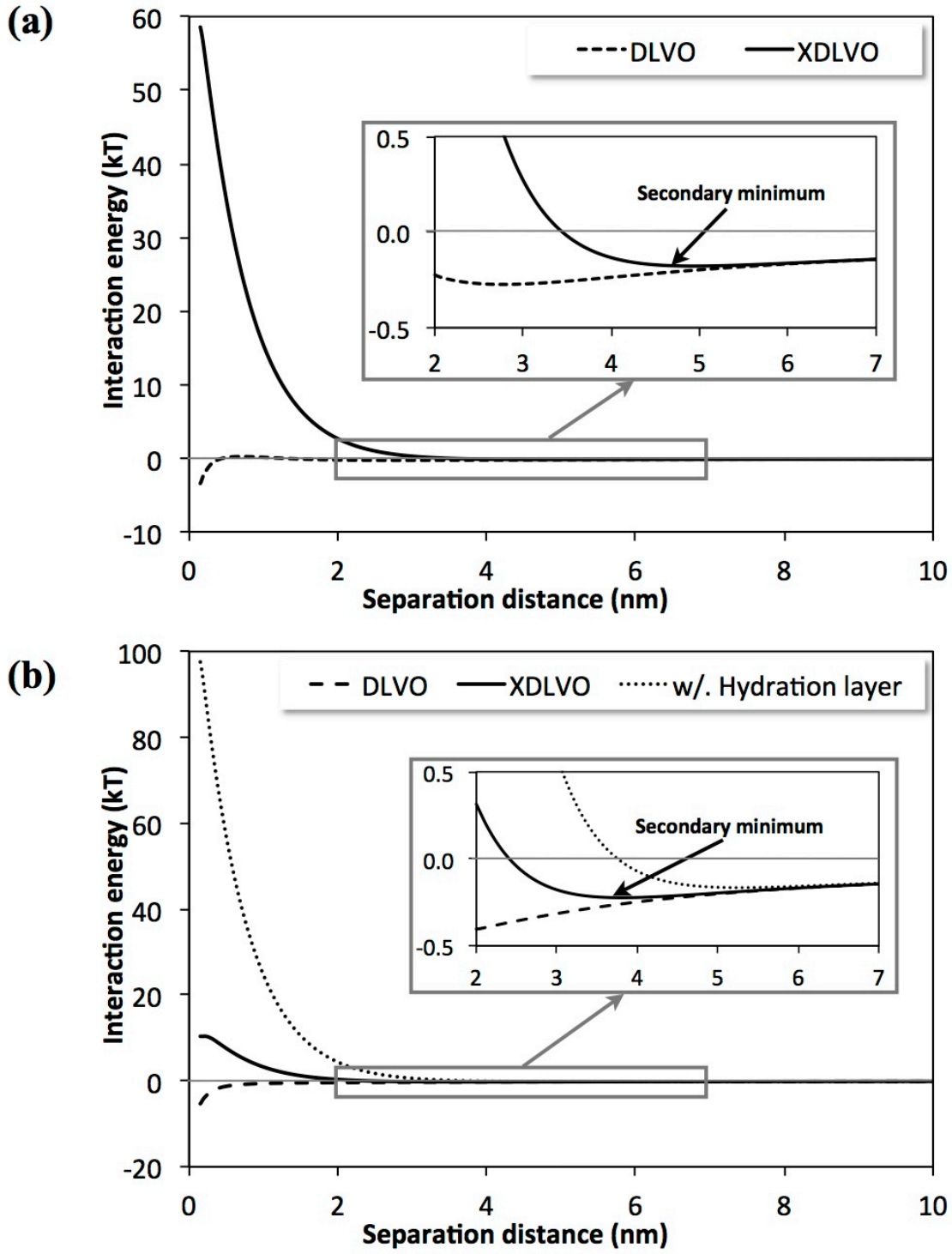

Figure A.3 The estimated DLVO and XDLVO interaction energy profiles between FITC-BSA and (a) glass and (b) PEG are presented.

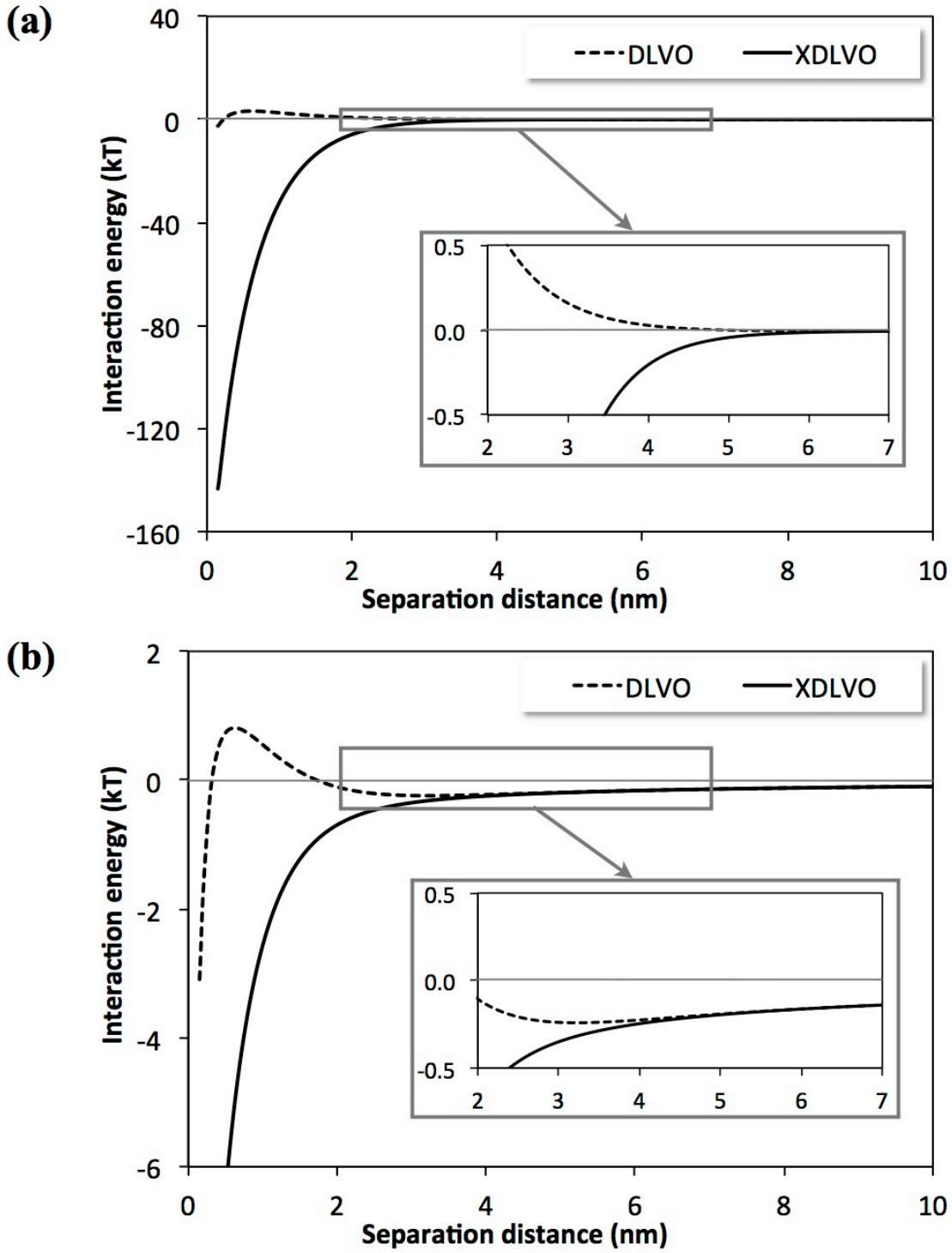

Figure A.4 The estimated DLVO and XDLVO interaction energy profiles between FITC-BSA and (a) OTS and (b) PMMA are presented.

With an energy barrier, the protein molecules may not be able to overcome the energy barrier to adsorb at the primary minimum, instead, they adsorb reversibly at the secondary minimum (i.e. weaker adsorption). Without an energy barrier, the proteins would probably be able to adsorb at the primary minimum (e.g. stronger adsorption) and likely more proteins can be adsorbed. As shown in Figure A.3 and Figure A.4, the DLVO interaction energy curves of all BSA-substrate combinations had energy barriers except the BSA-PEG combination, which only showed the primary minimum. Also, very similar DLVO energy curves were obtained for BSA-glass (Figure A.3a), BSA-PMMA (Figure A.4b), and BSA-PS (curve not shown) combinations, while the FITC-BSA adsorption behaviors were obviously different (Figure A.1). Furthermore, higher energy barriers were obtained for BSA-OTS and BSA-PDMS combinations, while the amount of FITC-BSA adsorbed on OTS and PDMS surfaces was much higher than that on the non-energy barrier PEG surface. Therefore, the energy curves obtained using the DLVO theory, which does not included the acid-base interactions, could not interpret FITC-BSA adsorption on most surfaces.

The XDLVO interaction energy curves of these combinations, on the other hand, appeared to be able to explain the observed protein adsorption. The energy profiles of the BSA-glass and BSA-PEG combinations showed energy barriers, indicated FITC-BSA molecules, if could not overcome the energy barrier, could not irreversibly adsorb on these two surfaces, leading to less adsorption. The energy curves of the BSA-OTS, BSA-PS, BSA-PDMS, and BSA-PMMA combinations all only exhibited the primary minima, suggesting that FITC-BSA molecules could adsorb irreversibly on OTS, PS, PDMS, and

PMMA surfaces, and the amount of adsorption would likely be higher than those on glass or the PEG surface.

One might wonder why the PEG and PMMA surfaces having similar surface energy and its components (Table A.1) had such different XDLVO energy curves with BSA. As shown in Table A.1, their zeta potential and γ^- were quite different. Zeta potential and γ^- influenced ΔG^{EL} and ΔG^{AB}, respectively. Using γ_2^- of ~ 40 mJ/m^2 for PEG and of ~ 28 mJ/m^2 for PMMA in Eq. (2) yielded a positive ΔG_{d0}^{AB} for PEG (15.6 kT) and a negative ΔG_{d0}^{AB} for PMMA (-12.7 kT). When the BSA molecule was very close (e.g. 1 nm) to the substrate, ΔG^{AB} was about 3-fold to one-order magnitudes greater than ΔG^{LW} and ΔG^{EL}, respectively. The differences caused by zeta potential for these two cases were not differed significantly, ΔG_{d0}^{EL} was 1.1 kT for PEG and 3.1 kT for PMMA. Consequently, the difference of γ^- of PMMA and PEG, hence the acid-base interactions, caused the dramatic difference in the interaction energy curves.

While a negative energy minimum estimated by the XDLVO analysis could suggest the tendency of protein adsorption, the correlation between the minimum energy and the actual adsorbed amount was difficult to draw. The energy barrier between the primary energy minimum and secondary energy minimum was found to be more important to elucidate whether or not and the amount of proteins could adsorb on a surface. For the three polymer surfaces and OTS-modified glass, no energy barrier from the XDLVO analysis was noticed, and proteins were easily adsorbed to these four surfaces and a greater adsorbed amount was noticed. For glass and PEG modified glass, less FITC-BSA adsorption as compared to the other four surfaces was noticed, which

appeared to correlate to the energy barrier of the XDLVO energy curve, for these two combinations (BSA-glass and BSA-PEG). One might even expect less proteins adsorbed on glass, since the energy barrier was higher for the BSA-glass combination as compared to that of the BSA-PEG combination, but the opposite experimental results were observed. One of the possible reasons was the role of hydration layer on the PEG surface, which was one of the important factors for the non-fouling characteristics of the PEG surface. This factor was not taken into account in our initial analysis based on the XDLVO theory [140]. If this hydration layer were being considered, the PEG surface would behave more like a water surface. When surface energy and surface energy components of water were used in the XDLVO analysis, the energy barrier between the primary and the secondary energy minimum was greatly increased, as shown in Figure A.3b. Another possible reason was the steric repulsion due to the elastic force caused by molecule long chain compression [141], which could make it even harder for protein molecules to adsorb on the PEG surface.

A.4 Summary

In this study, we evaluated FITC-BSA adsorption on glass, the OTS-modified glass, the PEG modified glass, PS, PDMS, and PMMA surfaces. Higher adsorption was resulted on the PS surface, PMMA, OTS, and PDMS, all showed no energy barrier between the primary and secondary minimum energy of the XDLVO interaction energy with BSA. Whereas for BSA-glass and BSA-PEG, lower BSA adsorption and existing of energy barrier in the interaction energy curve were noticed. In order to interpret the non-fouling characteristics of the PEG surface, an inclusion of the hydration layer on the PEG

surface for the XDLVO analysis was necessary. This study indicated that the XDLVO theory could be the first model to be employed for rough and qualitative interpretation of protein adsorption behaviors. The energy barrier was found to be more useful to interpret BSA adsorption. For more quantitative analysis, other factors, such as molecular conformation of proteins, hydration layer of the PEG, should be included into the analysis.